8-2021

Extending Core-Collapse Supernova Simulations: from the Onset of Explosion to Shock Breakout

Michael A. Sandoval
University of Tennessee, Knoxville, msandov1@vols.utk.edu

To the Graduate Council:

I am submitting herewith a dissertation written by Michael A. Sandoval entitled "Extending Core-Collapse Supernova Simulations: from the Onset of Explosion to Shock Breakout." I have examined the final electronic copy of this dissertation for form and content and recommend that it be accepted in partial fulfillment of the requirements for the degree of Doctor of Philosophy, with a major in Physics.

William R. Hix, Major Professor

We have read this dissertation and recommend its acceptance:

William R. Hix, Otis Messer, Andrew W. Steiner, Mike Guidry, Tim Schulze

Accepted for the Council:

Dixie L. Thompson

Vice Provost and Dean of the Graduate School

(Original signatures are on file with official student records.)

Extending Core-Collapse Supernova Simulations: from the Onset of Explosion to Shock Breakout

A Dissertation Presented for the

Doctor of Philosophy

Degree

The University of Tennessee, Knoxville

Michael A. Sandoval

August 2021

For Mom, I wish you were here for this journey.

Acknowledgments

First and foremost I would like to thank the Department of Physics and Astronomy at San José State University (SJSU) for not only setting me up for academic success when transitioning to graduate school, but also for preparing me on a research level. The close-knit community that was the SJSU Physics and Astronomy department truly was a family, including the SJSU Physics club. Also, if SJSU did not cancel their Optics class due to low enrollment, then I would not be here today, for that cancellation led me to taking my first Astronomy class. I would like to thank my first advisor, Aaron J. Romanowsky, who was the professor of that class and gave me a chance at research after I was eager to get involved after my mother passed away.

Along those same lines, I would like to thank my mentors at the University of Tennessee, as I would not be here without their guidance. I would like to thank Raph Hix and Bronson Messer for providing such a healthy and fun environment to conduct research in. I envy both of your abilities to explain such complicated concepts in a down-to-earth way.

I would like to thank the San Jose Sharks for losing the Stanley Cup finals in 2016 so that I could properly study for my qualifying exams, because I probably would not have passed if I *had* to continue watching the Sharks play. However, this "acknowledgment" of the Sharks will be voided if they do not win the Stanley Cup in my lifetime.

I would like to thank Andrew Mogan for being my *Super Smash Bros.* tournament buddy and for introducing me to *Metroid Prime*.

I would like to thank Chloe Keeling (now Chloe Sandoval) for putting up with me for six years and somehow not wanting to divorce me. I love you so much, even though you want me to socialize with people and I hate it. You are all the light my world needs, you are my supernova girl.

Most importantly, I would like to thank my Mom, Holly Jan Houser, who – unfortunately – is not here today to read this thesis. You set me on the right path in life and I certainly would not be here without your love and support. You were a single mom who cared for two kids and worked your ***censored*** off until the day you died. No matter how poor we were, somehow we always had plenty of stuff under the Christmas tree, and I'll never forget that. I can only hope to live up to your legacy of how you cared for your children. I was always embarrassed whenever you bragged about my studies as a Physics major because I felt like it was not that big of a deal. I'm sorry for being such a drama queen all the time, I know you were just proud of me. In the hospital, you wanted to make sure I was still going to graduate from SJSU, and I assured you that I was still going to graduate, but may not attend graduate school. Well, it turns out you lit a fire in me to keep going. I wish you could have met Chloe. I miss you and all of this is for you.

Abstract

A core-collapse supernova (CCSN) is the result of a massive star's core collapsing due to the inability of electron degeneracy pressure to provide sufficient support against gravity. Currently, there is a disconnect between when most three-dimensional CCSN simulations end (seconds) and when the explosion would reach the surface of the star and become visible (hours to days). We present three-dimensional simulations of CCSNe using the FLASH code that follow the progression of the explosion to the stellar surface, starting from neutrino-radiation hydrodynamic simulations of the first seconds performed with the CHIMERA code. We consider a 9.6-$M_\odot$ zero-metallicity progenitor, starting from both 2D and 3D CHIMERA models, and a 10-$M_\odot$ solar-metallicity progenitor starting from a 2D CHIMERA model, all simulated until shock breakout in 3D while tracking 160 nuclear species. The relative velocity difference between the supernova shock and the metal-rich Rayleigh-Taylor (R-T) "bullets" which launch from the inner precincts of the star determines how the ejecta evolves as it propagates through the progenitor and dictates the final morphology of the explosion. We find maximum ^{56}Ni velocities of $\sim$1950 km s^{-1} and $\sim$1750 km s^{-1} at shock breakout from 2D and 3D 9.6-$M_\odot$ CHIMERA models, respectively, due to the bullets' ability to penetrate the He/H shell. When mapping from 2D, we find that the development of higher velocity structures is suppressed when the 2D CHIMERA model and 3D FLASH model meshes are aligned. The development of faster growing spherical-bubble structures, as opposed to the slower growing toroidal structure imposed by axisymmetry, allows for interaction of the bullets with the shock and seeds further R-T instabilities at the He/H interface. We see similar effects in the 10-$M_\odot$ model, which achieves maximum ^{56}Ni velocities of $\sim$2500 km s^{-1} at shock breakout.

Table of Contents

List of Tables

List of Figures

Chapter 1

Core-collapse Supernovae

Statement of disclosure: This thesis contains an edited version of a soon-to-be published journal article [77]. I am the primary author of the article, and the version in this thesis has been edited and spread across Chapters 1, 2, 3, and 4.

The explosions of massive stars provide more to the universe than just an epic light show. Supernovae provide an origin story for many of the elements around us. Core-collapse supernovae (CCSNe) are the result of the gravitational collapse of the core of a massive star ($M \geq 8$ $M_\odot$, where $M_\odot$ is the mass of the Sun). Before reaching that point, massive stars spend the majority of their lives on the main sequence, where they burn hydrogen into helium in their cores. Once the hydrogen is exhausted, the stellar core undergoes gravitational contraction, which increases the temperature of the core. He-burning begins in the core when the temperature rises above 1.5×10^8 K, which transforms helium into carbon and oxygen through the fusion of helium nuclei. For a massive star, the outer layers of the star have enough mass to compress the carbon-oxygen core until it becomes hot enough to ignite carbon. The cycle of contraction, heating, and ignition repeats as the core fuses its fuel into heavier nuclei. Through this, we get nuclei such as neon, sulfur, and silicon, which eventually burn into iron. One of the results of this repeated cycle of contraction is that we find concentric shells of different composition and density. These shells are of prime importance to the research presented in this dissertation, for the explosion interacting with these shells affects the distribution of CCSN ejecta (discussed further in Sections 1.4 and 1.5). Starting from the iron core (the center of the star), we find shells of silicon, sulfur,

oxygen, neon, carbon, helium and hydrogen (the edge of the star). The final stage before collapse is silicon shell burning around the inert iron core of the massive star. This burning produces iron 'ash' that falls onto the iron core, which grows its mass until it undergoes gravitational collapse. [30]

From the exhaustion of silicon in the core, and resulting decline in nuclear energy production, until collapse, the core of the star is sustained by electron degeneracy pressure. This pressure results from gravity and the Pauli exclusion principle forcing electrons to occupy higher energy states as the star is squeezed into a smaller volume. The amount of pressure that can be provided by degenerate electrons is limited by relativity, with the limit being reached at a limiting core mass of $\mathrm{M}_{CH} = 5.76\ \mathrm{Y}_e^2\ \mathrm{M}_\odot$, where Y_e is the ratio of electrons to nucleons [17] (for the iron core, $\mathrm{M}_{CH} \sim 1.0 - 1.2 M_\odot$). Eventually, silicon shell burning contributing additional iron to the core causes the core to exceed this Chandrasekhar mass limit and the pressure exerted by the electrons becomes insufficient to support the star, leading the core to collapse. The collapse of the iron core results in the formation of a neutron star (or, in some cases, a black hole) which releases a significant amount of energy that can drive the explosion. A CCSN explosion is not as simple as a massive shock continuously pushing things out symmetrically. In fact, before being re-energized by neutrino heating, the shock stalls for hundreds of milliseconds, which is a significant amount of time in the early evolution of a supernova [4, 14]. Although there is only a small sample size, observations of CCSNe help determine how the explosion manufactures and disperses the heavy elements, specifically those between oxygen and iron, for CCSNe are dominant sources of such elements [106]. Once the explosion reaches what was the surface of the star, and for hundreds of years afterwards, observations of the distribution of matter provide insight as to how CCSNe may affect the dynamics of a galaxy, chemical evolution of that galaxy, and star formation in that galaxy. In this work, we present state-of-the-art core-collapse supernova simulations that explore the development and evolution of asymmetries as the supernova shock progresses through the entire star.

1.1 Importance of Simulations

The explanation of the origins of what exists around us is built on the results of accurate supernovae simulations tested against observations. As well as contributing to star formation and galactic chemical evolution, CCSNe are the richest astrophysical producers of heavy elements. These elements include oxygen through iron and a significant number of elements heavier than iron [1]. Since a complete supernova process does not have a simple checklist to determine if a star will explode, simulations help accurately determine what type of progenitor stars explode, and which stars turn into inert objects floating around the universe. Due to the high flux of neutrinos emitted from a core-collapse explosion, a great amount of knowledge about neutrino physics can be gained from CCSNe. Core-collapse supernovae are also relevant sources of gravitational waves [72]. Being able to cross-reference between gravitational wave and neutrino detections will serve as a significant accuracy check, for gravitational waves and neutrinos probe the regions of the supernova that are still obscured deep behind the observable material. Along with contributing to societal questions like "Where do we come from?" and "Are we made of stardust?", simulations can help answer scientific issues such as the mystery of convection in presupernova stars, and if gamma ray bursts have a direct connection with CCSNe [105].

It has been clear from the earliest observations of supernova remnants that large scale asymmetries develop in the decades between the explosion and the present day. Modern observations continue to reveal more detail. Direct imaging of ^{44}Ti emission in Cassiopeia A [38, 37] revealed previously hidden asymmetries in the innermost ejecta. Observations of ^{44}Ti ejection velocities in SN 1987A [7] suggest an even higher level of asymmetry in that supernova. X-ray observations of G292.0+1.8 [5] reveal gross elemental asymmetries in the ejecta of this young, oxygen-rich, Galactic supernova remnant, echoing earlier work on Cassiopeia A [47].

Observations at earlier epochs support the assertion that CCSN explosions are asymmetric from their earliest days [2, 59, 103, 65]. Not surprisingly, evidence from the closest supernova in modern times, SN 1987A, is particularly extensive [96, 55]. Observed asymmetries in iron lines have been explained by the concentration of iron-peak elements

into high-velocity "bullets" [83]. Similar bullets have been invoked to explain features of the Vela supernova remnant [3, 85]. The early development of fine structure in the H_α line in SN 1987A, less than a month after the explosion, [referred to as the *Bochum event*, 41], was explained by Utrobin et al. [92] as the result of a large ($\sim 10^{-3}$ $M_\odot$) clump of nickel ejected at high velocity ($\approx$4,700 km s^{-1}) into the far hemisphere of the supernova. Near-IR observations of He I lines arising roughly two months after the explosion of SN 1987A were similarly interpreted as indications of dense clumps of ^{56}Ni mixed into the hydrogen envelope [27]. Subsequent observations [82] from different viewing angles via light echo spectroscopy support a strongly asymmetric distribution of nickel.

Evidence for asymmetries in SN 1987A set in motion the earliest multidimensional studies of supernova shock propagation [see, e.g., 39, 66, 43]. These studies revealed that the supernova shock's encounters with the stellar compositional interfaces induced Rayleigh-Taylor (R-T) instabilities that effectively broke spherical symmetry. However, the asymmetry introduced was not sufficient to explain the observed asymmetries in SN 1987A, suggesting asymmetries are part of the central engine of the explosion, leading to the earliest multidimensional investigations of that central engine [62, 44, 13, 48].

These studies show us that the large-scale features associated with the explosion are directly tied to the asymmetries formed at early times due to the explosion mechanism itself. The biggest question relevant to our research is to understand how the instabilities in the central engine drive inhomogeneities in the ejecta.

1.2 The Central Engine

Prior to collapse, the core is composed of elements synthesized during stellar evolution, primarily iron and nickel at this point in the star's life. As previously mentioned, the core collapses due to the inability of electron degeneracy pressure to support the star. The collapse is eventually halted due to nuclear interactions, and the core then rebounds, causing the infalling layers above to "bounce" off of it. This "bounce shock" moves outward, but eventually stalls due to nuclear dissociation and loss of energy in the form of neutrinos. Although the shock stalls for a hundred milliseconds or more, the explosion is eventually

able to continue due to neutrino heating above the proto-neutron star (PNS) formed after collapse. This is due to a high neutrino flux present, which transports energy from the PNS to the stalled shock and the layers above the PNS [4, 98]. Once the shock has enough energy to overcome the gravity of the PNS and the ram pressure due to the infalling mass, the shock is able to propagate again.

1.3 Nucleosynthesis

Nucleosynthesis is the process of the creation of new atomic nuclei from pre-existing nucleons. The explosion mechanism in CCSNe determines the environments in which supernova nucleosynthesis occurs, for the strength and timing of the shock as well as the presence of neutrino energy deposition, or lack there of, shapes the ejecta. The neutrino reheating mechanism creates a significant delay between core-bounce and an explosion, which directly affects the nucleosynthesis. In the outer layers of the heating region, there is a decrease in neutronization due to neutrino interactions, which results in more proton-rich ejecta.

As the shock propagates, it heats the matter along the way, and for high enough temperatures – 6 GK or more – a region will obey nuclear statistical equilibrium (NSE) [61]. Under such conditions, matter is no longer sensitive to individual reaction rates and the composition is essentially only dependent on the temperature, density, neutron-richness of the matter, and nuclear parameters like the binding energy and the partition function of the isotopes. In most cases, one can tell that a region satisfies NSE when the triple alpha process and its reverse rate, ^{12}C photodisintegration, remain in equilibrium, because at that time all other reaction rates are typically already in equilibrium [104]. NSE falls apart when the rate that statistical equilibrium requires the α density to decrease drops below the max rate that α particles are able to be reincorporated into heavier nuclei. This depends on both the local thermodynamic conditions and the rate of expansion.

This is a problem in the inner regions of the star, for in these regions the shock heats the ejecta to temperatures where NSE is mainly dominated by α particles. Once that matter starts to cool and expand, the triple alpha process, and eventually all reaction pairs, fall out of equilibrium. The remaining α density is so high in this area that α captures continue,

resulting in an overabundance of heavy species along the α chain due to recombination of α particles. As a result, much of the iron synthesized in core-collapse supernovae bears the fingerprint of this alpha-rich freezeout [104]. However, as the material continues to expand and cool below 6 GK, not all α particles necessarily reassemble, and, as a result, the final abundances freeze out with a significant number of α particles remaining. It is the rapid transition that causes this freezeout – being heated sufficiently to achieve NSE, but then quickly cooled.

Although NSE has fallen apart, there still exists regions in the N-Z plane that obey their own quasi-equilibrium (QSE) relation, which is a local equilibrium condition, in contrast to a global equilibrium relation like NSE [6]. QSE unites the exchange of neutrons, protons, α particles, and photons, so one can also think of this as uniting the strong and electromagnetic reactions. Failure of a QSE group to reach NSE implies the exchange of free nucleons and α particles among neighboring nuclei are in equilibrium, but the free nucleon abundances have not achieved global equilibrium [45]. QSE is crucial because, while NSE fails to account for the intermediate abundances, quasi-equilibrium provides a more accurate estimate and representation of those nuclear species, as well as being a convenient approximation during silicon burning [45]. At low enough temperatures, while in QSE, the burning of silicon ends prematurely, which results in a larger concentration of intermediate mass elements than NSE would suggest [107, 45].

As the shock propagates and cools, above the inner helium-, nickel-, and iron-rich regions, it leaves behind, in spherically symmetric parametrized models, the products of incomplete silicon burning. Species such as ^{40}Ca, ^{36}Ar, ^{32}S and ^{28}Si are left behind [106, 89, 58]. A layer of ^{16}O, also containing ^{20}Ne, ^{24}Mg, ^{12}C, resides above that, as well as the helium layer and hydrogen envelope residing further above. At this point, nearly one second of supernova evolution time has passed since the PNS formed, and the shock is approaching the (C+O)/He interface.

1.4 Instabilities

The nucleosynthesis is mostly complete within the first seconds of the explosion, but the distribution of the species continues to develop as the explosion progresses. Although the supernova is extremely sensitive to a multitude of physics at the beginning, at this later point in the explosion, hydrodynamics is the key aspect in its evolution. Hydrodynamic instabilities, specifically Rayleigh-Taylor instabilities, affect the distribution of material most strongly.

The Rayleigh-Taylor (R-T) instability is an instability which occurs at an interface between two fluids of different densities, and starts to develop when the light fluid is pushing the heavy fluid [75, 88]. As the instabilities continue to grow, they resemble "fingers" or "bullets" penetrating through the interface. In CCSNe, this phenomenon occurs when the shock pushes material through different fluid densities, which are generally the compositional shells that resulted from stellar evolution. With gas pressure held constant at the interface by hydrostatic equilibrium, the mass densities at the interface vary by the ratio of the mean molecular mass. The pronounced shift in the density gradient at the location of the compositional interfaces makes them good candidates for R-T instabilities. Specifically, it has been shown that R-T instabilities originate at the Si/O, (C+O)/He, and He/H boundaries of the star, and that these instabilities can shape the ejecta [18, 39, 34, 66, 43, 69, 51, 49].

Kelvin-Helmholtz (K-H) instabilities also occur at the different interfaces in CCSNe due to the shear flow in certain regions of the star. This type of instability originates from a difference in fluid velocities, rather than fluid densities, at a specific interface of fluids. Since these instabilities are strongly driven by the vorticity of the fluid, K-H instabilities shred the inner region of the star and the R-T fingers. K-H instabilities shape the R-T "fingers" into the typical mushroom shape commonly seen in supernovae and other explosions.

1.5 Post One Second: Continuing to Shock Breakout

As the shock approaches the (C+O)/He interface, most of the material retains the general shape that it had when nucleosynthesis "finished" (in velocity space, at least). However, as

the shock hits that interface, things begin to change drastically due to the sudden change in the radial density profile. A shock decelerates when it encounters a density profile that changes with a shallower slope than r^{-3}, and it accelerates in the opposite case [81, 53]. Due to the complex history of nuclear burning in the shells surrounding the core (as discussed in Section 1), supernova progenitors aren't as simple as obeying a single power-law density, so the shock propagates inconsistently in time. This inconsistency results in Rayleigh-Taylor unstable pressure and density gradients at the composition interfaces of the star.

Once the shock hits the (C+O)/He interface, the shock decelerates and leaves behind a "reverse shock", a positive pressure gradient that slows down the material behind the shock (post-shock material). The material that slows down forms a shell that propagates inwards in mass coordinate, starting from the density interface that decelerated the shock [53]. What was previously the density interface of the progenitor gets carried with the momentum of the shock, and the R-T fingers start to slowly grow from a metal-rich shell that resides behind the shock. As the shock continues to progress through the He shell, the R-T fingers continue to grow through the shell as well, still keeping up with the shock. This begins the reshaping of the inner, metal-rich, regions of the ejecta.

The elements synthesized in the inner region during the first second of the explosion start to get injected into the R-T bullets from below as they push against the rear of the metal-rich shell from which the R-T bullets are growing. At this point, the metal-rich shell starts to fragment dramatically with the continuing growth of R-T instabilities. After the shock had encountered the first density interface, (C+O)/He, the shell began to fragment into clusters that followed the flow, but were being hindered by drag and the reverse shock. However, as the shock travels for hundreds of seconds through the He shell, the fragmentation worsens and the clusters no longer follow the general flow. This results in the clusters propagating ballistically, like bullets, through the star [53, 102].

One of the species present in these clusters is Ni, which, as previously described, plays an important role as the primary source of energy once the supernova "finishes" exploding. The dense regions of Ni have a large enough momentum that they cannot be slowed down as easily as the lighter metal clumps. Consequently, they are able to penetrate through the star more easily. These bullets, because they are propagating through the He shell,

are thickly coated in He, and as the He from the progenitor mixes with the bullets from the explosion, it fills the gaps between the bullets. As the bullets try and catch up with the shock, the shock approaches the He/H interface of the star. Once the shock hits that interface, a second reverse shock is formed. The speed of the bullets and how sharp the change in density gradient is at the He/H interface determine whether the bullets are slowed by this reverse shock or are able to evade collision before it forms (i.e., the reverse shock forms behind them). If the bullets are moving fast enough relative to the shock front, the trailing instabilities are able to catch up to the back of the main shock and start to penetrate through it. However, even though the He/H interface is an R-T unstable region, the bullets are never able to completely penetrate through the shock, as their kinetic energy is quickly dissipated trying to make their way through the pressure gradient. The reverse shock that forms at the He/H interface continues to propagate inward, decelerating the material as it progresses, and eventually shreds the inner regions of the star [53]. Ni which was traveling on the order of tens of thousands of km s^{-1} is slowed to thousands of km s^{-1}.

As the explosion continues through the last layer, the hydrogen envelope, the K-H instabilities continue to shape the R-T instabilities, especially in the chaotic inner region of the star that has been shredded by both the reverse shocks. On the order of hours – the specific time depends on the progenitor's density profile – the shock hits the outer-edge of the star and "breaks out", achieving a successful explosion. Although the shock has hit the edge of the star, the bullets, and the rest of the ejecta, will not be revealed to observations for several days, as the ejecta expands and the photosphere moves deeper into the star.

1.6 Modeling a CCSN

Accurate modeling of the explosion has a large effect on the results. For example, within the neutrino reheating mechanism, spectral discretization of neutrino energies has been shown to be much more accurate than gray transport, which only tracks the average neutrino energies [87]. This is because spectral transport provides a much better estimate of the distribution of energy and neutrino luminosities; therefore, there are more accurate neutrino-matter interactions, which depend strongly on the neutrino energies. In contrast,

gray transport can provide an inaccurate representation of the neutrino distribution due to higher neutrino energies dominating the average. In some cases, this can lead to gray transport overestimating the strength of the explosion or producing an explosion that is not expected. In addition, past multi-dimensional simulations using gray neutrino transport that did produce explosions greatly exceed the limit of neutron-rich ejecta allowed by observations of CCSNe [44, 46, 48].

The use of multi-dimensional simulations is also essential. In fact, spherically symmetric models generally do not explode under this regime, due to the inability to deposit enough neutrino energy to disperse the outer envelope of the star [9, 100, 11]. The development of instabilities is another place where spherically symmetric models hit an obstacle, for those models cannot develop the instabilities at the composition interfaces because they are unable to mix the fluid to develop them. Each succeeding instability furthers the departure of CCSNe from spherical symmetry. There must be asymmetries in the star that provide enough mixing to account for physical observations of the geometry of supernova remnants and high velocity bullets ejected from the star [59].

1.6.1 Parametrized Explosions

Much of the current understanding of successful CCSNe explosions is based on parametrized explosion models. Either using a neutrino "light bulb" of fixed luminosity or even more crudely by simply adding energy via a thermal energy "bomb" or kinetic energy "piston" as the explosion mechanism. In these bomb or piston models, the explosion's energy, its delay time and mass cut are supplied as initial conditions [106, 89, 69]; "mass cut" refers to the separation between the material that becomes part of the neutron star, and the material that ends up being ejecta. However, these methods ignore the neutrino-driven nature of the CCSN process. This leads to differences in the inner regions of the explosion where neutrino interactions, and the choice of the explosion mechanism itself, act strongest [33]. While more realistic in their inclusion of neutrinos, light bulb models fail to include the full feedback mechanism, leading to explosions that are still not self-consistent. As well as leading to different distributions in the ejecta, this also affects when, if, and how, the stalled shock

is re-energized to achieve a successful explosion. Therefore, self-consistent neutrino-driven simulations are more accurate in describing the formation of the elements.

On the other hand, as described above, neutrino-driven models have had trouble in the past being able to achieve successful explosions, particularly before multi-dimensional simulations. So there has been a gap between models that are able to explode consistently, but neglect important pieces of physics, and models which describe the physics more completely (at least in some ways) yet are unable to explode. In the past decade, there has been a general trend in the community toward the development of self-consistent neutrino-driven explosions. This includes models run with the UT/ORNL CCSN simulation code CHIMERA [10]. CHIMERA includes one of the more complete sets of relevant physics thought to be associated with CCSNe [12, 57, 56]. This includes spectral neutrino transport in a ray-by-ray approximation, which involves neutrino radiation transport being calculated along each radial direction, but neglecting lateral transport. However, if a region near or just inside the PNS is being considered, lateral transport is accounted for by advection because matter and neutrinos are strongly coupled in that area.

Accurate neutrino transport models that yield successful explosions lead to more accurate modeling of the ejecta in the explosion process. As previously mentioned in Section 1.3, there is a decrease in neutronization in the outer layers of the heating region, which results in more proton-rich ejecta. Because parametrized bomb or piston models ignore neutrino transport, this aspect of the physics does not occur. The lack of de-neutronization in those models directly results in the over-production of neutron-rich isotopes of iron and nickel. Therefore, this is another example of how bomb and piston models will result in a qualitatively different species composition. Parametrized models that include neutrino transport do exist, leading to more accurate study of the nucleosynthesis [31, 32]. In these parametrized neutrino transport models, the effects of neutrino interactions seem to remedy the effects of the over-production problem, as expected. There is also the enhancement of the production of certain elements – Zn, Cu, and Sc – which have been physically observed to be quite abundant in metal-poor stars, but for which previous models have failed to account [36, 16]. However, these neutrino-driven parametrized explosions are often one-dimensional or use gray transport to save computational cost, which results in the inaccurate evolution of the

turbulent, neutrino-heated ejecta. Although the development of self-consistent neutrino-driven explosions is being explored, only a select few groups follow the explosion all the way to shock breakout.

1.7 Relevant Studies

Kifonidis et al. [53] extended neutrino-driven multi-dimensional CCSN simulations to shock breakout in 2D, analyzing ^{56}Ni clump formation along the way. Previously, most late-time explosion simulations were initiated with parameterized spherical pistons or thermal bombs rather than a neutrino heating simulation. Although in axisymmetry, the work of Kifonidis et al. [53] represented a more faithful attempt at understanding the generation and propagation of ^{56}Ni bullets through the star, which at the time, displayed a discrepancy between observed and simulated velocities [43]. Kifonidis et al. [53] discovered that their 2D models displayed significant differences in the ejecta when compared to previous piston initiated simulations that did not accurately capture the growth of the R-T instabilities. This motivated further exploration of the crucial impact of the stellar density structure on the evolution of the bullets prior to shock breakout.

Hammer et al. [40] explored these issues using a series of 2D and 3D shock breakout models powered by neutrino heating. They found that the R-T instabilities generated were different than those discussed in simpler 3D simulations [68, 67, 108], and that the propagation of bullets in 3D behaved differently than in 2D. In agreement with Kane et al. [51], they showed that the inherent axisymmetry of 2D models leads to slower clumps compared to those in 3D, due to enhanced kinematic drag relative to the buoyant force. In this case, a 2D model has toroidal structures due to axisymmetry, whereas a 3D model has bubble structures that are more spherical. The density profile of the star determines how unsteadily the shock represented in those structures progresses, as it will accelerate for gradients steeper than r^{-3} and decelerates for shallower slopes [81]. The toroidal structures experience less growth, thus pre-existing toroidal R-T instabilities approach the remaining composition interfaces at a slower speed, making them less likely to penetrate the rear of the shock and the composition "wall" and spawn further instabilities. It has also been shown

that slower plumes can lead to more interaction with the reverse shock, which further slows the bullets [52, 40, 102].

Wongwathanarat et al. [102] improved upon the previous work of Hammer et al. [40] by running 3D shock breakout simulations with full 4π solid angle coverage of the star. Their simulations using four different progenitors allowed them to correlate the final morphologies to the different progenitor density structures. Although the metal-rich clumps were tied to the initial asymmetries of the explosion, they found that the shock and reverse shock dynamics determined by the density structure of the star were of prime importance in determining the final distribution of the ejecta. The methods described in Wongwathanarat et al. [102] were extended to generate light curves for potential progenitors of SN 1987A [93, 95, 94].

Rayleigh-Taylor mixing in the context of CCSN shock breakout was further studied in Müller et al. [63], who ran 3D breakout simulations representing ultrastripped stars. They investigated the recent ideas proposed in Duffell [25] and Paxton et al. [73] who theorized that R-T mixing could potentially be analyzed with a mixing-length treatment (MLT). It was found that a MLT does provide insight into the previously mentioned buoyancy versus drag dynamic. However, the simulations of Müller et al. [63] suggest that MLT is insufficient to fully model R-T mixing in this problem.

Finally, Stockinger et al. [84] also have performed full-sphere 3D shock breakout simulations with the aim of studying low-mass progenitors. This extensive study covered R-T mixing, morphology differences, ejecta composition, and remnant properties for all the evolutionary phases of the explosion. The full suite of 1D, 2D, and 3D model comparisons provide more evidence of the importance of the density structure of the progenitor star, as each model exhibited drastically different shock dynamics during the explosion. We use one of the same progenitors as in that study and compare our results below.

1.8 Objective

To truly meet our goal of understanding the observable impacts of the central engine and R-T mixing on CCSN ejecta, simulations of the supernova explosion must be carried beyond

the initial seconds where the central engine operates and the nucleosynthesis occurs. Until now, this is where CHIMERA models have ceased. Here, we take CHIMERA models as initial conditions to new simulations that follow the progression of the explosion through the entire star. Utilizing self-consistent CHIMERA models, rather than parameterized models, provides the most physically faithful starting point currently available. This is especially the case from a nucleosynthetic point of view. The previous shock breakout studies discussed above have only tracked, at most, 13 α-nuclei (^{4}He, ^{12}C, ^{16}O, ^{20}Ne, ^{24}Mg, ^{28}Si, ^{32}S, ^{36}Ar, ^{40}Ca, ^{44}Ti, ^{48}Cr, ^{52}Fe, ^{56}Ni) with two additional species to track beta decay (^{56}Co, ^{56}Fe) and a composite tracer abundance for the rest of the iron peak species. In contrast, CHIMERA gives us the ability to track 160 nuclear species from ^{1}H to ^{64}Ge. To adequately capture the instabilities, the simulations must be done in three dimensions – as implied by the results of Hammer et al. [40]. Such simulations are necessary if we wish to use observations to constrain important questions like what type of progenitors explode, or what are the limits of the neutrino-driven explosion mechanism [26].

We present a set of 3D simulations for a 9.6 $M_{\odot}$ and a 10 $M_{\odot}$ progenitor, both of which have already been exploded for the initial seconds in CHIMERA. As well as being nearly double both the radial and angular resolutions compared to Wongwathanarat et al. [102] and Stockinger et al. [84], we present the first shock breakout simulations that evolve a large nuclear network (160 species). For one of the progenitors, however, only an axisymmetric model was available from the output of CHIMERA. Although it has been shown (see above) that the difference in using a 2D model versus a 3D model is significant due to the nature of the explosion mechanism, we have explored what utility a finished 2D model could provide in absence of a completed 3D model. This helps to ascertain the extent to which an axisymmetric model can be used in 3D to analyze observables at shock breakout.

Consequently, we have performed simulations in the following ways, with their respective naming conventions:

1. 2D CHIMERA model run in 2D within FLASH (only briefly discussed for comparison purposes). Referred to as D9.6–2D2D, D10–2D2D.

2. 2D CHIMERA model launched with axisymmetry in 3D within FLASH. Referred to as D9.6–2D3D, D10–2D3D.

3. 2D CHIMERA model launched with axisymmetry in 3D within FLASH, but tilted 90° counter-clockwise about the y-axis. Referred to as D9.6–$2\text{D}3\text{D}_{\text{Tilted}}$, D10–$2\text{D}3\text{D}_{\text{Tilted}}$.

4. 3D CHIMERA model, where available, run in 3D within FLASH. Referred to as D9.6–3D3D.

In Chapter 2, we describe the computational setup, input physics, as well as details about the progenitors. Results of all simulations reside in Chapter 3, where the progression of the explosion is detailed for the 9.6 $M_{\odot}$ progenitor in Section 3.1.1 and the 10 $M_{\odot}$ progenitor in Section 3.2.1. Finally, we summarize our work and discuss key takeaways in Chapter 4.

Chapter 2

Methods

2.1 FLASH

Although CHIMERA offers spectral neutrino transport, General Relativity, and an adaptive radial grid, these features are not relevant to these extended simulations. What is desirable for these simulations is thermonuclear reactive flow and adaptive mesh refinement [54, 40]. Thus, our simulations will be performed using the FLASH code (Fryxell et al. [35], Dubey et al. [24]) developed by the Flash Center at the University of Chicago. The FLASH code is a parallel multiphysics simulation code capable of handling compressible flow problems found in astrophysical environments [35]. FLASH has three types of grids available: a uniform grid, a block-structured adaptive PARAMESH grid, and a block-structured adaptive Chombo grid. The adaptive grids resolve only the parts of the grid that need refinement (See Figure 2.1). FLASH has been used extensively to model Rayleigh-Taylor and associated instabilities, in both astrophysical and laboratory settings [23, 29, 21, 71]. For example, Couch et al. (2009) have utilized FLASH to perform simulations of supernovae using parametrized transport.

The hydrodynamics are evolved using the explicit, directionally split piecewise-parabolic method (PPM) to solve the compressible Euler equations. Although it is less sophisticated than some choices of hydrodynamics methods available in FLASH, the directionally split PPM algorithm implements consistent multi-fluid advection [74] that better maintains compositional gradients key to examining the distribution of isotopes in the ejecta.

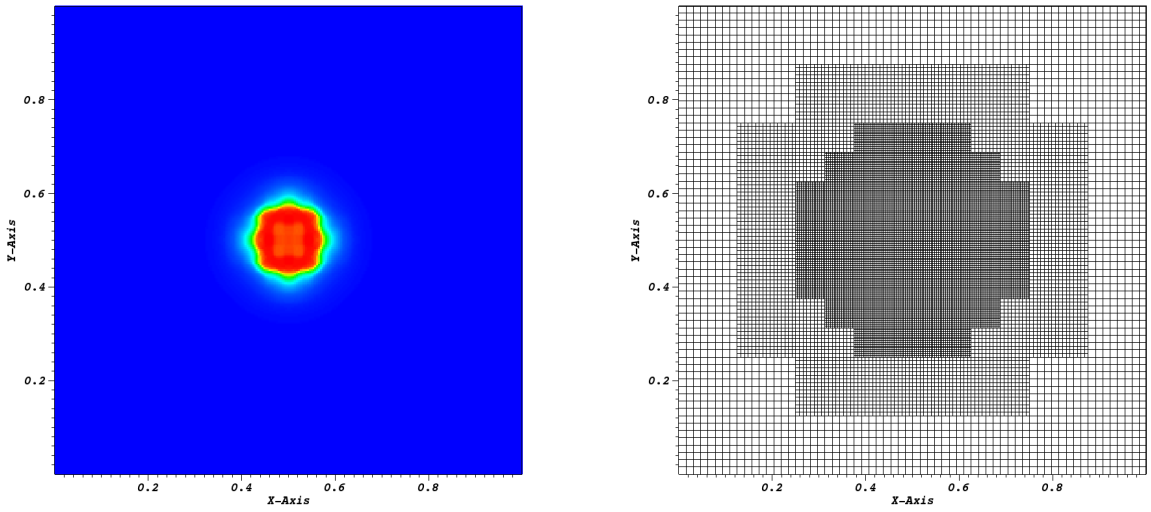

Figure 2.1: An internal energy plot of a Sedov explosion in FLASH. The adaptive-mesh refines the grid only where finer resolution is needed.

Self-gravity was included via FLASH's improved multipole solver that solves the Poisson equation through a multipole expansion [20]. Although the 3D spherical multipole solver was not originally compatible with 3D spherical geometry in FLASH, a modified version of the solver was created for this work.

2.2 Grid Setup

Both two dimensional and three dimensional simulations were run in spherical geometry. The spherical geometry is natural for self-gravitating objects and allowed us to easily "remove" the region of space containing the proto-neutron star (PNS). Following the studies of Wongwathanarat et al. [102] and Stockinger et al. [84], whose similar 3D simulations used parametrized models from the PROMETHEUS-HOTB code [80, 79], we use an inner radial boundary of 500 km to excise the PNS. Because of the high sound speed and fine zoning in that region, the excision helps alleviate the Courant-Friedrichs-Lewy (CFL) time step constraint. The CFL condition limits how far data can be passed during a given time step length, as information from a grid cell is only able to travel, at most, the distance to its immediate neighbors [22]. As a result, the smaller grid cells (higher resolution) near the inner radial boundary limit how far in time the simulation can advance due to the smaller distance between cells. A point mass was placed at the origin to replace the mass of the excised PNS.

These simulations are intended to accurately capture the explosion throughout the entire star, approximately 10^8 km in radius. An efficient way to accomplish this in spherical coordinates is to use a logarithmically-spaced radial grid, as described in Fernández [28] and shown in Wongwathanarat et al. [102]. This type of grid provides the ability to more easily maintain "square" zones with constant $\Delta\theta \approx \Delta r/r$, and can more accurately track the near power law density structure of stars. Though adaptive mesh refinement (AMR) provides an excellent way to resolve specific regions of the explosion, while efficiently ignoring others, FLASH's AMR is incompatible with log spacing. Consequently, we have implemented a log-spaced version of FLASH's uniform grid using logarithmically spaced blocks and uniformly-spaced cells within each block along the radial dimension.

As outlined in Fernández [28], we similarly define the domain between $r_{\rm min}$ and $r_{\rm max}$ such that consecutive block sizes have a ratio $\Delta r_{i+1}/\Delta r_i = \zeta > 1$, where i is the block number, which increases with increasing radius. Logarithmic block spacing is achieved by setting

$$\zeta = (r_{\rm max}/r_{\rm min})^{1/N_r} \,, \tag{2.1}$$

where N_r is the number of radial blocks. The grid is then created over $0 \leq q \leq N_r$ by defining the inner edge of each block as:

$$r_q = \zeta^q \, r_{\rm min} \,, \tag{2.2}$$

where $r_0 = r_{\rm min}$ and $r_{N_r} = r_{\rm max}$. Each logarithmically spaced block contains 16 uniformly spaced cells in the radial direction.

The inner and outer radial grid boundaries are diode and outflow, respectively, the polar grid boundaries are reflecting, and the azimuthal boundaries are periodic. The diode boundary condition is similar to outflow, but only allows matter to flow out of the domain, as opposed to letting matter freely enter the domain as well. The inner boundary is fixed until the first R-T instabilities begin to develop (∼2–3 seconds), then is shifted to larger radii, following the progress of the shock. This is accomplished by removing the innermost radial block whenever the inner boundary becomes smaller than 1% of the minimum shock radius. This removes the region where the PNS, absent from our model, may have influence in the form of a PNS wind, and makes the simulation computationally cheaper, progressively reducing the number of radial zones, which, in turn, relaxes the CFL time step constraint. The mass loss caused by moving the inner boundary is small, but not negligible – it is consistently $\sim 10^{-5}$ $M_\odot$ in all of our 3D simulations. As we will discuss in Section 3.1.3, this accounts for only ∼1.5% of the total mass lost, while the rest is due to fallback (matter passing through the inner boundary).

In addition, for all simulations, we define angle-averaged grid quantities as:

$$\langle X(r) \rangle = \frac{\int X(r) \, d\Omega}{\int d\Omega} \,, \tag{2.3}$$

where $d\Omega$ is the differential of the solid angle.

2.3 Grid Numerics

For each 3D model, the grid initially consists of $2304 \times 192 \times 384$ total cells in r, θ, ϕ, respectively. The radial section of the grid extends logarithmically from 500 km $\leq r \leq R_\star$, where $R_\star$ is the stellar radius of the progenitor (see Table 2.1). As with Hammer et al. [40], cones were excised along the poles to help further relax the CFL condition in 3D – in this case having a half-opening angle of 5°. The grid therefore covers $0.0278\pi \leq \theta \leq 0.972\pi$ at $\delta\theta = 0.885°$ and azimuthal angles $0 \leq \phi \leq 2\pi$ at $\delta\phi = 0.938°$. In two dimensions, the grid covers the same radial extent and polar angles $0 \leq \theta \leq \pi$ with 2304×204 cells, respectively.

This leads to a nearly constant radial resolution of $\Delta r/r$ of 5.7×10^{-3} and 6.1×10^{-3} for models D9.6 and D10, respectively. This can be compared to 6.9×10^{-3} of Müller et al. [63], 8.9×10^{-3} of Stockinger et al. [84], and 1×10^{-2} for Hammer et al. [40] and Wongwathanarat et al. [102]. All of our 3D runs have angular resolutions $\lesssim 1°$, compared to 1° for Hammer et al. [40], 1.6° for Müller et al. [63], and 2° for both Wongwathanarat et al. [102] and Stockinger et al. [84].

2.4 Mapping from CHIMERA to FLASH

Depending on what type of model we are initializing from, different approaches are necessary when mapping from Chimera to FLASH. A 3D Chimera model uses a specialized "Yin-Yang" overlapping grid [50], so unique interpolation methods are used when considering this type of grid (discussed in Section 2.4.1). A 2D Chimera model uses a basic spherical grid, which allows us to directly interpolate from Chimera to FLASH without having to consider where we are in the domain. However, when tilting our models (for D9.6–2D3D$_{\text{Tilted}}$ and D10–2D3D$_{\text{Tilted}}$), a coordinate transform – described in detail in Section 2.4.2 – is applied before the interpolation.

Table 2.1: Progenitor Structure

Model	(C+O)/He [km]	He/H [km]	$R_\star$ [km]	$t_{\rm map}$ [s]
D9.6	6.95×10^3	1.40×10^7	1.50×10^8	0.650 (0.467)
D10	2.02×10^4	4.32×10^6	3.57×10^8	1.763 (...)

Note. — Radii of the composition interfaces are defined as the positions at the edge of the stellar layers where the dominant mass fraction of the layer drops below half its maximum value within the layer. $R_\star$ is the stellar radius of the progenitor, and $t_{\rm map}$ indicates the post-bounce time when the CHIMERA conditions are mapped into FLASH. Mapping time of the 3D CHIMERA model, if available, is given in parentheses.

2.4.1 Yin-Yang Grid Mapping

This method is primarily used for the D9.6–3D3D model, as it is our only FLASH model initialized from a 3D CHIMERA model. The Yin-Yang grid is an overlapping grid that covers the entire surface of a sphere (4π steradians) and eases the coordinate pole's effect on the hydrodynamic flow that is typically seen when using traditional spherical polar grids [50, 101]. The Yin-Yang grid can be deconstructed into two patches ("Grid 1" and "Grid 2"), where each patch tracks a specific region of the domain. Both patches are related via a symmetric coordinate transformation (two subsequent rotations) and are identical in geometry, but have independent coordinate systems that cover different sections of an ordinary spherical polar grid. In angle, each grid covers polar angles $\pi/4 - \delta \leq \theta \leq 3\pi/4 + \delta$ and azimuthal angles $-3\pi/4 - \delta \leq \phi \leq 3\pi/4 + \delta$. The buffer zone, δ, is determined by the angular resolution of the CHIMERA grid, and is included to have a buffer region that provides overlap between each grid.

Each grid is offset by two subsequent rotations, 90° about the x-axis followed by a 180° rotation about the z-axis. Due to this, the angular coordinates transform as

$$\theta^{(2)} = \arccos\left(\sin\theta^{(1)} \sin\phi^{(1)}\right) , \tag{2.4}$$

$$\phi^{(2)} = \arctan\left(\frac{\cos\theta^{(1)}}{-\sin\theta^{(1)}\cos\phi^{(1)}}\right) , \tag{2.5}$$

where the inverse transform between grids is obtained by swapping the superscripts "(1)" and "(2)". The vectors transform as

$$\begin{bmatrix} v_r^{(2)} \\ v_\theta^{(2)} \\ v_\phi^{(2)} \end{bmatrix} = P \begin{bmatrix} v_r^{(1)} \\ v_\theta^{(1)} \\ v_\phi^{(1)} \end{bmatrix} , \tag{2.6}$$

where

$$P = \begin{bmatrix} 1 & 0 & 0 \\ 0 & -\sin\phi^{(2)}\sin\phi^{(1)} & -\cos\phi^{(1)}/\sin\theta^{(2)} \\ 0 & \cos\phi^{(1)}/\sin\theta^{(2)} & -\sin\phi^{(2)}\sin\phi^{(1)} \end{bmatrix} , \tag{2.7}$$

is the transformation matrix for the vectors [50].

Figure 2.2 and Figure 2.3 are examples of a Yin-Yang grid in spherical and Cartesian spaces, respectively, after applying the above transformations. Both patches are overlaid in the same coordinate system, thus "Grid 2" has been transformed and overlaid into the coordinate system of "Grid 1". Each grid point landing beyond the red boundary in Figures 2.2 or 2.3 is guaranteed to be located in the interior region of the opposite patch after the coordinate transformation (i.e. the grid point resides in an overlapping region). Consequently, each grid point lying within the red boundary is guaranteed to be located beyond the equivalent boundary of the opposite patch.

Because we only have one main grid in FLASH, as opposed to the two unique patches of CHIMERA, we must treat one of the CHIMERA patches as the "true" coordinate system in FLASH. In this case, the Grid 1 patch in CHIMERA will be directly adopted as the FLASH coordinate system. When interpolating from CHIMERA to FLASH, we consider where we are in the domain on a cell-by-cell basis. A grid cell in FLASH checks where it is in the domain and it then checks if that position corresponds to Grid 1 in CHIMERA, while at the same time checking to see that it is not located in a buffer or overlapping region. If this holds true (i.e. does the position of the cell reside within the red boundary of Figure 2.2), then no transformation is applied and the FLASH grid cell directly interpolates from the CHIMERA data. However, if the FLASH grid cell determines it is in Grid 2, then it applies the appropriate transformations (Equations 2.4 and 2.5) first before interpolating from the CHIMERA data. Once the interpolated data is retrieved, a symmetric coordinate transform is then applied to transform the newly interpolated velocity vectors to the original FLASH "Grid 1" coordinate system (Equation 2.6).

2.4.2 Tilt Mapping

The tilt method is used for the D9.6–2D3D$_{\text{Tilted}}$ and D10–2D3D$_{\text{Tilted}}$ models, in hopes of adding longitudinal velocities to the 100% latitudinal velocity system induced by axisymmetry. Recall that for the tilted models, we rotate the CHIMERA data 90° counter-clockwise about the y-axis. Counter-clockwise rotations of a vector about the y-axis are

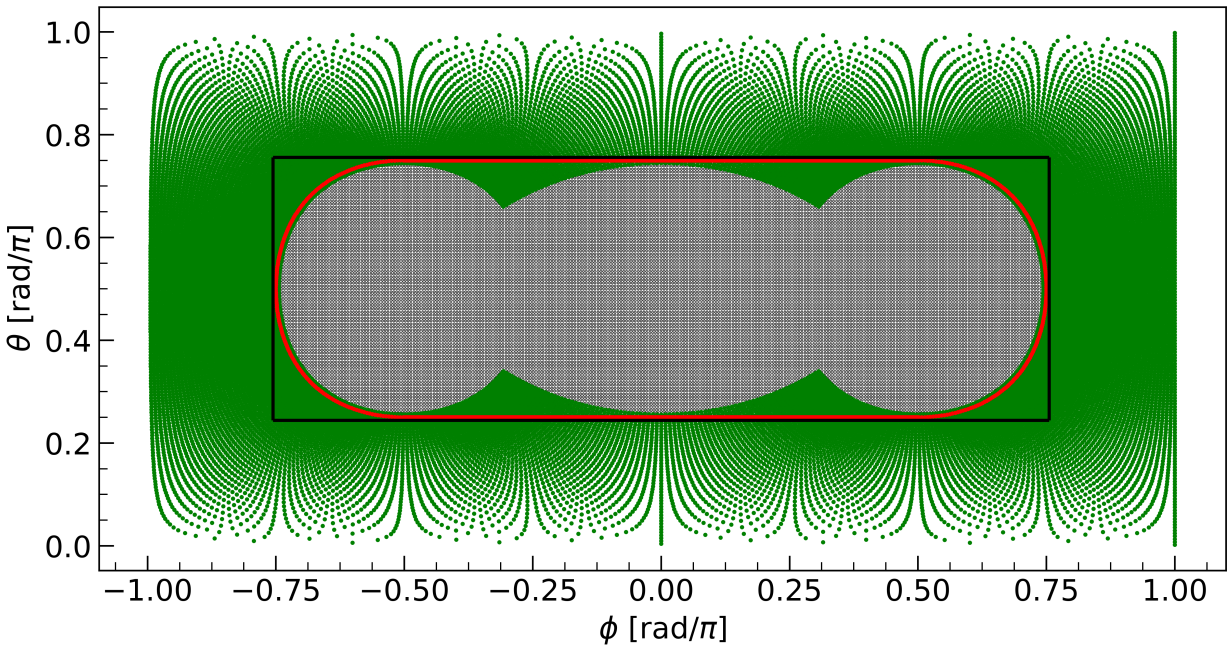

Figure 2.2: An example of a Yin-Yang grid. The black dots are the grid points of "Grid 1", and the green circles are grid points of "Grid 2" that have been transformed into the first patch's coordinate system. The red outline represents a soft boundary between the first patch's interior and overlapping regions. The solid black lines indicate the hard boundaries of Grid 1. Green grid points falling within the red boundary of Grid 1 indicate that they exist within the corners of Grid 2 (the overlapping region), where green grid points residing outside the red boundary of Grid 1 indicate that they exist on the interior of Grid 2.

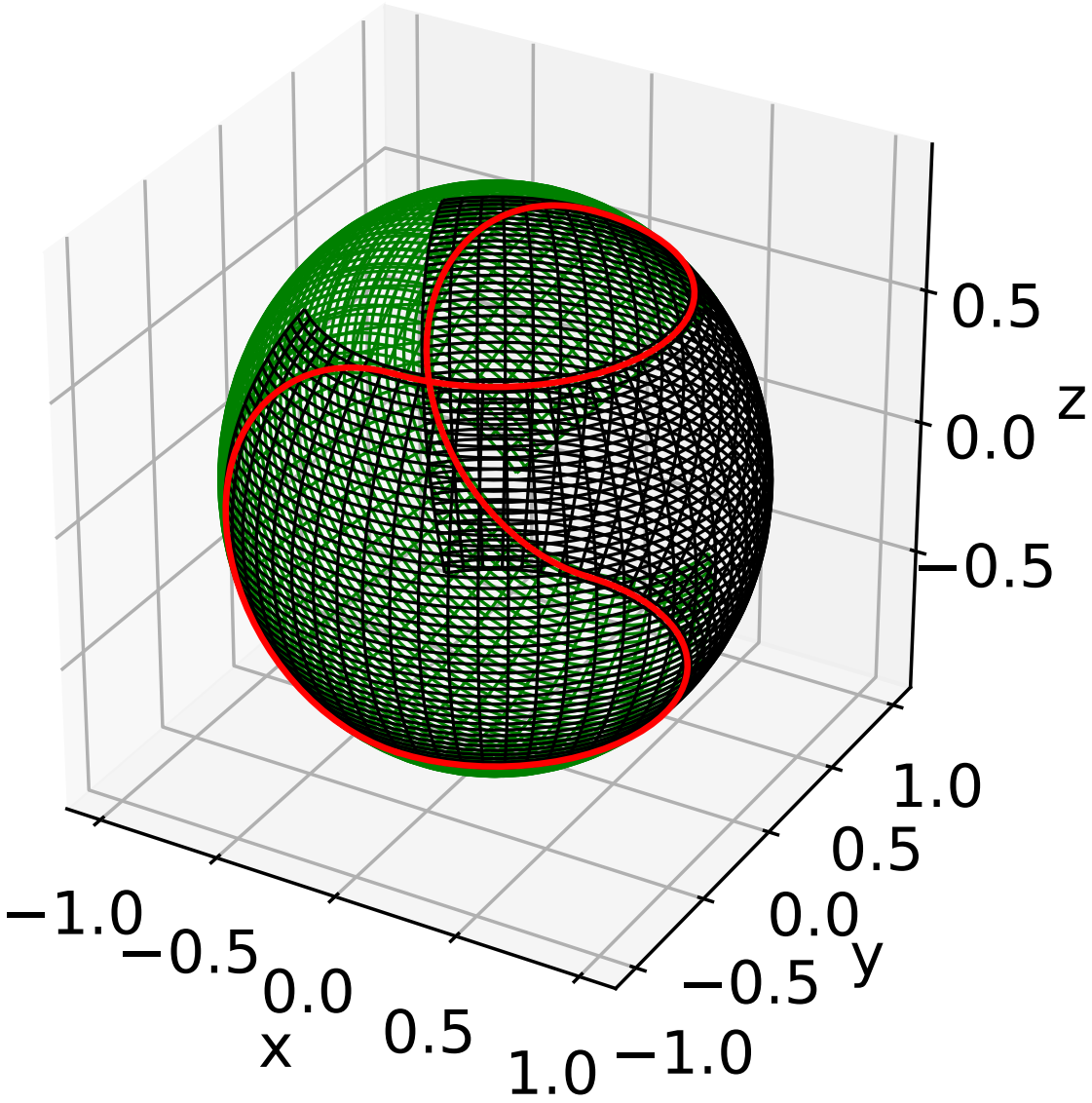

Figure 2.3: An example of a Yin-Yang grid in 3D Cartesian space. The black wireframe represents Grid 1 and the green wireframe represents Grid 2. Note the red curve marking the boundary between the overlapping regions between both patches.

represented by

$$R_y(\gamma) = \begin{bmatrix} \cos(\gamma) & 0 & \sin(\gamma) \\ 0 & 1 & 0 \\ -\sin(\gamma) & 0 & \cos(\gamma) \end{bmatrix}, \tag{2.8}$$

where γ is the angle of rotation. Consider original grid coordinates "G" and interpolated coordinates "I". We first rotate the original grid position vectors 90° clockwise to get new positions to interpolate from (going from "G" to "I"),

$$R_y(-90°) \begin{bmatrix} x_G \\ y_G \\ z_G \end{bmatrix} = \begin{bmatrix} -z_G \\ y_G \\ x_G \end{bmatrix} = \begin{bmatrix} x_I \\ y_I \\ z_I \end{bmatrix}. \tag{2.9}$$

When applying this transformation to spherical coordinates we obtain

$$r_I = r_G\,, \tag{2.10}$$

$$\theta_I = \arccos\left(\frac{z_I}{r_I}\right) = \arccos\left(\cos(\phi_G)\sin(\theta_G)\right), \tag{2.11}$$

$$\phi_I = \arctan\left(\frac{y_I}{x_I}\right) = \arctan\left(\frac{\sin(\theta_G)\sin(\phi_G)}{-\cos(\theta_G)}\right). \tag{2.12}$$

Once FLASH computes the new position vectors for a given grid cell, we need to rotate the new interpolated data back to the original FLASH positions (going back from "I" to "G"). However, we are not solely rotating position vectors this time, for now we have velocity vectors that were obtained from interpolation that we must rotate as well. Since we obtained our new vectors by rotating 90° clockwise, applying our new interpolated data back to the original coordinates is achieved by rotating the new vectors 90° counter-clockwise.

$$R_y(90°) \begin{bmatrix} x_I \\ y_I \\ z_I \end{bmatrix} = \begin{bmatrix} z_I \\ y_I \\ -x_I \end{bmatrix} = \begin{bmatrix} x_G \\ y_G \\ z_G \end{bmatrix}. \tag{2.13}$$

For spherical coordinates, our position vectors become

$$r_G = r_I \,, \tag{2.14}$$

$$\theta_G = \arccos\left(-\cos(\phi_I)\sin(\theta_I)\right) \,, \tag{2.15}$$

$$\phi_G = \arctan\left(\frac{\sin(\phi_I)\sin(\theta_I)}{\cos(\theta_I)}\right) \,. \tag{2.16}$$

Because we already have our original grid coordinates, there is no need to re-compute them, but the above relations are needed for transforming our newly acquired velocity vectors. Taking the time-derivatives of the above relations, the velocities become

$$\dot{r}_G = \dot{r}_I \,, \tag{2.17}$$

$$\dot{\theta}_G = \frac{d}{dt}(\theta_G(t)) = \frac{\dot{\theta}_I \cos(\theta_I)\cos(\phi_I) - \sin(\theta_I)\sin(\phi_I)\dot{\phi}_I}{\sqrt{1-\sin^2(\theta_I)\cos^2(\phi_I)}} \,, \tag{2.18}$$

$$\dot{\phi}_G = \frac{d}{dt}(\phi_G(t)) = \frac{\dot{\theta}_I \sin(\phi_I) + \sin(\theta_I)\cos(\theta_I)\cos(\phi_I)\dot{\phi}_I}{\sin^2(\theta_I)\sin^2(\phi_I) + \cos^2(\theta_I)} \,. \tag{2.19}$$

Because we are using cell-centered data, we do not encounter problems with divisions by zero. After applying Equations 2.17, 2.18, and 2.19 to the velocity, FLASH has successfully rotated the CHIMERA data 90° counter-clockwise. In summary, we transformed our original coordinate vectors 90° clockwise to get new data ("G" to "I"), and then passed this new data to our original coordinates by rotating back 90° counter-clockwise ("I" to "G").

2.5 Equation of State

The removal of the PNS from the grid allows us to neglect the high densities and temperatures present there and use FLASH's implementation of the Helmholtz equation of state [Helmholtz EoS; 90], which displays perfect thermodynamic consistency and includes contributions to internal energy from ions, electrons, positrons, and radiation. Because the Helmholtz EoS assumes full ionization, we halt each simulation when the shock front reaches the region of the progenitor where this criterion is no longer true ($T \lesssim 10000$ K), which happens only a few zones before shock breakout for our models.

2.6 Nuclear Network

FLASH allows us to track large numbers of species and utilize a multispecies network for nuclear burning, in this case the FLASH implementation of XNet [45]. Nuclear burning does not occur during these extended FLASH runs unless the CHIMERA runs serving as our initial conditions were stopped before nuclear burning was complete, which is the case with the D9.6–3D3D model. Regardless, the inclusion of XNet gives us the unprecedented ability to track the composition of 160 nuclear species throughout the evolution of the explosion, which leads to a more accurate analysis of the ejecta seen at shock breakout. The species list of the sn160 network from XNet is given in Table 2.2. Of particular note are ^{64}Ge and ^{66}Zn, where proton-rich and neutron-rich flows that would progress to higher atomic number in nature stagnate in this network.

2.7 Particles

Tracer particles included in our simulations are of the form of "passive particles" in FLASH. As opposed to active particles, the passive particles do not interact with the mesh, but rather track the quantities interpolated from the mesh over time. Passive particles can be thought of an explicit fluid packet being tracked through the entire simulation, both in position and in thermodynamic quantities such as temperature, pressure, and density. The use of particles will help establish a more extensive thermodynamic history of the system while also extending the nuclear network evolution through post-processing nucleosynthesis calculations [42]. Similar to the rest of our initial grid data, the particle data is also transferred from CHIMERA (see initial particle distribution in Figure 2.4). As particles in CHIMERA have already gone through the post-processing [42], extending particles in our simulations will give us the ability to compare to the analysis performed at the end of CHIMERA runs and see if what was predicted holds true. Because minimal particle post-processing work has been done for our simulations, briefly discussed in Chapter 3, we mainly investigate whether the bound and unbound particles at the end of the CHIMERA runs remain as such until the

Table 2.2: Species list in sn160 network

n	$^{1\text{–}2}$H	$^{3\text{–}4}$He	$^{6\text{–}7}$Li	^{7,9}Be	^{8,10,11}B
$^{12\text{–}14}$C	$^{13\text{–}15}$N	$^{14\text{–}18}$O	$^{17\text{–}19}$F	$^{18\text{–}22}$Ne	$^{21\text{–}23}$Na
$^{23\text{–}26}$Mg	$^{25\text{–}27}$Al	$^{28\text{–}32}$Si	$^{29\text{–}33}$P	$^{32\text{–}36}$S	$^{33\text{–}37}$Cl
$^{36\text{–}40}$Ar	$^{37\text{–}41}$K	$^{40\text{–}48}$Ca	$^{43\text{–}49}$Sc	$^{44\text{–}51}$Ti	$^{46\text{–}52}$V
$^{48\text{–}54}$Cr	$^{50\text{–}55}$Mn	$^{52\text{–}58}$Fe	$^{53\text{–}59}$Co	$^{56\text{–}64}$Ni	$^{57\text{–}65}$Cu
$^{59\text{–}66}$Zn	$^{62\text{–}64}$Ga	$^{63\text{–}64}$Ge			

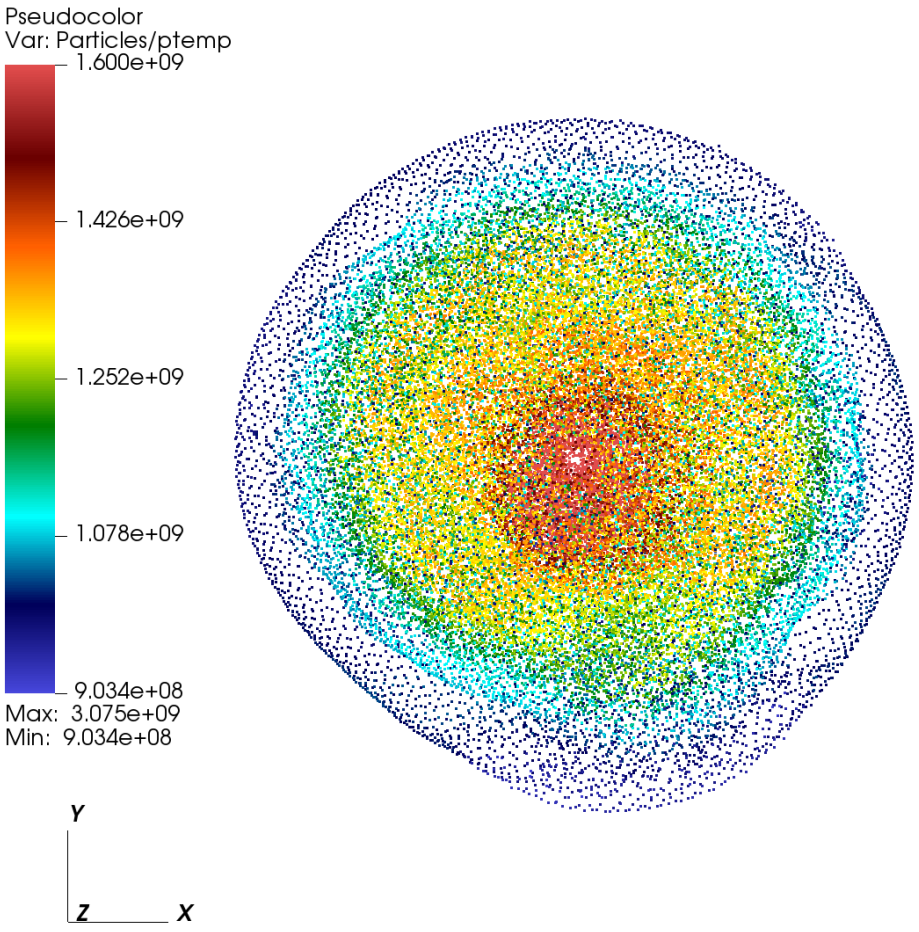

Figure 2.4: Initial distribution of particles in the D9.6–3D3D model, after having been mapped into FLASH. Particles are colored by their temperature in Kelvin.

shock reaches the surface of the star. As discussed briefly in Chapter 4, significantly more post-processing is planned for future work.

We use a linear weighting scheme in FLASH to handle the interpolation of values to and from the grid. Referred to as "Cloud-in-Cell" (CIC) mapping in FLASH (referred to as "Particle-in-Cell" mapping in other works [99]), the interpolation to and from particles is defined as a linear weighting from neighboring grid cells. Where the particle exists in a cell, and how close (or far) it is from neighboring cells establishes how much weight the surrounding cells have. A particle retrieves data from the surrounding grid cells and applies the cell weights to the newly acquired data. For each hydrodynamic time step, the particle advances based on its velocity, which is also interpolated from the grid, and repeats the interpolation process. Although the particles are able to be tracked in FLASH by default using the CIC method, 3D geometry is not natively supported. Due to this, an extended version of the existing 2D mode was created for our purposes.

2.7.1 Particle Method Verification

To establish confidence in our modified particle routine, we ran a smooth hydrodynamic test problem in FLASH with particles enabled – the isentropic vortex. This test problem has been used in the past to verify astrophysical codes and other particle schemes because of its known analytical solution [109, 15, 8, 76]. The exact solution for temperature, density, and pressure of the stationary isentropic vortex is given by

$$T = 1 - \frac{(\gamma - 1)\beta^2}{8\gamma\pi^2} e^{1-r^2}\,, \tag{2.20}$$

$$\rho = T^{\frac{1}{\gamma-1}}\,, \tag{2.21}$$

$$p = \rho^{\gamma}\,, \tag{2.22}$$

where β is the vortex strength parameter (typically $\beta = 5.0$) and γ is the ratio of specific heats (typically $\gamma = 1.4$) [109].

Many 2D tests of the isentropic vortex test problem have been performed, but we are interested in verifying our 3D particle unit. Since this problem can be extended to 3D space

[76], we tested this problem using 3D Cartesian geometry in FLASH. In FLASH, a spherical geometry version of this problem is not easily adaptable, but a Cartesian version is already pre-built. Although we use spherical coordinates for our CCSN simulations and are testing the particle routine in a different geometry, the linear weighting particle method that we are verifying does not "discriminate" between geometries, therefore the verification of this method in 3D Cartesian geometry will also apply to our 3D spherical geometry. To keep things as simple as possible, and close to default as possible, we implemented a stationary isentropic vortex and scattered 40,000 particles throughout the x-y plane. We then let the problem evolve in 3D space, although it is essentially in its axisymmetric. Similar to the work of Brown et al. [8], who tested their particles in the 2D version of the isentropic vortex in FLASH, we focused on the evolution of three specific particles – an inner, middle, and outer particle at $r = 0.276$ cm, 0.775 cm, and 3.58 cm, respectively. As the system evolves, the PPM hydrodynamics scheme introduces dispersive errors that distort the shape of the vortex, breaking its symmetry. This distortion will affect the trajectories of the particles, who - in reality - should have a constant orbital radius.

We evolved the system on a 128×128×128 equidistant grid and tracked the trajectories over a simulation time of 100 s. This time period corresponds to approximately 15-20 orbits of the inner and middle particles, whereas the outer particle does not complete a full orbit. Figure 2.5 displays the error of the radial positions of the three particles over the full simulation ($[r(t) - r(0)]/[r(0)]$). We find that the inner particle deviates from its initial orbit radius most rapidly and has the most dramatic deviation over time. However, this is only compared to the other two particles, as the percent error is still < 2 %, which is relatively small and is consistent with what was seen in Brown et al. [8]. The error steadily increasing over time is expected to be from the PPM solver slightly disturbing the system, as explained above. In contrast to the interior particles, the outer particle keeps close to its original orbital distance, which is due to the particle being less influenced than the other particles by the vortex, or its distortion, over time. Because we do not see the steadily increasing error in the outer particle, we are confident that the errors seen are mainly due to the hydrodynamic solver rather than the linear weighting method itself. In addition to tracking the positions over time, we also analyzed the error of the particle interpolation from

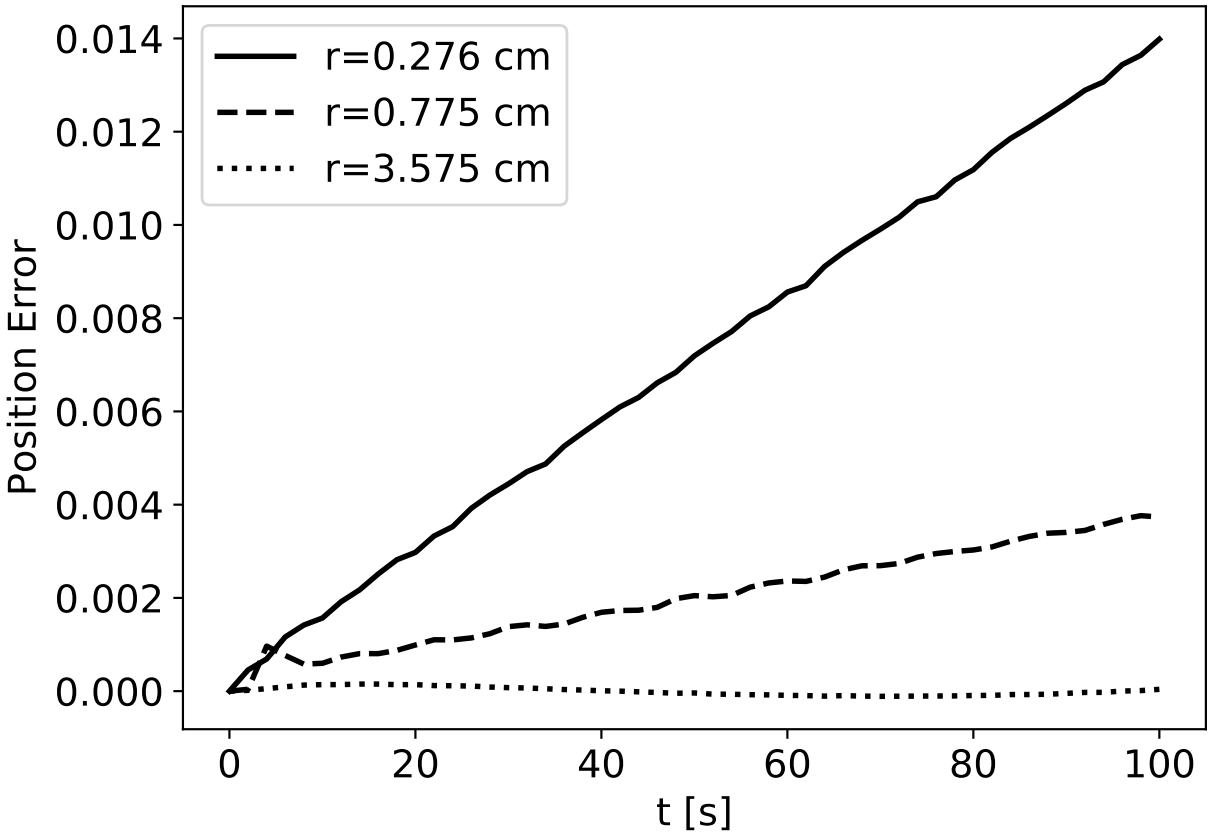

Figure 2.5: Particle trajectory errors ($[r(t) - r(0)]/[r(0)]$) for three specific particles in the isentropic vortex test problem. The solid line is the inner particle, dashed line is the middle particle, and dotted line is the outer particle.

the thermodynamic grid quantities, which are known quantities due to Equations 2.20, 2.21, and 2.22. We find ∼0.07 %, ∼0.04 %, and ∼4×10^{-6} % errors for the density of the inner, middle and outer particles, respectively. These errors are consistent with what is seen in temperature and pressure as well. Due to the relatively small errors we find, and because they are consistent with what was found in previous studies using a similar problem setup, we are confident that our implementation is accurate and that our particles are following the proper flow.

2.8 Initial Conditions and Progenitor Models

Each of our FLASH simulations are initialized from the final step of a 2D or 3D CHIMERA neutrino radiation hydrodynamics simulation of the supernova mechanism that has reached an asymptotic explosion energy. The CHIMERA simulations are initialized from two 1D progenitors calculated with the KEPLER stellar evolution code [97] up to the moment of Fe-core collapse. These simulations are part of CHIMERA's 'D-series' (and so prefixed) and are substantially similar in input physics to prior CHIMERA simulations except for the inclusion of the larger 160-species nuclear network to better handle the formation of neutron-rich ejecta. The explosion dynamics of the input CHIMERA simulations will be described in forthcoming publications. As the CHIMERA simulations do not include parts of the outer core or the envelope of the progenitor, the missing portions of the KEPLER progenitor are reattached outside the limit of each CHIMERA simulation when mapping to FLASH. The CHIMERA simulations are ended when the computational intensity required to simulate the neutrino mechanism is no longer needed.

The first progenitor is a 9.6 $M_\odot$ zero-metallicity star, provided by A. Heger (private communication). That choice is motivated by 3D simulations of this same progenitor by other groups [60, 64, 84] and is used to explore progenitors relating to low-mass cores, and to demonstrate the 160 species network. The diagnostic explosion energies at the end of the CHIMERA runs are 1.91×10^{50} ergs for CHIMERA model 'D9.6-sn160-2D' and 1.68×10^{50} ergs for CHIMERA model 'D9.6-sn160-3D', where the difference is due, in part, to the 2D run having been evolved nearly 200 ms further than the 3D model (E.J. Lentz et al., in prep.).

We refer to these models collectively as D9.6 in this work. The explosion energy in 3D is ∼95% higher than the energy reported for the same progenitor in Stockinger et al. [84] at the time of their mapping from Vertex-Prometheus to Prometheus-HOTB. Like low-mass oxygen-neon supernovae, the shock did not stall after bounce and the initial ejecta includes neutron-rich material drawn from the vicinity of the PNS that is not exposed to neutrino radiation in protracted pre-explosion convective heating. As a result, the outer ejecta of this explosion is enhanced with neutron-rich species like ^{48}Ca, ^{60}Ni, and ^{66}Zn that are not seen in typical iron-core CCSNe and less of isotopes like ^{56}Ni and ^{44}Ti that are more common in supernovae that take longer to explode. This neutron-rich ejecta is noticeable at $t_{\rm map}$ in Figure 2.6 (left), and can be seen in the ^{60}Ni peak that rivals typical CCSN ejecta like ^{56}Ni.

At the time it is mapped into FLASH, the D9.6 model has a relatively featureless density profile which gradually decreases ahead of the shock front until the edge of the star (Figure 2.7, left). The mean shock position at $t_{\rm map}$ resides in the He shell, which extends from 6.95×10^3 km to 1.40×10^7 km, and accounts for 0.33 $M_\odot$ of the total mass. An extensive H-envelope spans from the edge of the He shell to the edge of the star at 1.50×10^8 km, and accounts for 7.85 $M_\odot$ of the total mass. The compactness parameters, as described in O'Connor and Ott [70], are $\xi_{2.5} = 7.65 \times 10^{-5}$ and $\xi_{1.5} = 2.34 \times 10^{-4}$, which are smaller overall compactness than our second progenitor.

The second progenitor, a 10 $M_\odot$ solar-metallicity star, was presented in Sukhbold et al. [86] as a part of their study of 200 pre-supernova models. The 2D Chimera model ('D10-sn160-SEWBJ16', J.A. Harris et al., in prep.) has a diagnostic explosion energy of 3.075×10^{50} ergs, which is almost double the energy of the D9.6 3D at its $t_{\rm map}$and ∼50% higher than the D9.6 2D energy.

The D10 Chimera model is a traditional CCSN model with the shock stalling shortly after bounce and significant accretion onto the PNS occurring. This explains the lack of neutron-rich material when comparing composition profiles of the two models in Figure 2.6 — note the lack of a ^{60}Ni peak. Combined with a significantly higher presence of ^{12}C and ^{16}O, this leads to a different profile in the ejecta lying behind the shock. More fluctuations are also noticeable within the composition profile due to the more prolate shock front in the

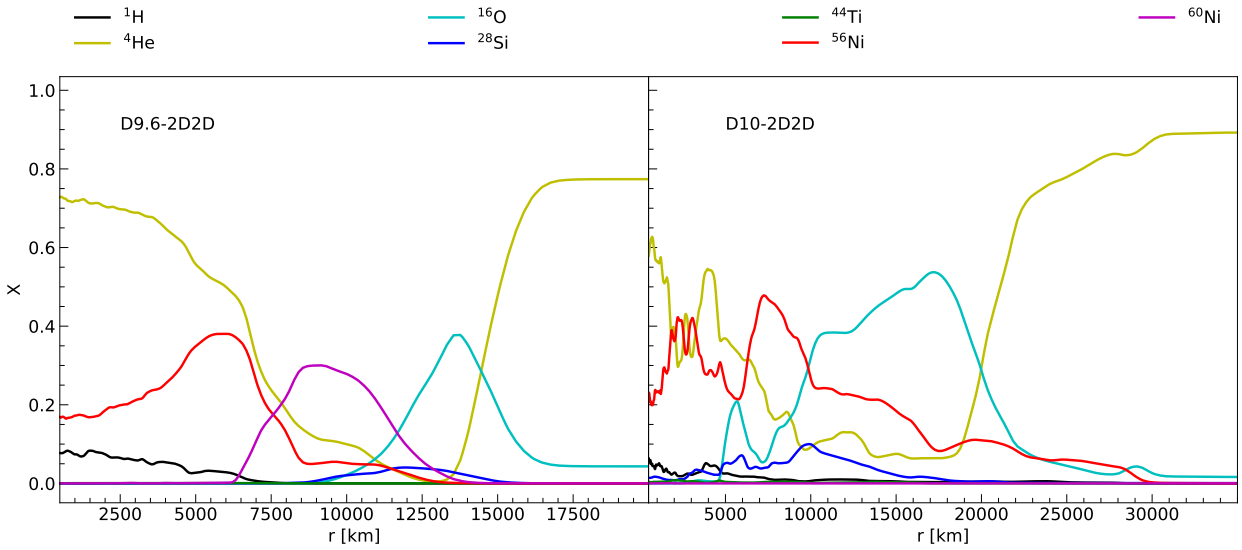

Figure 2.6: Angle-averaged mass-fractions of inner ejecta for D9.6–2D2D (left) and D10–2D2D (right) at t_{map}.

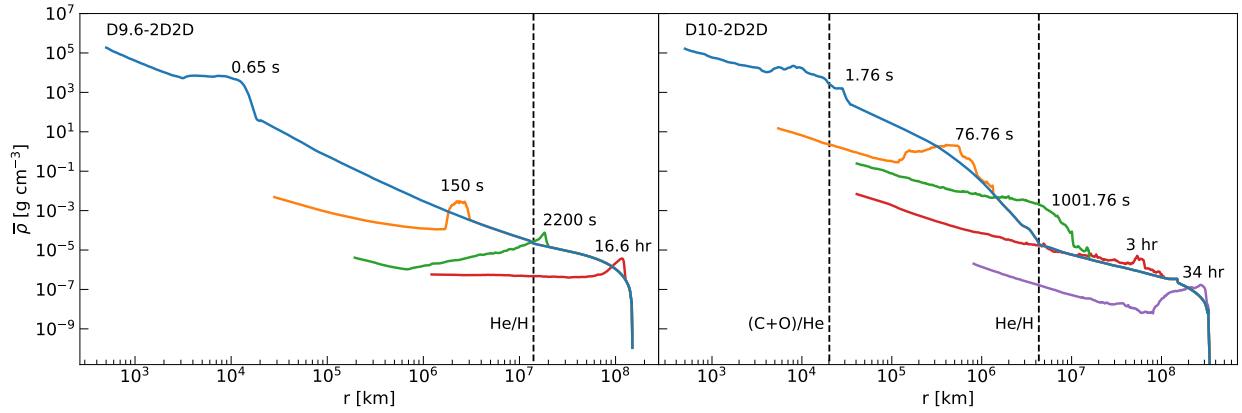

Figure 2.7: Left: Evolution of the angle-averaged density profile for the D9.6–2D2D model. The vertical dashed line indicates the position of the He/H interface. Right: Evolution of the angle-averaged density profile for the D10–2D2D model. The vertical dashed lines indicate the positions of the (C+O)/He and He/H interfaces.

D10 compared to the relatively spherical shock front of the D9.6, leading to a less uniform angular distribution of ejecta.

In further contrast to the D9.6, this progenitor has a rather erratic density profile with a dramatic change in density gradient at the He/H interface (Figure 2.7, right). This is especially noticeable in ρr^3 (see the density profiles of both models overlaid in Figure 2.8). The mean shock position at $t_{\rm map}$ resides in the former He-burning shell, which extends from 2.02×10^4 km to 3.20×10^5 km. This shell is a key feature in the ρr^3 profile, for it is the source of a dramatic acceleration that the shock experiences when transitioning to the inert He layer residing above. The He-burning shell contributes 0.44 $M_\odot$ while the remaining He layer, which ends at 4.32×10^6 km, provides a comparable 0.43 $M_\odot$ for a total mass of 0.87 $M_\odot$ of the entire He shell. The similar masses for each section of the He shell spread across widely different spatial extents explains the change in density gradient at the transition point. A hydrogen envelope spans from the edge of the He shell to the edge of the star at 3.57×10^8 km, and accounts for 7.2 $M_\odot$ of the total mass. An additional density feature can be seen near the edge of the hydrogen shell located at 1.49×10^8 km. The compactness parameters are $\xi_{2.5} = 2.04 \times 10^{-4}$ and $\xi_{1.5} = 4.32 \times 10^{-1}$. The large difference between $\xi_{2.5}$ and $\xi_{1.5}$ is the result of the (C+O)/He interface lying at 1.61 $M_\odot$. Details of key interfaces for both progenitors, as well as mapping times from CHIMERA to FLASH, are given in Table 2.1.

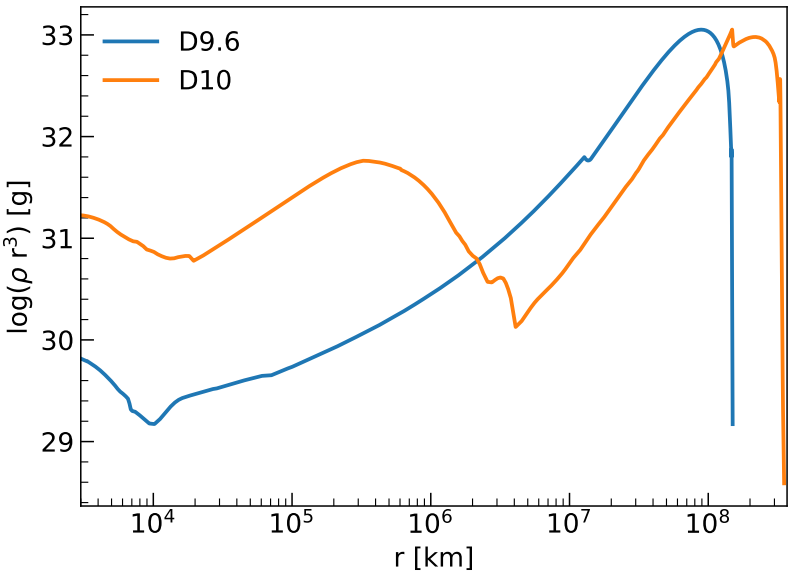

Figure 2.8: ρr^3 profiles for each progenitor plotted on the same axis.

Chapter 3

Results

3.1 D9.6 - Results

In this section, the results of the D9.6–3D3D simulation (Section 3.1.1), D9.6–2D3D simulation (Section 3.1.2), D9.6–2D3D$_{\text{Tilted}}$ simulation (Section 3.1.3), comparisons to previous studies (Section 3.1.4) and preliminary particle results (Section 3.1.5) are presented in sequence.

3.1.1 D9.6-3D3D

Here we discuss the general progression of the shock in the D9.6–3D3D model, with slight deviations to the story, specific analysis, and comparisons residing in the nested subsections. Model D9.6–3D3D was mapped into FLASH at a time $t_{\text{map}} = 466.6$ ms after the bounce that marks the formation of the PNS, having been simulated to that point with CHIMERA. At this point in the explosion, the mean shock radius is at $\sim 1.0 \times 10^4$ km, just across the (C+O)/He interface. As noted by Stockinger et al. [84], this progenitor is in the process of a 2nd dredge-up of the He shell which has created a section at the base of the shell that contains minimal hydrogen (in contrast to the rest of the He shell). The shock encountering changes to ρr^3 in this region explains the slight deviation in the trend of the shock velocity at $\sim 1.7 \times 10^4$ km and $\sim 6.0 \times 10^4$ km (see Figure 3.1).

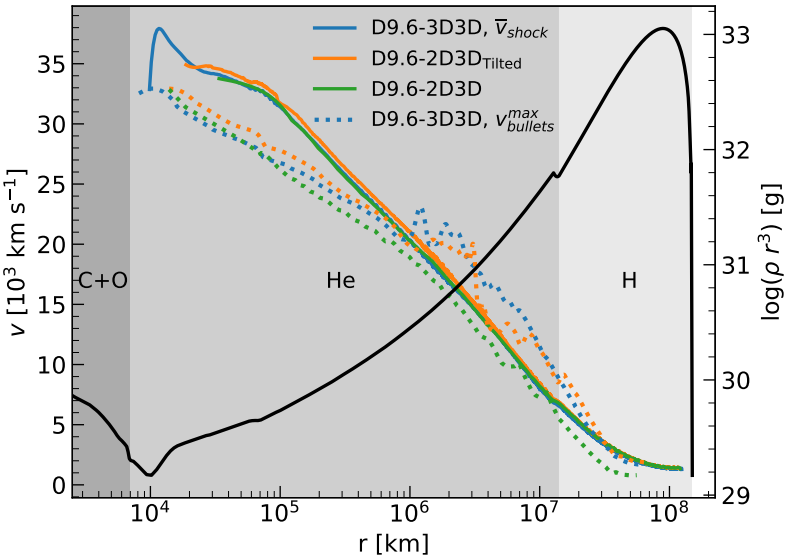

Figure 3.1: Angle-averaged shock velocity (colored, solid lines) and maximum velocity of the $X_{^{56}\mathrm{Ni+IG}} = 3\%$ bullet isosurface (colored, dashed lines) for the D9.6 models as functions of their respective angle-averaged shock or bullet radii. Density profile of the D9.6 progenitor prior to bounce (black, solid) displays the change of ρr^3 and spans the right axis. Grey shaded sections highlight the regions of the (C+O), He, H shells up to the defined R_{Int} in Table 2.1.

At the time of mapping from CHIMERA to FLASH, the metal-rich shell lying behind the shock is mainly composed of ^{12}C and ^{16}O. It is this shell, which is quasi-spherical, that begins to deform and starts to develop the initial R-T instabilities. This shell, located at the green to yellow transition in Figure 3.2(a) at $\sim 8.5 \times 10^3$ km, is also the location of the reverse shock created upon crossing the (C+O)/He interface. The departure from sphericity is imprinted on the reverse shock at its creation. Although the location of the mass shell is the position of the reverse shock in this scenario, this is not always the case as we will see with the He/H interface discussed below. Because the main shock has only just crossed the (C+O)/He interface, there are still portions of it that are still traveling down the density cliff, thus overall the shock is still accelerating at this point — represented by the velocity spike shown in Figure 3.1. There is also a wind-termination shock [also in 84] that resides close to the inner boundary and will eventually collapse inwards due to the absence of the PNS and its wind from the simulation. From this point forward, the explosion propagates through the He core, and the deformed metal-rich shell starts to mix with that material.

By $\sim$2 s, the shock has crossed fully into the He layer with the initial R-T plumes appearing as ripples in the fragmenting metal-rich shell. The instabilities begin to develop their typical mushroom state at 10 s and are still mainly composed of the species from the metal-rich shell (see ripples at $\sim 2.3 \times 10^5$ km in Figures 3.2(b), 3.3(b)). Beginning at approximately 30 s, the inner regions of the ejecta (the "hot bubble") are injected into the rear of the instabilities, including the key isotopes of nickel like ^{56}Ni and ^{60}Ni. To track the bullets, we have combined the mass fractions of ^{56}Ni and neutron-rich iron group nuclei ($X_{^{56}\mathrm{Ni+IG}}$) and have taken a 3% isosurface of the result, which enables a direct comparison to the tracking of $X_{^{56}\mathrm{Ni+Tr}}$ bullets in Stockinger et al. [84]. To approximate the crude tracer nucleus of Stockinger et al. [84], we define "neutron-rich iron group" as all species in our network falling in the range of ^{49}Cr–^{64}Ni, excluding ^{52}Fe and ^{56}Ni.

Large-scale features start to form at $\sim$60 s where the radial shock position is $\sim 1.0 \times 10^6$ km, which can be seen in Figure 3.1 as the $X_{^{56}\mathrm{Ni+IG}}$ maximum velocity (dashed blue) curve crosses the shock's (solid blue) curve. Fluctuations in the velocity after the crossing point are due to plume interactions with the shock. As the fastest moving bullet penetrates the shock, that bullet slows, and the maximum velocity shifts to the next fastest bullet.

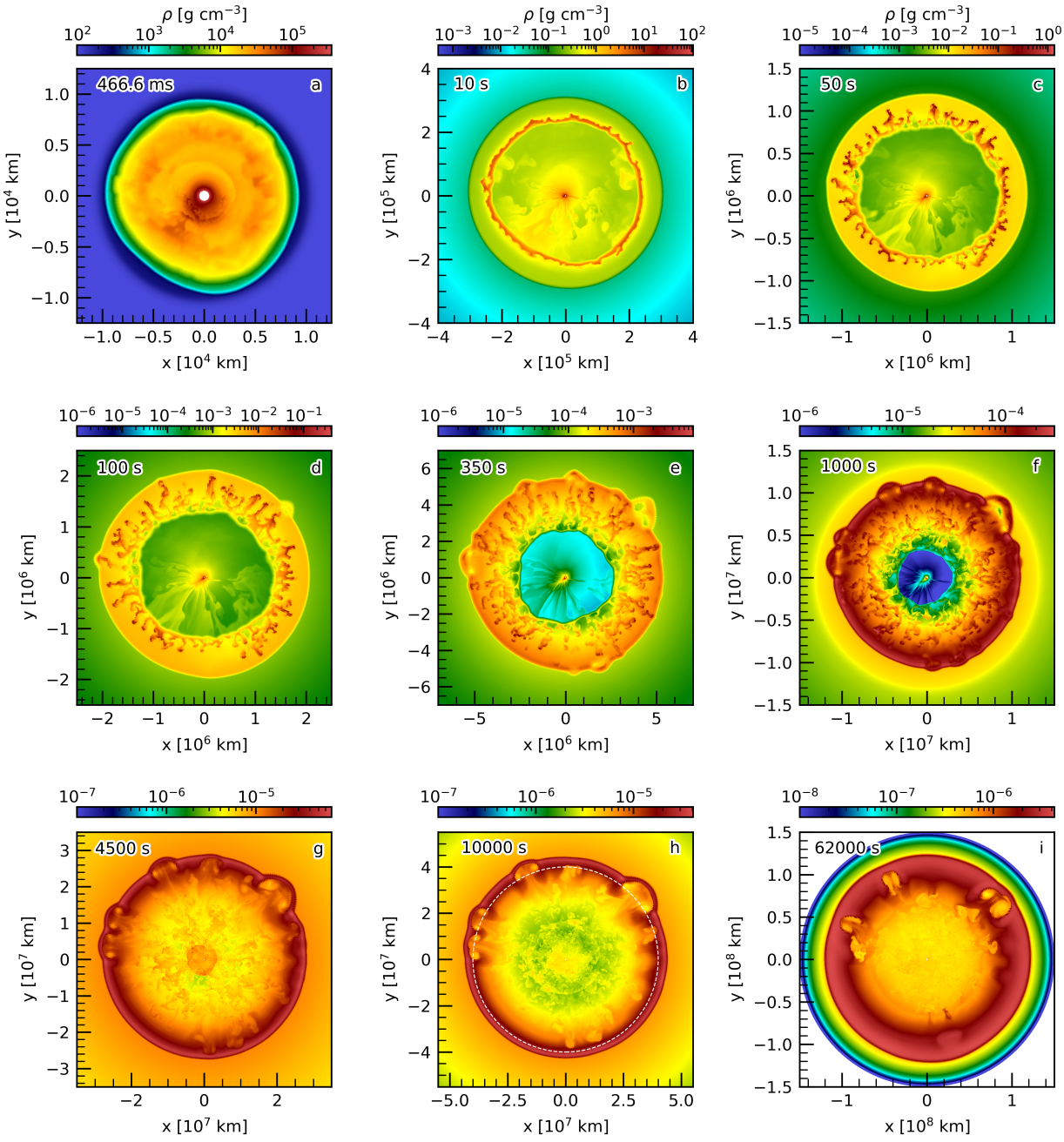

Figure 3.2: Slices of density in the D9.6–3D3D model at displayed times. Note the dramatic changes between the panels in the axis limits and the color bar range as the ejecta expands. Green to yellow color discontinuity ahead of the shock in panel (f) represents the position of the He/H interface. In panel (g), the secondary blast wave that resulted from the rebound of the first reverse shock (the collapsing blue region behind the shock in prior panels) is visible at $\sim 5.0 \times 10^6$ km. White dashed circle in panel (h) marks the 4.0×10^7 km radius used to slice the plumes in Figure 3.8.

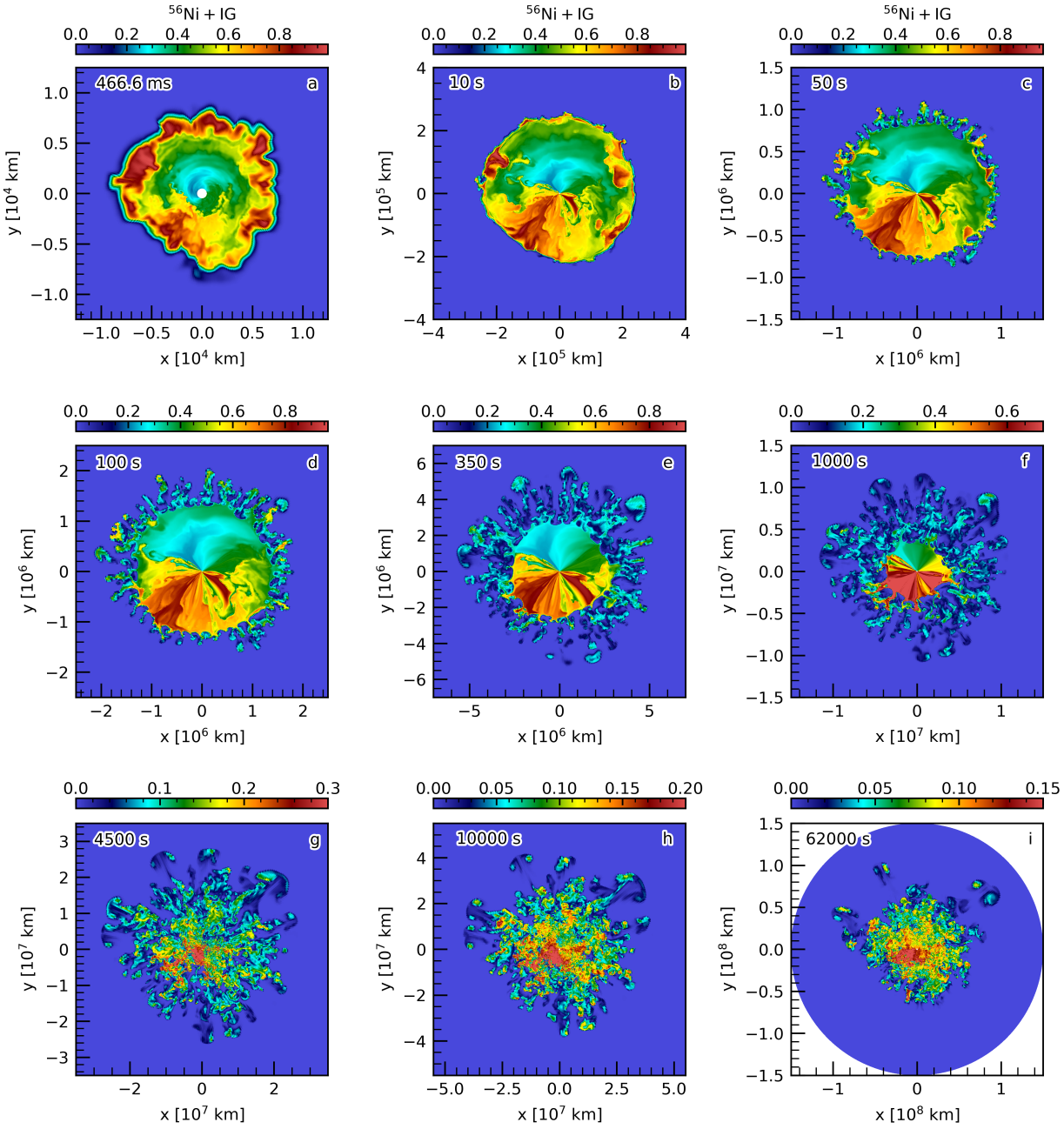

Figure 3.3: Slices of $X_{^{56}\mathrm{Ni+IG}}$ in the D9.6–3D3D model at displayed times (same times and axes as in Figure 3.2). Note change in color bars in later panels as the heavy elements become diluted.

This continues until all of the fast moving clumps eventually interact with the shock front, which then results in a steady decline of the maximum velocity of these R-T plumes. These features can explicitly be seen penetrating the shock in Figure 3.2(d).

By 150 s, there is no semblance left of the metal-rich shell, as the inner ejecta from the hot bubble has completely engulfed it. The R-T fingers have grown significantly by this point and have reached the back of the shock (see large mushroom features in middle panel of Figure 3.4). As the shock continues to progress through the He core, the R-T fingers progress with it, remaining near the rear of the shock (see elongated fingers penetrating the shock in Figures 3.2(e) and 3.3(e)). Whether the R-T fingers penetrate the shock is key to the morphology of the remnant. The shock experiences a gradual deceleration in this region of the progenitor due to the increasing ρr^3 and the extent of the He shell. Additionally, the reverse shock created at the first density interface has continued to propagate inward in mass and starts to shred the inner regions (the blue region at $\sim 2.5 \times 10^6$ km in Figure 3.2(e)). This reverse shock is not spherical as a consequence of the asphericity and timing of the main shock's interactions with the prior composition interface.

At $\sim$1000 s (Figures 3.2(f) and 3.3(f)), the shock crosses the He/H composition interface located at 1.4×10^7 km and creates a weak pressure wave due to the minimal change in ρr^3 (see Figure 3.1) that propagates inward in mass and radius before eventually steepening into a second reverse shock. This delay ensures that the second reverse shock location is quickly decoupled from position of the mass shell at the He/H interface, whereas the (C+O)/He mass shell and first reverse shock positions coincided. Although slight, the deceleration gives the closest R-T plumes to the shock front the opportunity to interact with the rear of the shock. We only see this interaction happen in D9.6–3D3D and D9.6–2D3D$_{\text{Tilted}}$, which end up having higher overall velocities compared to the other simulations (discussed in Sections 3.1.2 and 3.1.3). This interaction not only seeds new instabilities, but it further develops the most dominant R-T fingers into even larger mushroom-shaped plumes that are able to penetrate and re-shape the shock. These will be the fastest bullets at shock breakout, though the shock must still propagate through most of the envelope before they reach that point.

By 2500 s, the inner regions of the explosion are completely shredded by the first reverse shock. The mixing effects can be seen when transitioning from Figure 3.3(f) to 3.3(g) (note

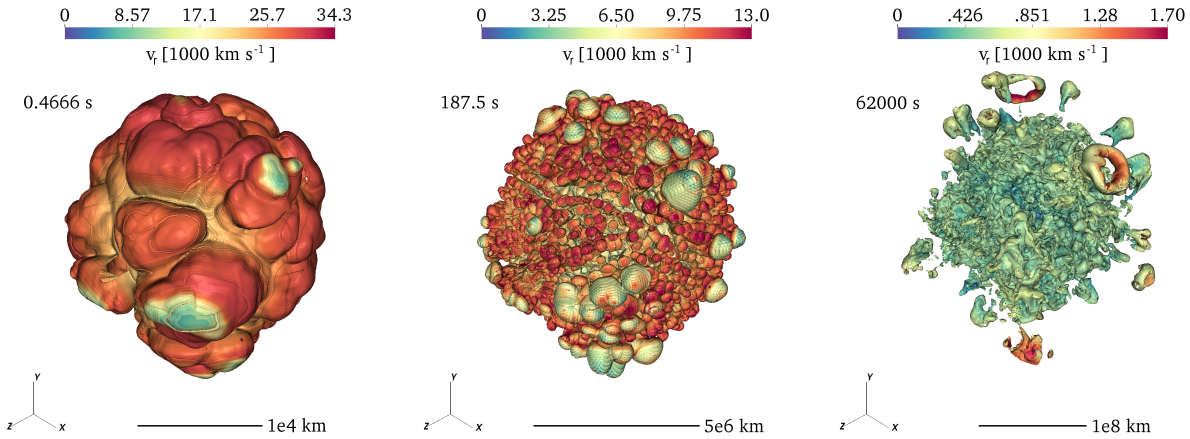

Figure 3.4: Time snapshots of the $X_{^{56}\mathrm{Ni+IG}} = 3\%$ isosurface (color-coded by radial velocity) in the D9.6–3D3D simulation. Initial asymmetries at t_{map} (left) evolve into mushroom features in the He shell (middle) that seed further R-T plumes seen at shock breakout (right).

that the distribution of ejecta is much less uniform in the inner regions after the transition). Having been born quasi-spherical and propagated through inhomogeneous regions of the star leaves the reverse shock aspherical. As a result, although some portions of the collapsing reverse shock pass through the inner radial boundary (located at $r = 1.8 \times 10^5$ km at this point in the simulation), most of the reverse shock bypasses the boundary altogether and collides with itself off center rather than at the PNS. This sets up the creation of a secondary forward-propagating blast wave which is reminiscent of the implosions discussed in supernova remnant theory [91, 19]. The blast wave can be seen at $\sim 5.0 \times 10^6$ km in Figure 3.2(g). This causes significantly more mixing, as the inner regions also bounce off the reflecting boundaries of the grid, and the R-T plumes grow to be quite abundant.

What once were primarily metal-rich mushrooms are now heavily coated in helium, for the propagation through the He core has filled the gaps between the R-T fingers and has shaped them further. However, as noted earlier, the original inner regions of the ejecta still form the "bulk" of the inner anatomy of a single finger (see Figure 3.5) due to the injection through the metal-rich shell. Most notably represented in the main anatomy of an instability are the Ni isotopes, as expected, with the most abundant isotope occupying the bullets being ^{60}Ni, from the early, neutron-rich portion of the hot bubble.

As the shock continues to expand, the pressure wave created at the He/H interface reaches the center of the grid at $\sim$20000 s, after steepening into a reverse shock at $\sim$16000 s. As the first reverse shock collided with itself, so does the second, but it does not rebound as hard as the former, because this second reverse shock has been weak since its launch as a result of the slight deceleration of the main shock noted above. Nevertheless, reaching the center still creates another forward-propagating blast wave which further influences the inner ejecta.

The shock continues to propagate through the H envelope until hitting the edge of the star, and grid (1.5×10^8 km), at $\sim$70000 s (19.4 hours). We "rewind" and declare the end of our simulations at $\sim$62000s, as this is the time where the shock enters the region of the progenitor where the Helmholtz EoS' assumption of fully-ionized hydrogen is no longer valid ($T \lesssim 10000$ K). As the shock has only been backtracked to $\sim 1.4 \times 10^8$ km from 1.5×10^8 km, the changes to ejecta morphology, yields, and speeds are negligible. Carrying

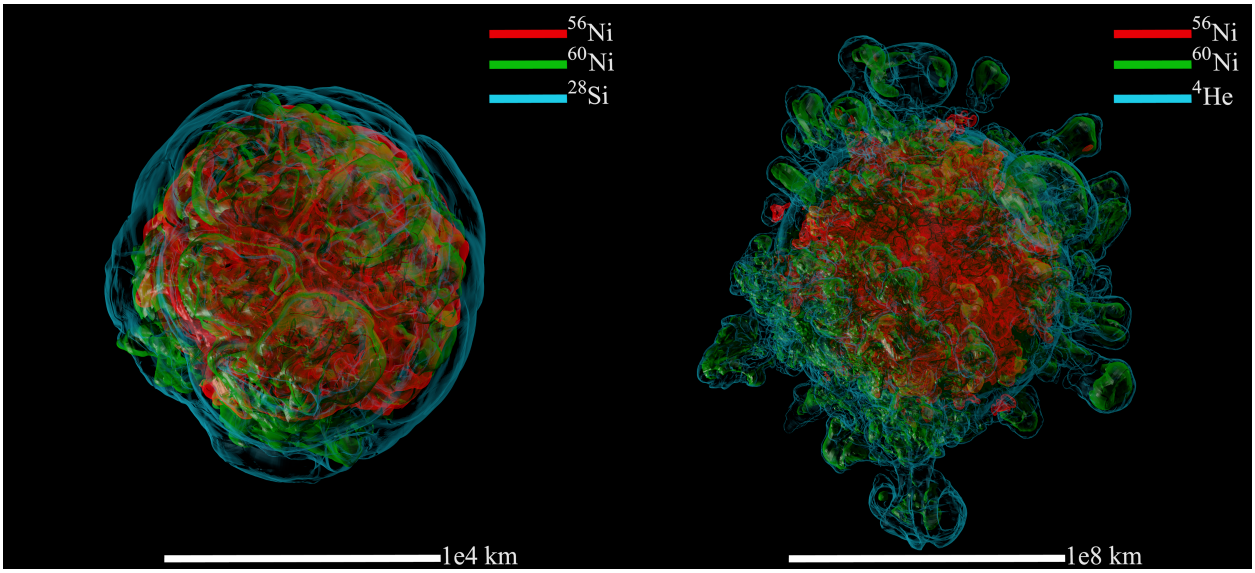

Figure 3.5: Left: Isosurfaces at 5% mass fraction of ^{56}Ni (red) and ^{60}Ni (green) reveal the early morphology of inner ejecta surrounded by a shell of ^{28}Si (cyan) displayed as a 1% mass fraction isosurface for the D9.6–3D3D model at $t_{\rm map}$ (466.6 ms). Right: Isosurfaces at 1% mass fraction of ^{56}Ni (red) and ^{60}Ni (green) highlight the inner anatomy of the ^{4}He (cyan) coated bullets displayed as a 40% mass fraction isosurface for the D9.6–3D3D model at shock breakout ($\sim$62000 s).

the models further would require accounting for the circumstellar environment and radiation hydrodynamics of shock breakout.

The synchronous conversion between kinetic and internal energy through the entire evolution of the explosion can be seen in Figure 3.6. Both quantities respond to changes in $v_{\rm Shock}$ as the shock front moves through the density structure of the star. At the end of our simulations, the internal energy is still in the process of converting to kinetic energy, which starts to converge toward the total energy of the system.

Though the D9.6–3D3D model clearly has significant extended plume features present at shock breakout (see Figures 3.4 and 3.5), the majority of trailing R-T bullets have only made it to approximately 1.0×10^8 km and are therefore well short of the surface of the star. The early development of features within the He shell, in combination with a smaller relative velocity gap between the shock and fastest moving Ni bullets, enables the further spawning of large R-T mushrooms at the He/H interface. This model demonstrates how the early-time asymmetries can impact the late-time evolution of a CCSN. Asymmetries at the time of $t_{\rm map}$ seed the initial instabilities from the (C+O)/He interface that spawn further R-T plumes upon reaching the He/H interface — provided they are moving fast enough relative to the shock. This, in turn, affects the efficiency of radial mixing in the outer envelope. As seen in the upper panels of Figure 3.7, the instabilities spawned at the He/H interface in this model drive the mixing of metal-rich ejecta beyond the inner 4 $M_\odot$ to the edge of the star. The bulk of the bullets end up with a peak centered around 500 km s^{-1} with the yields for ^{16}O, ^{28}Si, ^{56}Ni, and ^{60}Ni in that region all in the range between 1×10^{-3} and 1×10^{-4} $M_\odot$. However, the extent of radial mixing is quite apparent with a high-velocity tail reaching to $\sim$1750 km s^{-1} including yields between 1×10^{-5} and 1×10^{-7} $M_\odot$ for these same species.

These bullets are heavily coated in ^{4}He, with the maximum bins of Figure 3.7 exceeding 1×10^{-1} $M_\odot$ around 1000 km s^{-1} and roughly 1×10^{-3} $M_\odot$ around 1500 km s^{-1}. The most unusual aspect is the internal anatomy of these metal-rich clumps. The typical isotope associated with these types of bullets in the literature has consistently been ^{56}Ni, however ^{60}Ni seems to fill that role in this star. Across mass and velocity spaces, ^{60}Ni is the most abundant of our isotopes in the iron group, and it occupies more of the large-scale features whereas the ^{56}Ni resides more in the microstructure (Figure 3.5, right). Although surprising,

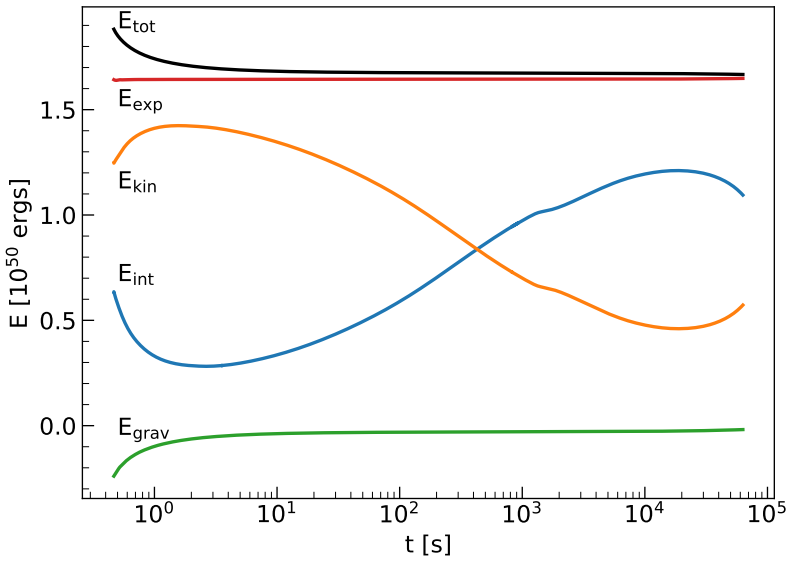

Figure 3.6: Evolution of total energy ($E_{kin} + E_{int}$) (black), explosion energy ($E_{kin} + E_{int} + E_{grav}$) (red), kinetic energy (orange), internal energy (blue), and gravitational binding energy (green) in the D9.6–3D3D model.

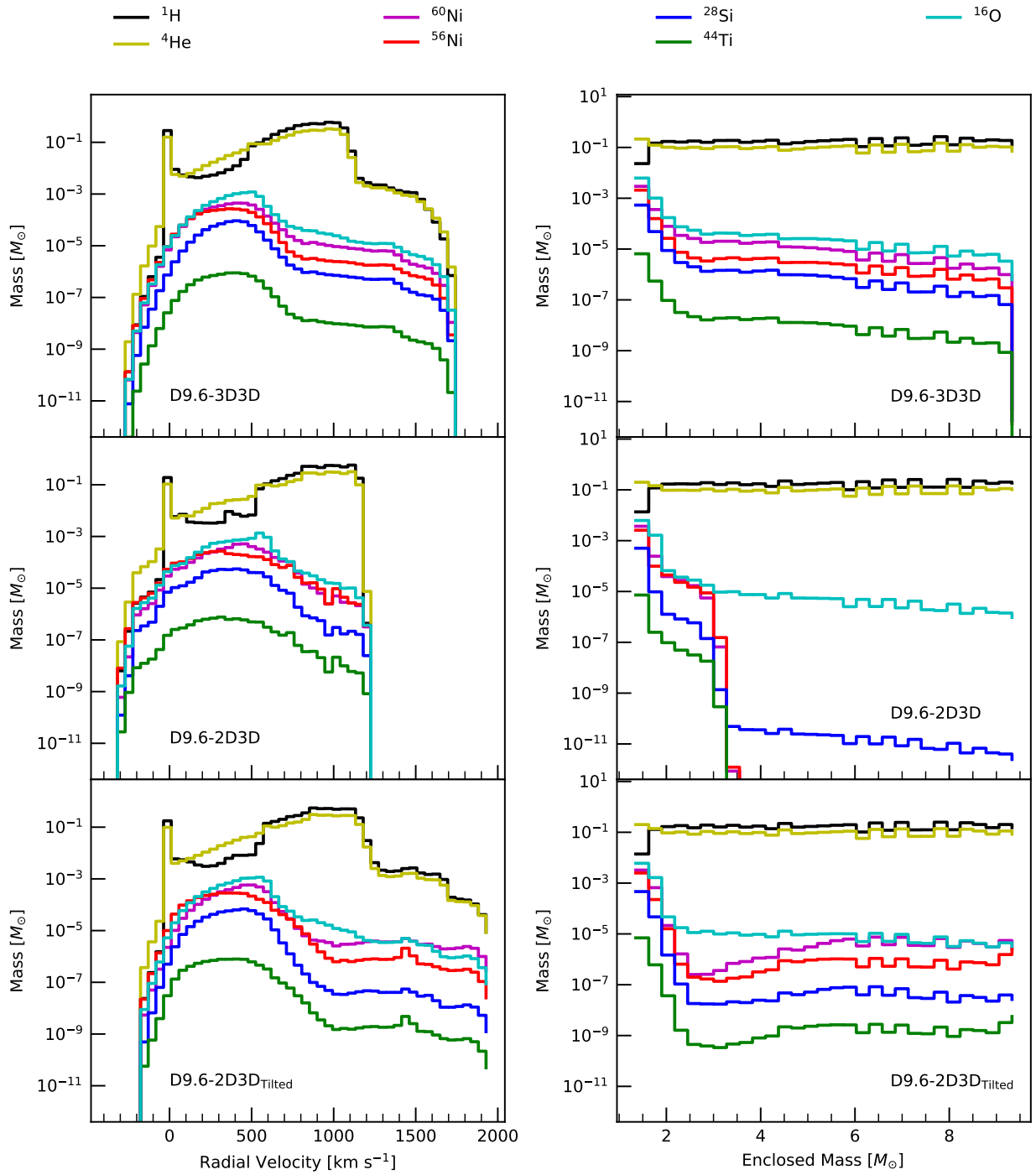

Figure 3.7: Mass yields of key isotopes binned across radial velocity (left column, 50 bins) and enclosed mass (right column, 30 bins) for each D9.6 model. Note, each bin is consistent across all models for both columns.

the distribution of these isotopes at the time of $t_{\rm map}$ from CHIMERA (Figure 2.6, left) makes this the most logical outcome. The explosion is surrounded by a shell of ^{12}C, ^{16}O, and ^{28}Si, but the two relevant Ni isotopes are distributed in such a way that the ^{56}Ni occupies the innermost ejecta whereas the ^{60}Ni is more extended (Figure 3.5, left). The extended ^{60}Ni features present at the time $t_{\rm map}$ grow into further extended structures as the explosion progresses, thus mixing more effectively in mass and velocity in the explosion.

Figure 3.8 provides a more detailed look at the compositional structure of the bullets. In the left panel of Figure 3.8, we plot the angular distribution of the composition of R-T plumes residing in the x-y-plane ($\theta = 90°$) at a constant radius of 4.0×10^7 km — marked as the dashed circle slicing the plumes at this radius in Figure 3.2(h). The right panel of Figure 3.8 displays the composition versus radius of a specific plume residing at $\phi = 18°$ in the x-y-plane. We choose this time (10000 s) for this inspection because the plumes are much more distinct in Figure 3.2(h) compared to their later appearance and the R-T plumes are simply expanding beyond this point in their evolution. In this plane, there exists six extended R-T plumes residing at 18°, 43°, 86°, 115°, 155°, and 171°. Two additional, less extended, R-T plumes can also be seen at 9° and 350°. All of the extended bullets are consistent in composition, having a ^{4}He coating that surrounds a metal-rich interior dominated by ^{56}Ni+IG. We find that in addition to the significant amount of ^{56}Ni+IG present in a single bullet ($X \simeq 0.07$) there also exists a substantial amount of ^{16}O ($X \simeq 0.02$) and lesser amounts of ^{66}Zn ($X \simeq 0.008$) and ^{28}Si present ($X \simeq 0.001$). The relatively large presence of ^{66}Zn in this model is representative of the enhanced α-rich, neutron-rich ejecta seen at the end of the CHIMERA run. (^{66}Zn is the neutron-rich upper limit of the sn160 network.) A closer inspection of the 18° bullet can be seen in the inset in the left panel of Figure 3.8. The vertical dashed lines indicate the angular positions of the edge of the 40% ^{4}He coating, and the intersection with the horizontal dashed line indicates what value this represents in $X_{^{56}\rm Ni+IG}$ (0.001 or 0.1%), demonstrating the correspondence between these isosurfaces. We will track the cocoon of ^{4}He that encases the heavy-element bullets in Section 3.1.3 by creating an isosurface at 0.1% $X_{^{56}\rm Ni+IG}$ instead of 40% ^{4}He, which allows us to analyze the evolution of the external coating without having additional noise at early-times from the He shell.

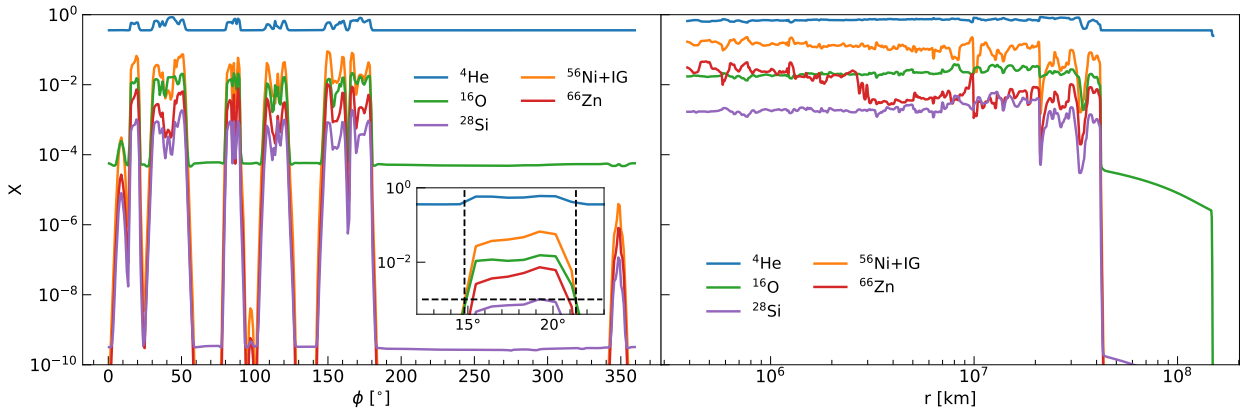

Figure 3.8: Left: Mass-fraction vs. azimuth at 10000 s in the x-y-plane ($\theta = 90°$) at a constant radius of 4.0×10^7 km. Inset: A magnified region of the 18° R-T plume. The horizontal dashed line marks a value of $X = 0.1\%$, and the vertical dashed lines mark the angular positions of the 40% $X_{^4\mathrm{He}}$ external coating. Right: Mass-fraction vs. radius along $\phi = 18°$ in the x-y-plane at 10000 s. Note the "head" of the plume is located between 3.5×10^7 km $\leq r \leq 4.1 \times 10^7$ km and the falloff of ^{16}O beyond this point is within the progenitor, not the R-T plume.

3.1.2 D9.6-2D3D

The D9.6–2D3D model exhibits similar behavior when it comes to the general progression of the shock front, yet differences can be seen when analyzing the leading R-T bullets. Although the Ni bullets are able to catch up to the rear of the shock, they are never able to fully interact with it in this model due to a sufficiently large gap in the relative velocity between v_{Shock} and v_{bullets}. This can be seen explicitly in Figure 3.1 in the shock and $X_{^{56}\text{Ni+IG}}$ velocity curves (green lines). The bullets are closest to the shock when the shock front hits the He/H interface at $\sim 1.0 \times 10^7$ km and $\sim$1000 s. The maximum velocity of the bullets in this model never rises above the average shock velocity in Figure 3.1, explaining why the plumes only minimally interact with the shock. Furthermore, in contrast to the D9.6–3D3D and D9.6–2D3D$_{\text{Tilted}}$ models, the maximum radial position of the $X_{^{56}\text{Ni+IG}}$ isosurface (Figure 3.9, upper edge of the green shaded region) always stays just below the curve representing the average position of the shock (green solid line), which highlights the absence of extended features. This minimal interaction leads to the scarcity of large-scale structures and asymmetries in D9.6–2D3D. Despite that D9.6–2D3D is mapped roughly 200 ms later than D9.6–3D3D and the explosion energy is $\sim$13% higher in D9.6–2D3D, the enhanced growth rate of the R-T plumes enabled by the 3D initial state allows D9.6–3D3D to retain higher velocity bullets.

The lack of macro-structure is apparent in the yields of key isotopes at shock breakout (Figure 3.7). The velocity distribution of the ejecta extends only to $\sim$1225 km s^{-1} in D9.6–2D3D, much less than the typical velocities associated with SN1987A and other CCSNe, and $\sim$30% lower in maximum velocity than D9.6–3D3D (1750 km s^{-1}) where the plumes interact with the shock. Because the shock is plowing through ^{4}He and ^{1}H, the shock can be seen as the "hump" in the ^{4}He curve centered at $\sim$1000 km s^{-1}, whereas the bulk of the bullets can be seen as the metal-rich hump further behind, peaking at $\sim$500 km s^{-1}. The gap between the humps shows how large the relative velocity between the shock front and metal-rich clumps is in D9.6–2D3D. The distribution gap in velocity further explains the inefficiency of mixing in mass space as well, with most of the metal-rich ejecta only extending to just within 4 $M_\odot$. Large-scale mushrooms are never spawned from the interaction of the shock

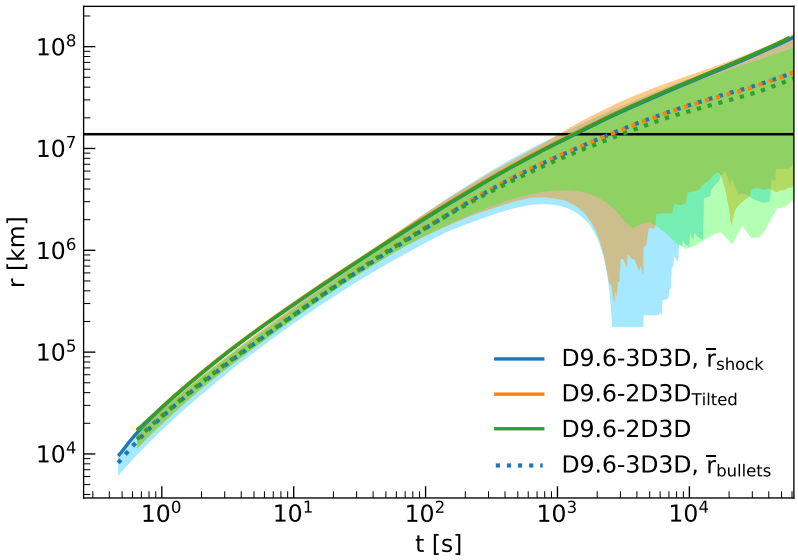

Figure 3.9: Angle-averaged shock radius (colored, solid lines) and angle-averaged bullet radius of the $X_{^{56}\mathrm{Ni+IG}} = 3\%$ isosurface (colored, dashed lines) as functions of time for the D9.6 models. Matching overlaid colored regions highlight the range of r_{min} to r_{max} of a model's respective bullet isosurface. Horizontal black line marks the radius of the He/H interface.

with the He/H interface, thus the metal-rich ejecta stays trapped behind the wall of He and is unable to extend its radial mixing.

The shock in D9.6–2D3D remains roughly spherical, even late in the evolution of the supernova. The D9.6–2D3D model is nearly identical to our D9.6–2D2D simulations, and this run can be viewed as, in essence, an axisymmetric simulation existing in 3D. Without transverse velocities in the 2D CHIMERA model, due to the initially assumed axisymmetry, true 3D behavior never develops (note the unbroken axisymmetry in Figure 3.10, left). However, the absence of structure in the shape of the shock is more than made up for by the amount of microstructure present in the inner regions containing the bulk of the R-T instabilities. This, in general, is similar to the results of Kifonidis et al. [53] and Wongwathanarat et al. [102] though with different progenitors. From a yields perspective, in both mass and velocity spaces, D9.6–2D3D is the most similar to the "3D3D" model presented in Stockinger et al. [84] which uses the same progenitor, referred to as "z9.6" (discussed further in Section 3.1.4).

3.1.3 D9.6-2D3D-Tilted

In light of the failure of the D9.6–2D3D model to break out from its 2D origin, we constructed the D9.6–2D3D$_{\text{Tilted}}$ model based on a simple coordinate transform. Similar to D9.6–3D3D, the D9.6–2D3D$_{\text{Tilted}}$ model establishes extended features in its explosion, which allows us to further investigate the morphology of this system. Features develop in this version of the "2D" model due to the evolution of a spherical-bubble structure rather than a pure toroidal structure imposed by axisymmetry. Tilting the original 2D CHIMERA model on its axis by applying a coordinate transform introduces longitudinal velocities into the previously 100% latitudinal velocity system. The presence of both longitudinal and latitudinal velocities seed the development of features in both coordinate directions. Hence, rotation of the angular velocities enables the explosion to deviate from the initial toroidal structure and start developing bubble-type features when forming the R-T bullets. Although only demonstrating a slight deviation initially, the bubble structures are able to retain higher velocities due to experiencing a lower drag to buoyant force ratio and deviate further from axisymmetry as

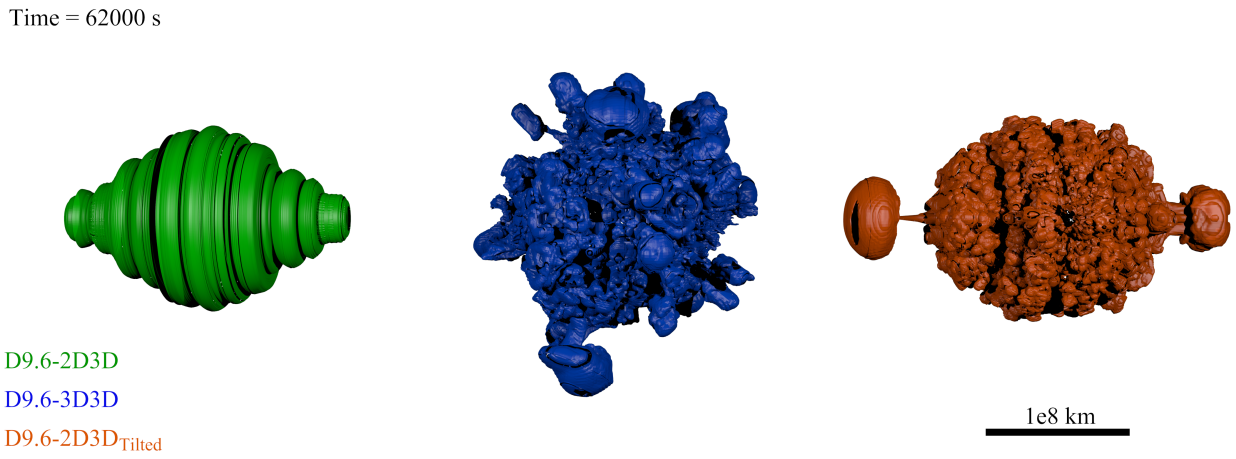

Figure 3.10: External coating $X_{^{56}\text{Ni+IG}} = 0.1\%$ isosurface for the D9.6–2D3D (green, left), D9.6–3D3D (blue, center), and D9.6–2D3D$_{\text{Tilted}}$ (orange, right) bullets at shock breakout. Note, the D9.6–2D3D$_{\text{Tilted}}$ isosurface has been realigned in post-processing (i.e. rotated clockwise about its y-axis 90°) to match the orientation of the other models.

the explosion progresses. Echoes of the axisymmetric origin persist, but they do not consume the entire model as with the D9.6–2D3D model. Side-by-side comparisons of all D9.6 models shown in Figure 3.10 demonstrate the true impact that tilting the model has on the resulting morphology of the explosion. Clearly, the D9.6–2D3D$_{\text{Tilted}}$ model, though retaining a grossly axisymmetric form, looks more like its true 3D counterpart, while the D9.6–2D3D model remains almost purely toroidal.

The similarities between D9.6–2D3D$_{\text{Tilted}}$ and D9.6–3D3D are also apparent in the distribution of radial velocity across the entire grid (Figure 3.11). Unlike D9.6–2D3D, both D9.6–2D3D$_{\text{Tilted}}$ and D9.6–3D3D have a significant number of grid cells occupying high-velocity space beyond a radius of 7.0×10^7 km. Additionally, the overall shape of the D9.6–2D3D$_{\text{Tilted}}$ distribution at larger radii looks similar to the D9.6–3D3D distribution, with a high peak of grid cells before the shock front resulting from the extended features produced in those models. Although obscured at lower radii by the D9.6–2D3D data, D9.6–2D3D$_{\text{Tilted}}$ and D9.6–3D3D are still consistent, where D9.6–2D3D is an outlier.

Analyzing the 3D surface area of the $X_{^{56}\text{Ni+IG}}$ isosurface shown in Figure 3.12 further illustrates the divergence between the D9.6–2D3D$_{\text{Tilted}}$ (orange lines) and D9.6–2D3D (green lines) models. The surface area representing the inner anatomy of the bullets (the 3% isosurface) is nearly identical for D9.6–3D3D and D9.6–2D3D$_{\text{Tilted}}$, while D9.6–2D3D quickly falls behind in the development of surface area. The divergence starts when the shock front encounters the He/H interface, because, once encountering this region, the D9.6–2D3D model does not have extended features penetrating the interface, which would significantly contribute to the surface area, while the other two models do.

The external coating of the bullets (represented by the 0.1% isosurface) is visualized in Figure 3.10 and displayed more quantitatively by the respective surface area curves in Figure 3.12 (dashed lines). Despite the formation of extended structures in D9.6–2D3D$_{\text{Tilted}}$, those features do not occupy as much overall surface area as in the D9.6–3D3D model, which can be seen in the isosurface plot. The biggest plumes in D9.6–2D3D$_{\text{Tilted}}$ do not grow as large as the biggest plumes in D9.6–3D3D, which affects the rate of change of the surface area. The largest contribution to the surface area occurs at the peak in the bottom plot of Figure 3.12, which represents the time that the bullets and shock hit the He/H interface.

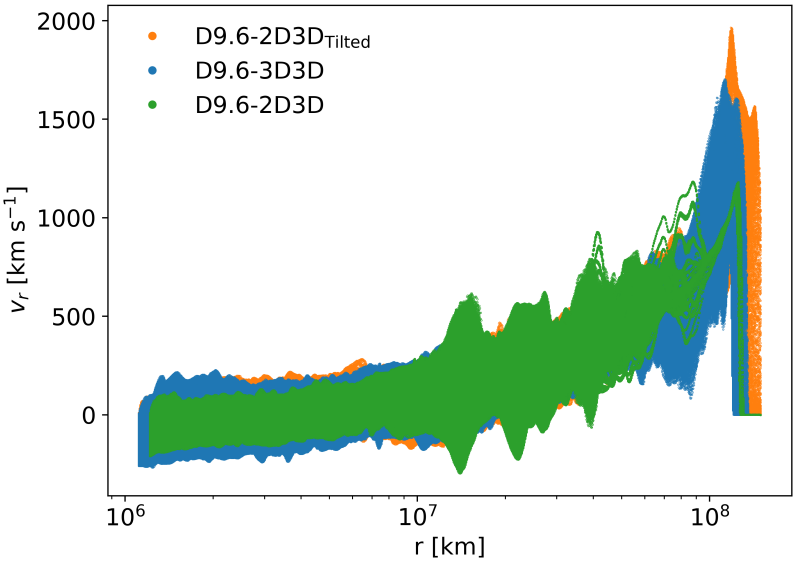

Figure 3.11: Scatter plot of radial velocity versus cell-centered radius for each grid cell at shock breakout for all D9.6 models.

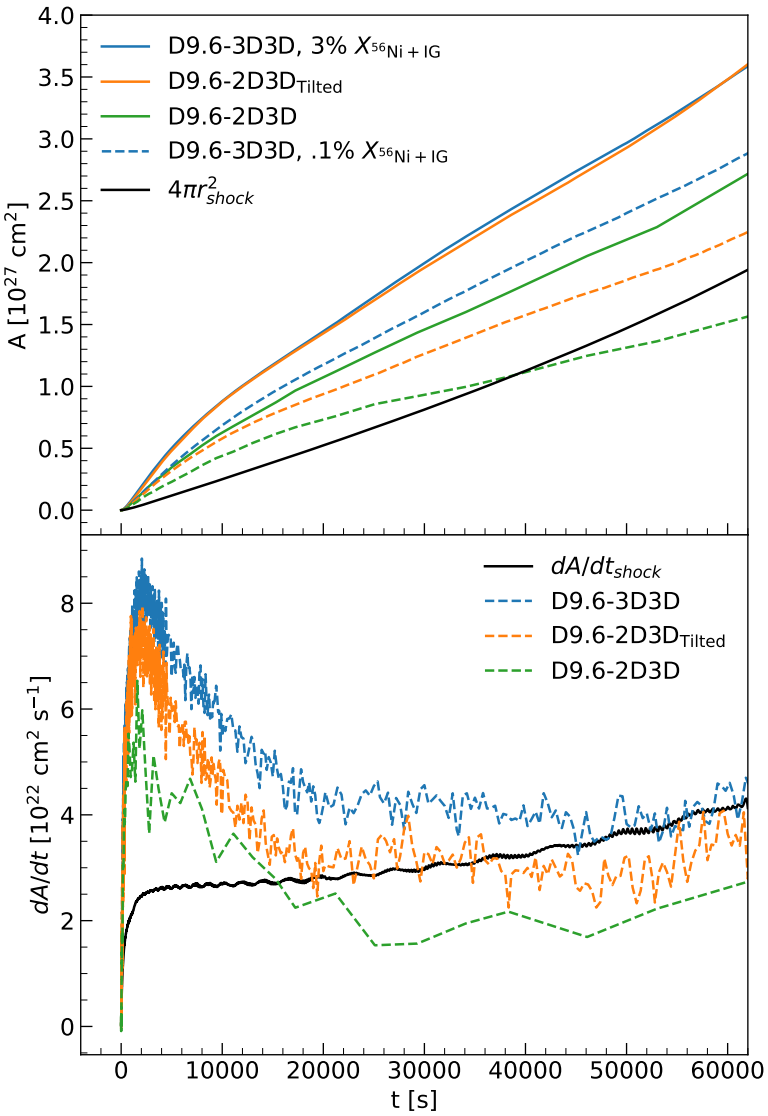

Figure 3.12: Top: Surface area of the $X_{^{56}\mathrm{Ni+IG}} = 3\%$ (colored, solid) and $X_{^{56}\mathrm{Ni+IG}} = 0.1\%$ (colored, dashed) isosurfaces for each D9.6 model. The average shock radii over time across all models are nearly identical, thus only the surface area of the D9.6–3D3D shock (black, solid) is included. Bottom: Numerical time derivatives of the surface area for the shock (black, solid) and $X_{^{56}\mathrm{Ni+IG}} = 0.1\%$ (colored, dashed) curves of the top plot. Note that the difference in file output in the D9.6–2D3D simulation has led to a less dense distribution of data points.

The addition of the He/H mass-shell to the coating of the bullets provides this boost due to the significant amount of extra volume it adds to the bullets. As the bullets expand, their surface area grows, and reaches a point near 10000 s where the slopes converge toward the contribution provided by shock expansion. The D9.6–2D3D model converges much faster, as it has no large plumes contributing to its evolution, whereas the other two models are able to stay above the shock expansion curve for longer. Although overall converging toward the contributions from the shock, the D9.6–2D3D$_{\text{Tilted}}$ model is able to achieve shock breakout while the total surface area resides above the curve represented by the shock (top panel of Figure 3.12). This does not occur in D9.6–2D3D, as the total surface area is dominated by the shock starting at ∼40000 s while almost all of the bullets are trapped behind the He/H mass shell and constantly outpaced by the shock.

Although the external coating isosurface tracks the larger structures of each model, its surface area contribution is not as large as the 3% isosurface. This is due to the fact that, while the 0.1% tracks larger structures that produce overall greater individual contributions, the amount of smaller individual contributions from the 3% isosurface is more numerous and builds up to occupy more of the volume, thus representing a larger total surface area.

The overall radial progression of the shock for all three models is nearly identical whether viewed as average shock radius relative to velocity (Figure 3.1) or time (Figure 3.9). Similar to the D9.6–3D3D model, D9.6–2D3D$_{\text{Tilted}}$ develops its larger scale features in the middle of the He shell near 1.0×10^6 km. This can be seen explicitly in Figure 3.1, as the maximum velocity of the bullets surpasses the average shock velocity. The same type of variations in the velocity profile after 1.0×10^6 km occur in the D9.6–2D3D$_{\text{Tilted}}$ model as they did in D9.6–3D3D before the velocity of the bullets steadily decline while penetrating through the shock until shock breakout is achieved. The plume penetration into the shock is seen further in Figure 3.9, as the bullets' maximum radial extent in the D9.6–2D3D$_{\text{Tilted}}$ model (orange shaded region) surpasses the average shock radius and even exceeds that of the equivalent highlighted range in the D9.6–3D3D model. The average radius of the $X_{^{56}\text{Ni+IG}}$ clumps in the D9.6–2D3D$_{\text{Tilted}}$ model is nearly identical to that of D9.6–3D3D, while the D9.6–2D3D model deviates around 60 s — the time when D9.6–2D3D$_{\text{Tilted}}$ and D9.6–3D3D form their large-scale structures.

Due to the formation of extended features in D9.6–2D3D$_{\text{Tilted}}$, this model bridges the gap between the D9.6–2D3D and D9.6–3D3D yields of metal-rich ejecta in both mass and velocity spaces (see Figure 3.7, lower panels). Not only is the extent of radial mixing similar to that of D9.6–3D3D, but the maximum velocity of the high-velocity tail is 200 km s^{-1} *larger* than the D9.6–3D3D model (1950 km s^{-1}), a remnant of the large-scale axisymmetry in this model. Once again, the bulk of metal-rich bullets peak at ∼500 km s^{-1} and 1.0×10^{-4} $M_{\odot}$. The dominant isotope of the iron group in D9.6–2D3D$_{\text{Tilted}}$ is ^{60}Ni, matching the D9.6–3D3D model. The total yields are relatively consistent across all models (Table 3.1), with the largest differences arising due to evolution within CHIMERA for the FLASH 2D initial condition, while also having a different t_{map} than the 3D initial condition. Additionally, we see relatively low mass loss across all models, $\sim 7 \times 10^{-4}$ $M_{\odot}$ lost, where ∼1.5% of this is due to the moving inner boundary (removal of innermost grid cells), and the remaining ejecta lost is due to fallback (matter falling through the inner boundary), most of which is ^{4}He ($\sim 3 \times 10^{-4}$ $M_{\odot}$).

3.1.4 Comparison to Previous Studies

Previous works have also studied supernovae from the same progenitor as our D9.6 models, but only one has studied the long-time evolution. Stockinger et al. [84] started from the Melson et al. [60] simulation of the neutrino heating phase using similar microphysics in 3D in their version of the 9.6 $M_{\odot}$ progenitor, but with a smaller nuclear network (15 species + n + p) and lower resolution than our initial state (see Section 2.3). They report metal-rich clumps centered around ∼300 km s^{-1} and extending to a maximum of ∼500 km s^{-1} in velocity space, which is clearly slower than our high-velocity tails extending to 1225 km s^{-1}, 1750 km s^{-1}, and 1950 km s^{-1} for D9.6–2D3D, D9.6–3D3D, and D9.6–2D3D$_{\text{Tilted}}$, respectively. The lower clump velocities in their run also lead to less efficient radial mixing with the metal-rich ejecta only falling within the inner 2 $M_{\odot}$. These results are starkly different than the results of our respective D9.6–3D3D model, which shows mixing to the surface, and are less well mixed than even our simulations initiated from 2D CHIMERA models.

We believe that the notable differences in Stockinger et al. [84] derive from the lower overall diagnostic explosion energy reported at their t_{map}, for our initial energy is ∼95%

Table 3.1: Total D9.6 Yields At Shock Breakout

Species	2D3D $[M_\odot]$	3D3D $[M_\odot]$	$2D3D_{\text{Tilted}}$ $[M_\odot]$
^{1}H	4.995	4.958	5.017
^{4}He	3.052	3.023	3.056
^{12}C	2.290×10^{-2}	2.227×10^{-2}	2.226×10^{-2}
^{16}O	8.125×10^{-3}	8.050×10^{-3}	7.974×10^{-3}
^{28}Si	5.118×10^{-4}	6.181×10^{-4}	5.157×10^{-4}
^{44}Ti	7.557×10^{-6}	7.446×10^{-6}	7.705×10^{-6}
^{48}Ca	1.563×10^{-4}	1.419×10^{-5}	1.605×10^{-4}
^{52}Fe	2.777×10^{-5}	2.955×10^{-5}	2.820×10^{-5}
^{56}Ni	2.712×10^{-3}	2.337×10^{-3}	2.767×10^{-3}
^{60}Ni	4.013×10^{-3}	3.669×10^{-3}	4.044×10^{-3}
^{66}Zn	1.383×10^{-3}	1.142×10^{-3}	1.399×10^{-3}
Iron Group$_{\text{NR}}$	1.157×10^{-2}	1.060×10^{-2}	1.174×10^{-2}

Note. — Iron Group$_{\text{NR}}$ is defined as all species in our network falling in the range of ^{49}Cr–^{64}Ni, while excluding ^{52}Fe and ^{56}Ni. Only cells with a positive radial velocity are considered. This table, with all 160 species, is located in Appendix A. The species listed above are a selection of the content presented for analysis.

larger in the 3D3D case and even larger in the 2D3D cases. Consequently, our shock achieves breakout nearly 12 hours sooner than their reported breakout of ∼31 hours, which is an approximately 60% difference compared to our shock escape before rewinding (∼19.4 hours). The weaker overall explosion helps explain why their model does not produce large structures during its evolution, despite it being a 3D model starting with 3D initial conditions. The relative velocity gap is too large between the shock front and the leading metal-rich bullets, which enables the R-T plumes to get trapped behind the He/H mass shell as opposed to spawning large features from it (similar to our D9.6–2D3D model, but to a greater extent). This is seen explicitly in Figure 13 from Stockinger et al. [84] (equivalent to our Figure 3.1), where their isosurface of $X_{^{56}\mathrm{Ni+Tr}}$ never reaches maximum velocities that are larger than their average shock velocity. Further comparison can be seen in Figure 20 from Stockinger et al. [84] (equivalent to our Figure 3.4), as our bullets look distinctly more elongated while propagating through the He shell.

The total yields at shock breakout for D9.6–3D3D (Table 3.1) are relatively comparable to those listed in Stockinger et al. [84]. However, differences can be seen in the form of ^{28}Si, ^{56}Ni, and the iron group tracer material. The amount of ^{28}Si present at the end of our simulation is 128% greater than that reported by Stockinger et al. [84]. They report approximately 68% more ^{56}Ni than our total, which may result from the inclusion of the mass of all iron-group species not included in their network increasing the ^{56}Ni yield, as they discuss. Overall, the amount of neutron-rich iron group material across all of our models is larger by an order of magnitude (∼900%). Considering the amount of ^{60}Ni present in our model, and that it has essentially "replaced" ^{56}Ni as the traditional bullet material in this simulation, we see comparable or greater total nickel and iron group yields.

Neutron-rich iron peak isotopes are an area where the sn160 network we employed has significant advantage over the smaller network of Stockinger et al. [84], even with their tracer species. Since we see little mass loss of the ejecta during our extended FLASH runs and no significant formation of iron group nuclei during our short period of nuclear burning, the main cause of the discrepancy in the yields seen at shock breakout between D9.6–3D3D and Stockinger et al. [84] must be how the species were evolved in the CHIMERA and VERTEX-PROMETHEUS portions of the runs. As Stockinger et al. [84] also initiated their shock

breakout run from an early-time CCSN simulation [60], and because there is no discussion of notable mass loss during their late-time evolution, we stress how critical the initial conditions are in this yields comparison.

To a lesser extent, we believe that our higher resolution also impacts the morphology of the system. As we will discuss further in Section 3.2.1, resolution directly affects the number of R-T plumes spawned when a mass shell fragments. The fragmenting phenomenon determines how the shock front is able to be reshaped by the metal-rich bullets. A greater number of extant R-T plumes allows for more shock interaction across the entire domain, directly affecting the development of large-scale features. However, a more extensive resolution study is required to support this supposition.

For a more general comparison of our D9.6–3D3D model, we look to the morphology analysis in Wongwathanarat et al. [102], who categorized the late-time metal-rich ejecta into three types: (1) small clusters of R-T bullets having the fingerprint of early-time asymmetries as in their 15 $M_\odot$ red supergiants (RSGs); (2) fragmented and squished round features as in their 20 $M_\odot$ blue supergiant (BSG); and (3) long extended fingers as in their two 15 $M_\odot$ BSGs. Our RSG D9.6 simulations don't seem to fall *completely* into one of these regimes, but the reasoning outlined by Wongwathanarat et al. [102] does explain why our models look the way they do. In their 15 $M_\odot$ BSG models, the steep rise of ρr^3 inside the He layer causes a steady deceleration of the shock front as it propagates, and the acceleration/deceleration at the He/H interface is nearly non-existent. This allows the bullets to stay close behind the shock and avoid interaction with any of the reverse shocks. This is the type of density profile found in D9.6–3D3D, as the metal-rich bullets are able to catch up to the rear of the shock in the middle of the He layer due to higher maximum velocities than the average shock velocity.

Despite the presence of extended features in our simulation, they are not as extreme and distinct as those produced by the 15 $M_\odot$ BSG simulations of Wongwathanarat et al. [102]. Our features look like slightly more extended versions of their clustered RSG fingers. These clustered structures are associated with early-time asymmetries, and are clearly visible in Figure 3.5, however, the journey for our clumps is different. In Wongwathanarat et al. [102], the large gap between the shock and the trailing bullets allows for more momentum

to build before they collide with the reverse shock produced by the dramatic deceleration at the He/H interface, which does not occur in our simulations due to the smoother density profile of the D9.6 progenitor. The development of the bullet shape is strongly impacted by the interaction of the fingers with reverse shocks, which squash the clumps. Because the majority of our R-T plumes spawned ahead of the first reverse shock and out of the first mass shell, they completely avoid any reverse shock interaction. (The second reverse shock also forms behind the bullets.)

As important as the dynamics of the reverse shock are, neither Stockinger et al. [84] or Wongwathanarat et al. [102] discuss the phenomenon of the first reverse shock setting up a point-like rebound blast wave as it approaches the inner boundary as seen in our D9.6 models. We suspect that this event is missing due to how they moved their inner boundary. As discussed in Section 2.2, we mimicked Wongwathanarat et al. [102] in the handling of our inner boundary of the grid, but used a 1% of shock radius criterion as opposed to their 2%. This means we waited longer to move our boundary, thus allowing more accurate interactions near the center of the grid. If the collapsing reverse shock encounters the inner boundary when its radial excision is too large, then the reverse shock does not have the opportunity to set up a point-like blast and instead exits the grid. Regardless, the impact of this event on the morphology of the system, and its interaction with the PNS wind, needs to be explored further.

3.1.5 Preliminary Particle Results

As discussed in Section 2.7, tracer particles were present in the D9.6–3D3D simulation, which enables us to track the overall flow and evolution of the ejecta on a closer scale. However, due to unforeseeable time constraints, the amount of post-processing on the particles is minimal and limited to a general overview.

Prior to mapping into FLASH, there was a total of 295059 particles within the CHIMERA simulation, of which only 46002 were mapped into FLASH. The missing particles after mapping were due to the cutouts present on the FLASH grid – 155 particles were lost due to the 5° cutout along the poles of the grid and the remaining missing particles fell inside the 500 km inner radial boundary. Figure 3.13 displays the evolution of the total particles in

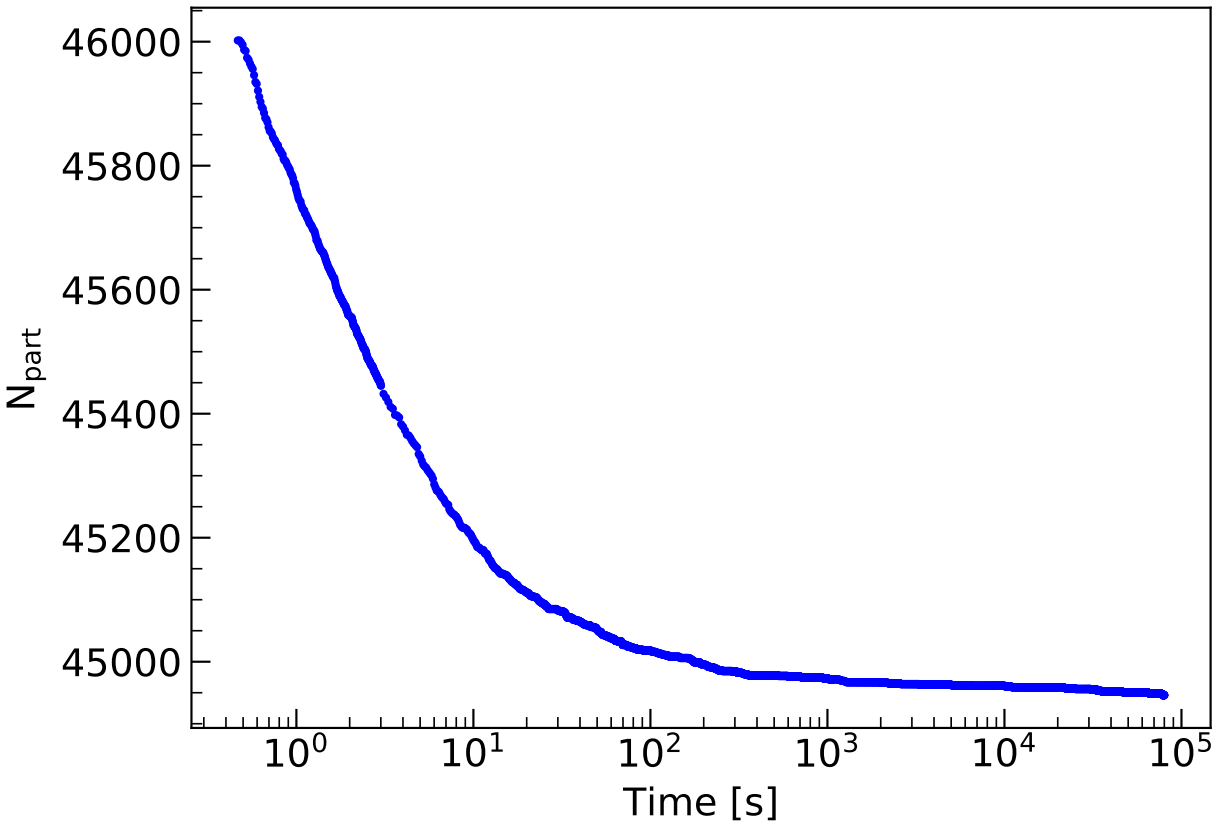

Figure 3.13: Total particles versus time for the D9.6–3D3D model.

FLASH across the entire simulation. Of the 46002 FLASH particles, 44946 particles remain on the grid at the end of the simulation, which corresponds to 1056 particles lost for the entire run (∼2.3% of the initial FLASH particles). Most of the particle loss (>50%) occurs within the first 3 s of the simulation, and >75% of the particle loss occurred within 10 s. The remaining particle loss occurred slowly over the rest of the simulation, and only bound particles were lost within ∼2600 s. Concerning the moving inner radial boundary's affect on losing particles, only 12 particles across the whole simulation were lost due to this method (three of which were unbound, and nine were bound).

Analyzing the initial and final bound states of the particles shines light on the initial particle predictions of CHIMERA by revealing how many particles end near the surface of the star versus how many particles end close to, or have already been captured by, the PNS. As work is still ongoing, we only have the final bound states of the *lost* particles during the simulation. The majority of the particles lost in FLASH were bound particles (1037 particles), where the remaining 19 lost particles were unbound (i.e. expected to be part of the ejecta). Three of the unbound particles were victims of being at the wrong place at the wrong time and were removed from the grid by the moving inner boundary. An additional three unbound particles were lost due to escaping the outer boundary as they resided at the forefront of the shock. The remaining 13 unbound particles had slightly negative velocities (see Figure 3.14), and were most likely in the process of transitioning to a bound state in between output files. Unfortunately, we only know the properties of a lost particle the output file *before* it leaves the grid, which leaves a gap in its history. Regardless, we are not concerned with the loss of the unbound particles, as they only made up ∼1.8% of the missing particles and – most importantly – the temperatures of these particles were relatively cold ($< 10^7$ K, see Figure 3.15). The loss of the bound particles is negligible as their final fate belongs to the PNS.

An additional area of interest is analyzing a particle's trajectory through the star. A particle does not simply propagate outward in a ray, for the hydrodynamic flow is not that simple. With all the instabilities forming in the simulation, particles will follow this flow and have a dynamic journey to the surface of the star. Figure 3.16 shows the trajectory of a single particle, particle number 277788, which is colored by the particle's temperature. This

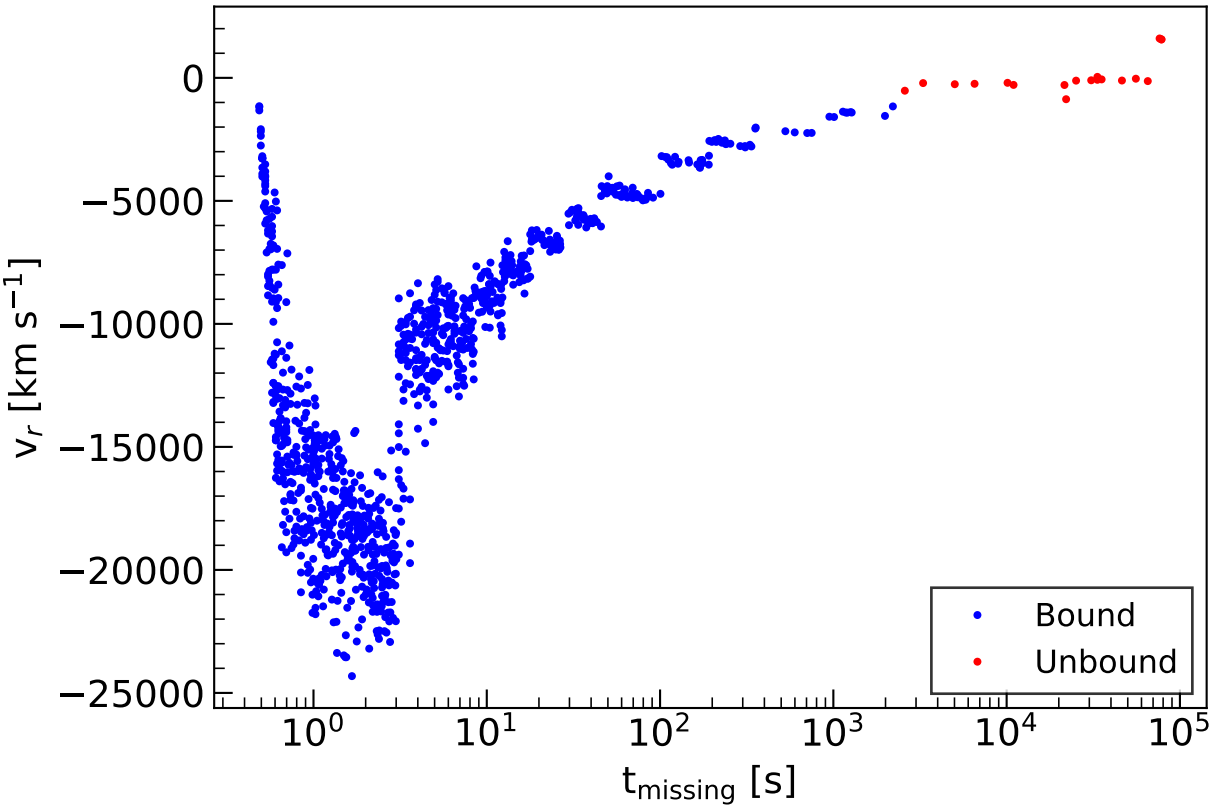

Figure 3.14: Final velocities of lost particles versus the time the particle left the grid in the D9.6–3D3D simulation. Note that the nearly discontinuous jump at ∼3 s is due to a change in stride of output files.

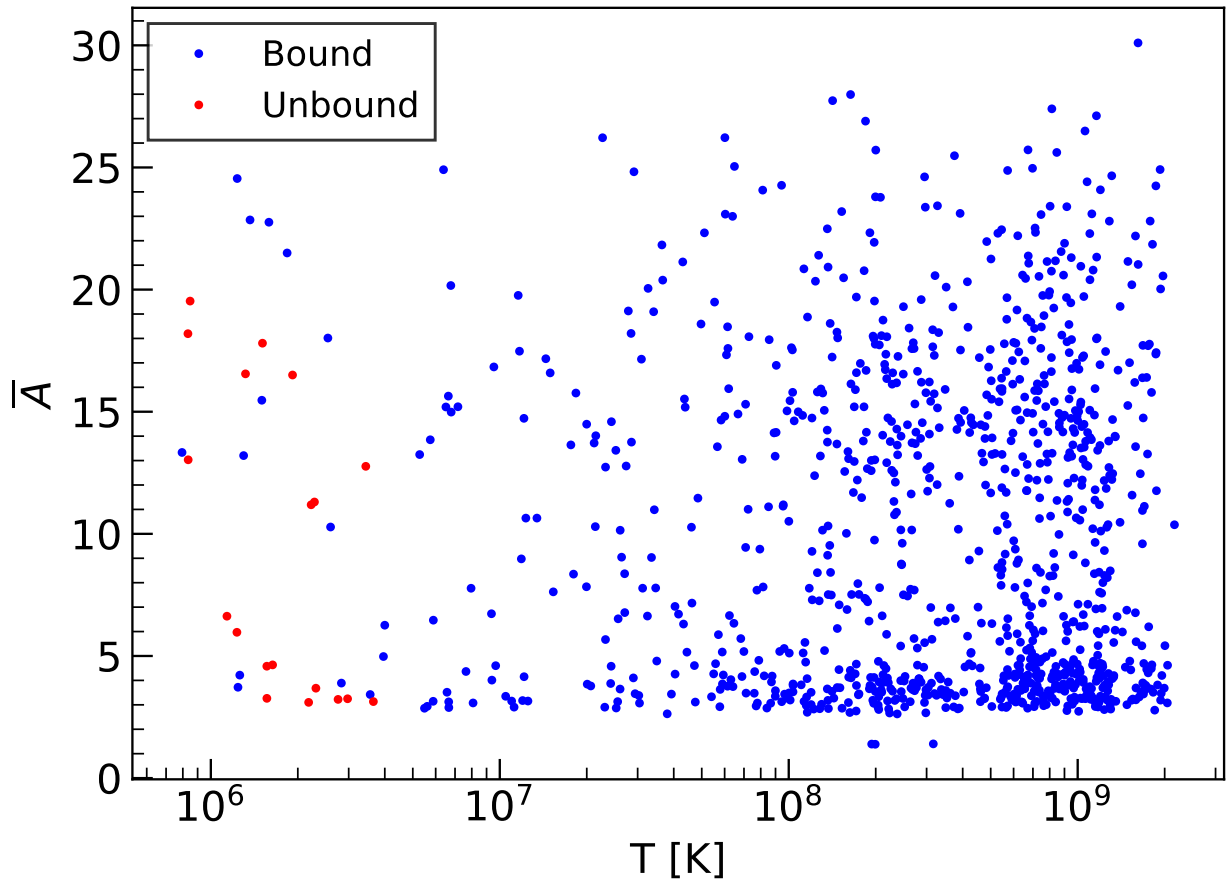

Figure 3.15: Final temperature versus final $\overline{A}$ (mean mass number) of lost particles in the D9.6–3D3D simulation.

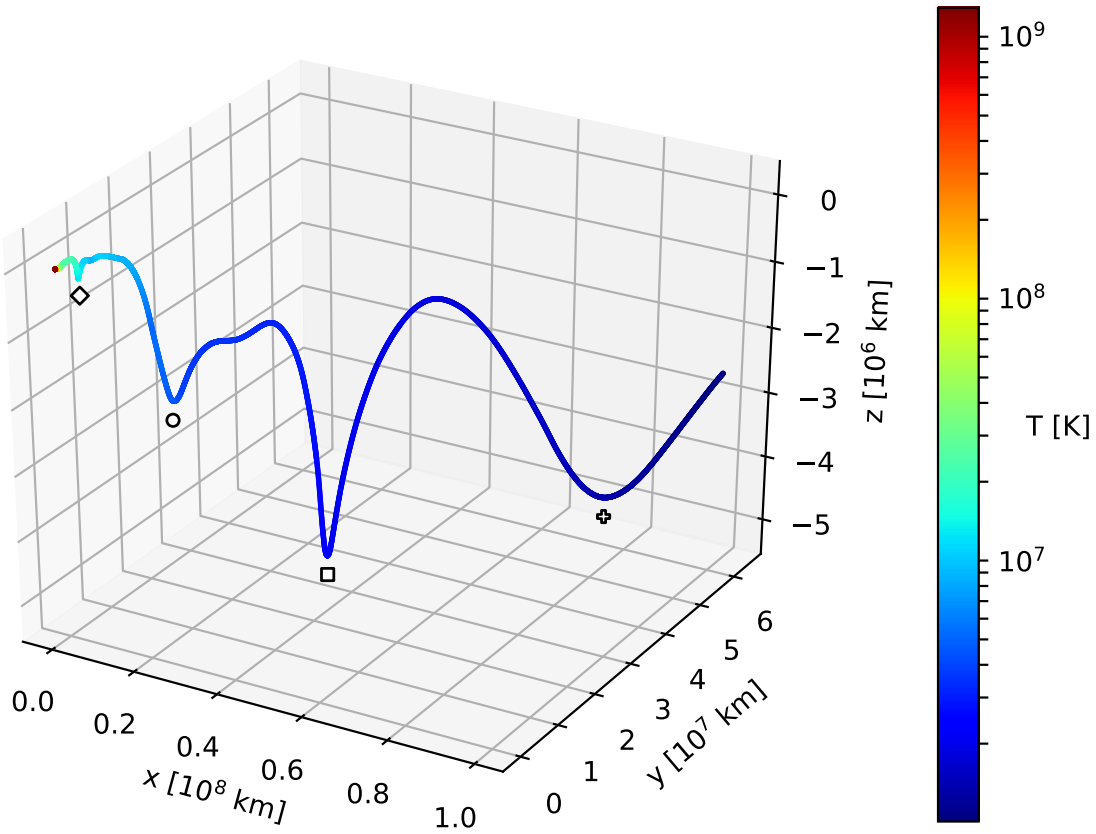

Figure 3.16: Trajectory of particle 277788 in the D9.6–3D3D simulation, colored by temperature in Kelvin. The white diamond, circle, square, and cross indicate where the particle penetrated the shock, encountered the He/H interface, saw a change in density gradient in the H shell, and encountered the density falloff at the edge of the star, respectively.

specific particle was chosen because it inhabited one of the biggest R-T mushrooms at the end of the explosion (see Figure 3.17). Because the particle resided in one of the main R-T bullets, the variations in the particle's path in Figure 3.16 are due to the particle responding to the density structure of the star just like the R-T bullet. More specifically, the extreme deviations seen around the markers in Figure 3.16 are due to the particle encountering key locations in the star, similar to the R-T bullet analysis in Section 3.1.1 of Figure 3.1. The first point of interest, the white diamond, is when the particle responds to its R-T bullet penetrating the rear of the shock front. The white circle marks where the particle responded to hitting the He/H interface (also see middle panel of Figure 3.17). The R-T bullet, after this point, grows much larger and establishes quite a robust mushroom cap. As the vorticity of the fluid further develops the head of the mushroom, the particle responds to this process, represented by the small wiggles after the white circle (but before the white square). The particle, and the R-T bullet, then encounter a slope change in ρr^3 at the white square as they both approach the outer regions of the star. Finally, at the white cross, the particle and its bullet start to fall off the density "cliff" and accelerate to the edge of the star. The final distribution of the particles, along with particle number 277788 highlighted, can be seen in the bottom panel of Figure 3.17. One can see that studying a particle's trajectory provides a different approach to analyzing the R-T bullets of the system. More work is being done on the particles, and their trajectories, in hopes of creating a correlation between where the particles are initially distributed versus where they reside at the end of the explosion.

3.2 D10 - Results

In this section, the results of the D10–2D3D simulation (Section 3.2.1) and D10–2D3D$_{\text{Tilted}}$ simulation (Section 3.2.2) are presented in sequence.

3.2.1 D10-2D3D

Here we discuss the general progression of the shock in the D10–2D3D model. Model D10–2D3D was mapped into FLASH at a much later t_{map} ($\sim$1.76 s), as nuclear burning ceased much later in this explosion compared to the D9.6 models. In addition, the shock front in the

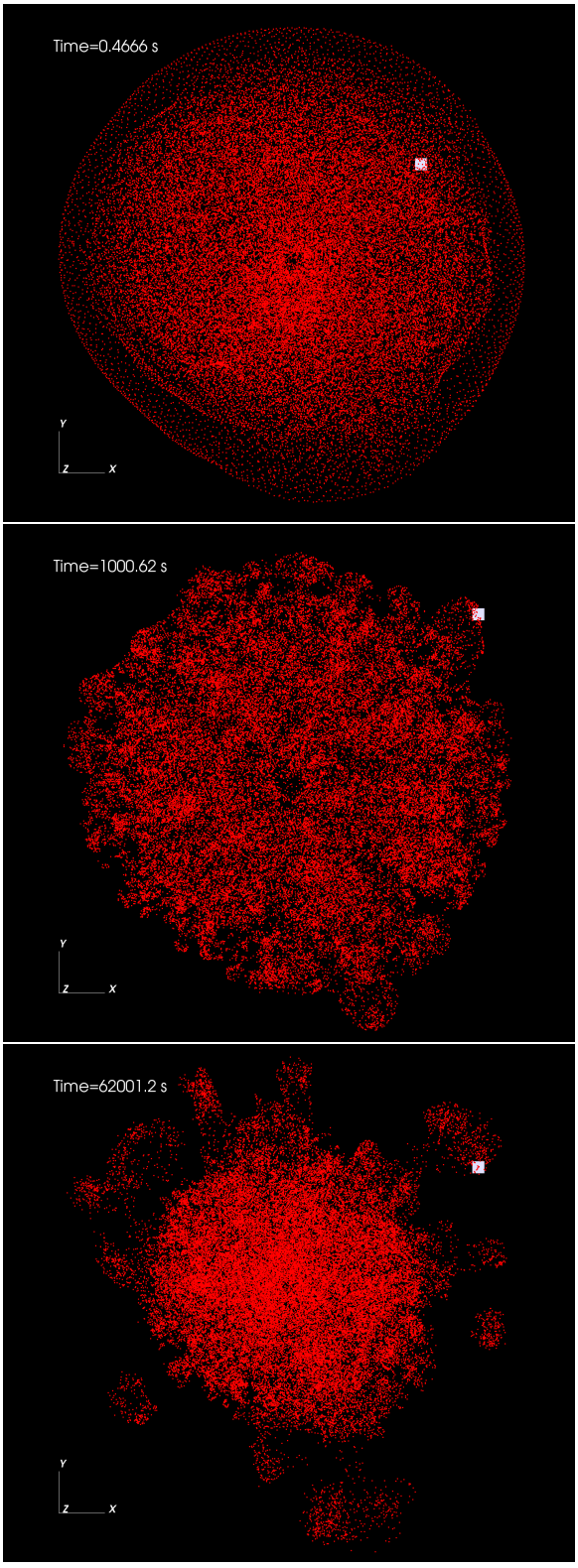

Figure 3.17: Time snapshots of the particle distribution in the D9.6–3D3D simulation (red), with particle 277788 highlighted (white). Top: The initial distribution. Middle: Encountering the He/H interface. Bottom: End of the simulation.

D10 is significantly more aspherical from the start (Figures 3.18(a) and 3.19(a)) compared to the D9.6 (Figures 3.2(a) and 3.3(a)). This is a common feature in 2D models of iron core-collapse supernovae, because the development of the explosion depends on the development of large plumes that can deliver energy from the regions of most intense neutrino heating to the shock. The three big convective plumes have already shaped the shock front at $t_{\rm map}$ and will eventually create shear Kelvin-Helmholtz (K-H) instabilities at the interface between the dominant plumes later in its evolution. At $t_{\rm map}$, the mean shock radius is $\sim 2.5 \times 10^4$ km, just across the (C+O)/He interface, and is now in the former He-burning shell. Unlike the D9.6 simulations that have essentially two phases to the shock progression (pre- and post-He/H interface), the D10 progenitor's density profile gives rise to four distinct phases of evolution. Fragmentation of the (C+O)/He shell (phase one) is followed by the acceleration of the shock away from carbon encompassed ejecta (phase two), where this material gets injected into the rear of the fragmenting He/H shell after the shock's deceleration (phase three) before slowly expanding to shock breakout (phase four).

Starting with phase one, the shock is still briefly accelerating after crossing the (C+O)/He interface, which creates a large reverse shock from the subsequent deceleration once fully into the He-burning shell. This reverse shock is coupled with the location of the mass shell that once marked the (C+O)/He interface, analogous to D9.6's first reverse shock. This promptly shreds and shapes the inner ejecta, as it starts to propagate inward in mass and soon in radius. The aspherical shock hits the (C+O)/He interface at slightly different times, leaving a fingerprint in the form of nonuniform fragmentation in its wake. Four main R-T plumes are quickly spawned (ignoring the poles), which are reminiscent of the dominant plumes that caused the shock to hit this composition interface, unlike the many small R-T plumes seen in D9.6. The main R-T plumes are located at approximately 20°, 35°, 80°, and 130° from the right pole as seen in Figure 3.18(b) and more distinctly in Figure 3.18(c). Of this "phase one" material, three out of the four plumes are significantly metal-rich (red features in Figure 3.19(c) at 20°, 35°, and 130°), while the last bullet is rich in ^{12}C (the darker blue plume at 80°). These features are mirrored due to the axisymmetry of the initial state and we will omit the mirror features from further discussion because they exhibit the same behavior as their original counterparts.

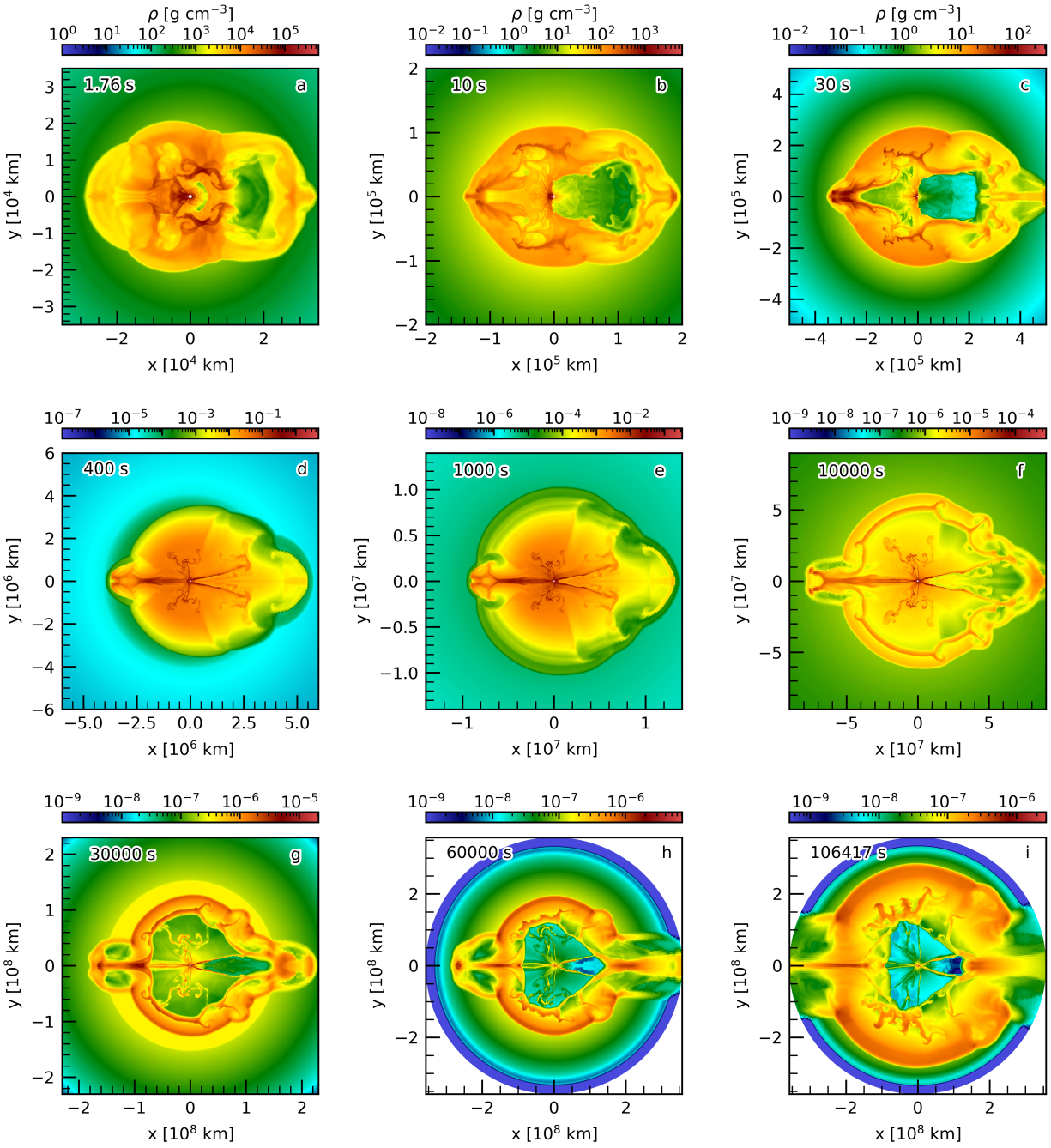

Figure 3.18: Slices of density in the D10–2D3D$_{\text{Tilted}}$ model at the displayed times. Note the changes in axis scale and color bar to accommodate the expanding shock. These slices are also consistent with the morphology of the D10–2D3D model at the given times. The blue to green color discontinuity ahead of the shock in panel (d) represents the position of the He/H interface.

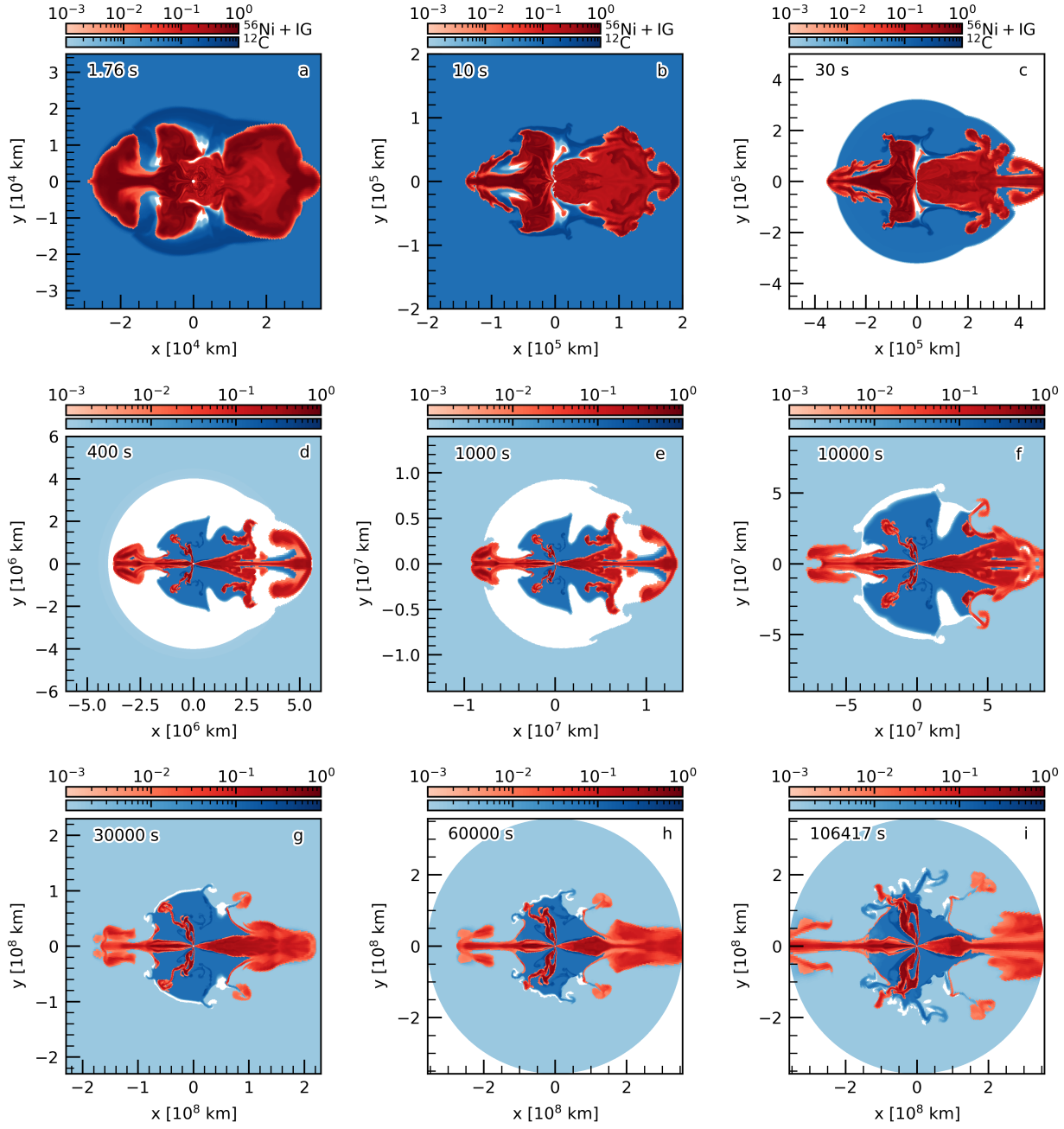

Figure 3.19: Slices of $X_{^{56}\mathrm{Ni+IG}}$ (red) overlaid on $X_{^{12}\mathrm{C}}$ (blue) in the D10–2D3D$_{\mathrm{Tilted}}$ model at the displayed times (same times as Figure 3.18). These slices are also consistent with the morphology of the D10–2D3D model at the given times. Note that the different colors help highlight the distribution of ejecta from the various phases of evolution described in Section 3.2.1. Red highlights the distribution of phase one, dark blue highlights phase two, and white (material not captured by the limit threshold of either colormap) can be viewed after panel (d) as highlighting the phase three fragmenting shell.

By 30 s, the shock reaches the density interface at the transition from the He-burning shell to the rest of the He layer (Figures 3.18(c) and 3.19(c)). Due to the dramatic change in ρr^3, the shock encountering this shell starts an acceleration that continues until the shock has fully entered the hydrogen envelope (see change in v_{Shock} starting at $\sim 3.5 \times 10^5$ km in Figure 3.20). The He-burning shell can be seen throughout the remaining evolution of the explosion as it is propelled forward by the shock. The enhanced ^{12}C from partial He-burning appears as a dark blue carbon "bubble" surrounding the inner ejecta in Figure 3.19(c) at $\sim 3.0 \times 10^5$ km while it interacts with the unburned He shell, similar to the helium bubble surrounding the inner ejecta in the D9.6 simulations. The unburned He shell in Figure 3.19 appears white (lower than the colormap limit of 10^{-3}), as it has converted its ^{12}C to ^{14}N via the CNO cycle. At this point we have entered phase two.

During phase two, until hitting the He/H interface, the shock front significantly outpaces the inner ejecta. By 60 s, the four main R-T fingers stretch with extremely thin stems at the base while the reverse shock collapses the material behind them. Previously the carbon bubble kept the shape of the shock front, but now the bubble starts to shear at one of the points on its perimeter where the uneven spherical arcs of the shock front hit it prior (at the shock triple point seen earlier at $\sim 50^\circ$ in Figures 3.18(c) and 3.19(c)). This starts to split the bubble and drive a physical wedge between the inner ejecta, which eventually develops into the dramatic dip seen at much later times in the northeastern quadrant of the dark blue bubble in Figures 3.19(d), 3.19(e), and 3.19(f).

At $\sim$250 s, the entirety of the first reverse shock has reached the inner boundary of the grid (now at $r = 3.4 \times 10^4$ km) as we near the end of phase two. By this point, the inner ejecta has been completely collapsed by the reverse shock, with all shape and distribution either being huddled close to the inner boundary, or pushed into the four main R-T fingers. The first reverse shock approaches the inner boundary significantly more centered about the origin than in the D9.6 models, thus most of it is carried off the grid as opposed to colliding with itself and creating a point-like explosion as seen in the D9.6 models. Because of the irregular shape of the first reverse shock, sections of it reach the inner boundary at different times (with the earliest portion reaching the center at $\sim$100 s), which further enables the opportunity to evade collision. The only collision that occurs is the portion of the reverse

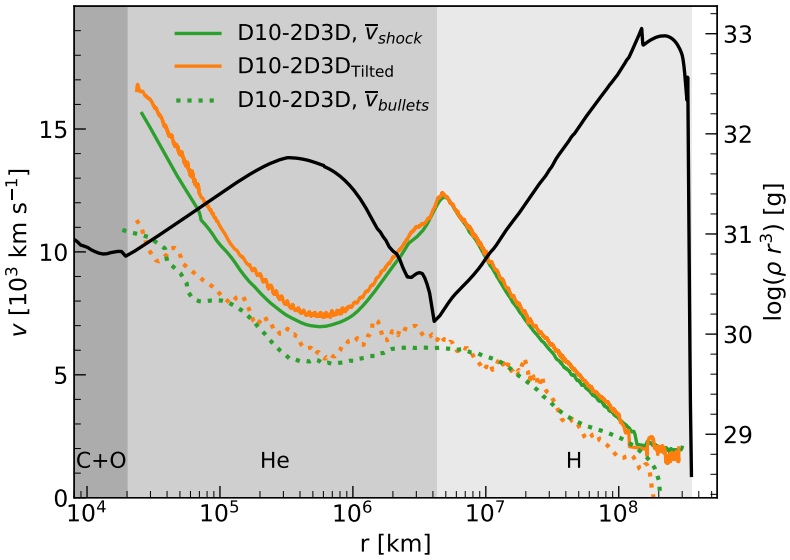

Figure 3.20: Angle-averaged shock velocity (colored, solid lines) and angle-averaged bullet velocity of the $X_{^{56}\mathrm{Ni+IG}} = 3\%$ isosurface (colored, dashed lines) for the D10 models as functions of their respective angle-averaged shock or bullet radii. Density profile of the D10 progenitor prior to bounce (black, solid) displays the change of ρr^3 and spans the right axis. Grey shaded sections highlight the regions of the (C+O), He, H shells up to the defined R_{Int} in Table 2.1.

shock produced along the poles that are able to avoid the inner boundary and start to impede the collapsing pressure waves on the opposite side.

Phase three begins at ∼400 s (Figures 3.18(d) and 3.19(d)) when the main shock encounters the He/H interface and launches a strong reverse shock due to the significant shock deceleration (see in Figure 3.20 the sharp change in $v_{\rm Shock}$ at $\sim 4.5 \times 10^6$ km). The second reverse shock is coupled to the location of the mass shell of the He/H interface, unlike the decoupled second reverse shock in the D9.6 models. This shell starts to fragment quickly, with an R-T instability forming promptly at the point where the main shock hit unevenly. Since the eastern side of the shock encounters the interface first, this region of the explosion develops its "phase three" R-T plumes the quickest, which can be seen explicitly as the two white instabilities in the northeastern quadrant in Figure 3.19(e) at a radius of $\sim 9.0 \times 10^6$ km. Additional fragmentation occurs later, forming singular, but dominant, R-T instabilities in succession. In our higher resolution 2D tests, we find the development of R-T instabilities to be much more abundant and the fragmentation to be much more uniform.

The deceleration of the shock front allows the trailing phase two and phase one material (the carbon bubble and R-T plumes within this bubble, respectively) to eventually get injected into the rear of the fragmenting He/H shell. The carbon bubble achieves this first, as a portion of it first reaches the fragmenting He/H shell and its reverse shock at 3000 s. By 10000 s (Figure 3.19(f)), some of the He/H R-T plumes have penetrated the rear of the shock front, and the second reverse shock continues to propagate inward in mass, which allows the remaining regions of the phase two carbon bubble to catch up to it. (The dark blue bubble in Figure 3.19(f) catches up to the white.) Note that the two metal-rich phase one R-T plumes in the northeast have at this point merged and burrowed through both the carbon bubble and the second reverse shock (see red R-T plume at ∼40° in Figure 3.19(f)). At 30000 s, the remaining phase one R-T instabilities reach and interact with this shell as well. (The 80° and 130° R-T plumes reach the front edges of the dark blue and white at $\sim 10^8$ km in Figure 3.19(g).) Additionally, the fragmenting shell, which was once only composed of helium and hydrogen, is now enriched in the phase two carbon. (The blue bubble now occupies the inner anatomy of the previously white R-T plumes in Figure 3.19(g).)

Phase four is the simplest of all our phases, as most features within the explosion are solely expanding radially. At about 40000 s, the shock crosses a sudden density spike in the middle of the H shell (ρr^3 spike at $\sim$1.5 $\times$ 10^8 km in Figure 3.20). This does not produce a third reverse shock, but it does spawn a noticeable pressure wave that starts propagating inward in mass (and eventually in radius), as the shock experiences a jolt seen as fluctuations in its velocity starting at this point (see $v_{\rm Shock}$, solid lines, in Figure 3.20). Although some of the He/H R-T plumes penetrated the rear of the main shock earlier, they have lost momentum trying to dig their way through the shock and are now being outpaced by it. By 60000 s, this model has partial shock breakout at the poles and the shock exits the grid along the pole. As these polar flows are artifacts of the assumed symmetry in CHIMERA, we continue the simulation to determine when the remainder of the shock front would achieve shock breakout. From this point forward, we provide analysis on the wedge of data that exclude the polar regions. (The wedge considers polar angles $30^\circ \leq \theta \leq 150^\circ$ across all ϕ.)

The second reverse shock further collapses the phase two carbon bubble, and the stems of the phase one R-T plumes within it, as it starts to progress inward in radius at $\sim$70000 s. This continues until full shock breakout is achieved when the (non-pole) shock leaves the grid (3.57×10^8 km) at $\sim$140000 s (38.8 hours). We rewind the end of our simulation to $\sim$110000 s, when the aforementioned "wedge" of the shock enters the region of the progenitor that is partially ionized. By this time, the majority of trailing R-T bullets are at $\sim$2.0 $\times$ 10^8 km, approximately 12 hours behind the shock front.

The D10–2D3D model keeps its toroidal shape through its entire evolution, like the D9.6–2D3D model. The average velocity of the metal-rich clumps is significantly lower than the average velocity of the shock (see consistent gap between the green curves in Figure 3.20). The velocity gap between the two increases when the shock front starts to accelerate down the density gradient as it approaches the He/H interface, which enlarges the relative velocity gap to a difference of $\sim$7000 km s^{-1}. Although this does not allow for any interaction with the main shock, it does allow for the main R-T clumps to grow rather elongated before encountering the He/H mass shell and reverse shock.

Burrowing through the He/H mass shell is what establishes the final morphology of the CCSN, as this greatly shapes the ejecta and has the ability to spawn further R-T plumes.

However, the fragmentation of this shell is quite minimal, and the perturbation from the trailing R-T clumps only seems to add to its bulk at the point of collision. Although some R-T plumes are seeded from this event, the development of the extended structures echos only the previously trailing asymmetries, rather than having a fully fragmented shell across all angles. Figure 3.21 shows how different the environment is between D10–2D3D and a high-resolution D10–2D2D model. The D10–2D3D model has three main He/H R-T features forming out of the fragmenting shell as the trailing instabilities catch up to it, while the high resolution D10–2D2D simulation has numerous R-T plumes developing at the equivalent time.

Naturally, the greater number of R-T plumes is not surprising given a much higher resolution, but we provide it here as an example of how the morphology can evolve much differently if the trailing R-T plumes encounter a fragmenting shell equivalent to that of the D10–2D2D high resolution model. While the bullets in the high resolution D10–2D2D model still have a fingerprint of the clumps that collided with the second reverse shock, there is a much more complex angular distribution of ejecta with much more mixing close to the rear of the shock front. This complex environment does not occur in the D10–2D3D model (or in D10–2D3D$_{\text{Tilted}}$ as we will discuss in Section 3.2.2), which shows a morphological environment that echoes the asymmetries of the past. The D10–2D3D model is eerily similar to its D10–2D2D counterpart of the same resolution (compare center to left panel of Figure 3.21). As was apparent with the D9.6–2D3D model, a basic 2D3D mapping does not provide much benefit over running a 2D simulation with similar resolution, due to the absence of longitudinal velocities.

3.2.2 D10-2D3D-Tilted

The D10–2D3D model does not seem to accurately portray the long-term evolution of a strongly axisymmetric explosion, due to the lack of initial longitudinal velocities and exaggerated polar flows from an unfortunate interaction between the 2D CHIMERA model's polar flow and the excised cone in FLASH. The D10–2D3D$_{\text{Tilted}}$ model alleviates the interaction with the excised cone, though the polar flow itself is still present as it has been tilted fully onto the FLASH grid.

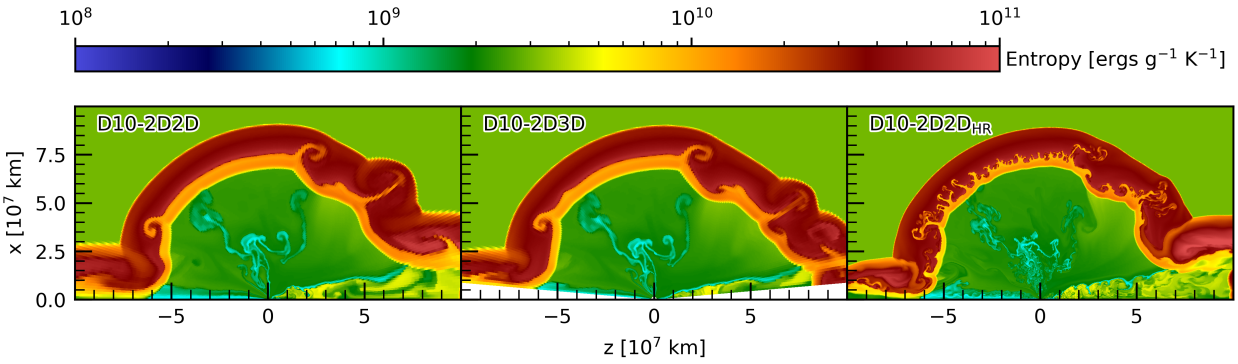

Figure 3.21: Entropy slice of the D10–2D3D model (center) compared to 2D simulations of similar resolution (left) and higher resolution (right) at 17500 s.

At first glance, the first column of the yields in Figure 3.22 do not show much change in the ejecta distribution in velocity space between D10–2D3D and D10–2D3D$_{\text{Tilted}}$. The dominance of the poles in both models drowns out contributions from the rest of the ejecta to the higher velocity matter and hides the microstructure in the first column of Figure 3.22. Because the poles in the D10 model are so dramatic, this provides a counterexample to the argument that the yields distribution in the D9.6–2D3D$_{\text{Tilted}}$ model could potentially be misleading due to more of the polar flow being present on the grid compared to its respective D9.6–2D3D model. If that were the case, then we would see a more dramatic difference in the distribution of the ejecta when comparing the upper and lower panels of the first column in Figure 3.22. Clearly, we do not.

To reveal microstructure obscured by the poles, we further analyze the yields by considering a wedge of the models that excludes contributions on the grid from the polar flows (second, third columns of Figure 3.22). The wedge for D10–2D3D$_{\text{Tilted}}$ is the same wedge discussed in Section 3.2.1 for the D10–2D3D model ($30° \leq \theta \leq 150°$ across all ϕ), but is applied after a 90° coordinate transform (i.e. after "undoing" the tilt). Through this, we actually see more of an effect that tilting the model has provided, as D10–2D3D$_{\text{Tilted}}$ has an apparent higher velocity tail ($\sim$2500 km s^{-1}) compared to its D10–2D3D counterpart ($\sim$1900 km s^{-1}) when comparing models in the second column of Figure 3.22. Comparing models in mass space (third column of Figure 3.22) shows higher yields for D10–2D3D$_{\text{Tilted}}$ in the outer regions. This can clearly be seen in the extent of ^{56}Ni and ^{44}Ti, which both drop significantly in the D10–2D3D model at 7.5 $M_{\odot}$ (top row, third column of Figure 3.22). In contrast, for the D10–2D3D$_{\text{Tilted}}$ model both ^{56}Ni and ^{44}Ti extend to 8.5 $M_{\odot}$, joining the lighter elements in the ejecta (bottom row, third column of Figure 3.22). The total yields (Table 3.2) further reveal this difference, with roughly 6% and 13% greater ^{44}Ti and ^{56}Ni yields, respectively, in the D10–2D3D$_{\text{Tilted}}$ model. Due to more of the polar flows, which originate from the hot bubble, being included on the grid, these isotopes (plus ^{52}Fe) are some of the key differences relative to the D10–2D3D model, while the rest of the yields are relatively consistent between D10 models. Although the poles are excised for both models in Table 3.2, the relevant species are more heavily mixed into surrounding areas during

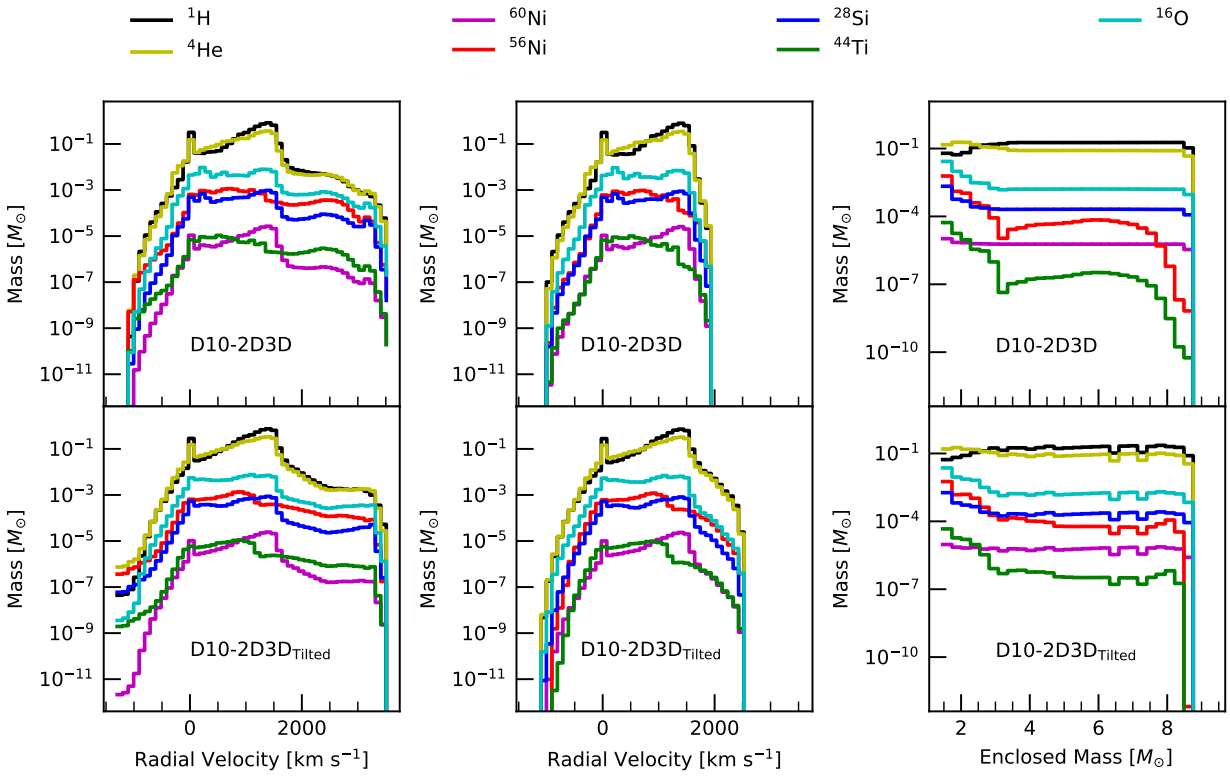

Figure 3.22: Mass yields of key isotopes binned across radial velocity (left, center columns – 50 bins) and enclosed mass (right column – 30 bins) for each D10 model. Note that each bin is consistent across all models for each column, and that both the center and right columns exclude the polar flows via considering a wedge of the data defined in Sections 3.2.1 and 3.2.2.

Table 3.2: Total D10 Yields At Shock Breakout

Species	2D3D $[M_\odot]$	$2D3D_{\text{Tilted}}$ $[M_\odot]$
^{1}H	4.131	4.277
^{4}He	2.488	2.533
^{12}C	4.546×10^{-2}	4.580×10^{-2}
^{16}O	7.985×10^{-2}	8.076×10^{-2}
^{28}Si	7.842×10^{-3}	7.948×10^{-3}
^{44}Ti	8.952×10^{-5}	9.481×10^{-5}
^{48}Ca	1.132×10^{-6}	1.164×10^{-6}
^{52}Fe	2.146×10^{-4}	2.207×10^{-4}
^{56}Ni	9.860×10^{-3}	1.115×10^{-2}
^{60}Ni	1.571×10^{-4}	1.616×10^{-4}
^{66}Zn	6.482×10^{-6}	6.572×10^{-6}
Iron Group_{NR}	1.068×10^{-2}	1.101×10^{-2}

Note. — These yields exclude contributions from the polar flows. Iron Group_{NR} is defined as all species in our network falling in the range of ^{49}Cr–^{64}Ni, while excluding ^{52}Fe and ^{56}Ni. Only cells with a positive radial velocity are considered. This table, with all 160 species, is located in Appendix B. The species listed above are a selection of the content presented for analysis.

the explosion in the D10–2D3D$_{\text{Tilted}}$ model, thus these species are more abundant than for D10–2D3D.

The consistency of the ejecta for the two D10 models is matched by the consistency in shock progression (colored, solid curves in Figures 3.23). Even the average radii of the $X_{^{56}\text{Ni+IG}}$ isosurfaces (colored, dashed curves) are quite similar. Despite this, the D10–2D3D$_{\text{Tilted}}$ model develops more spherical-bubble structures during its evolution (Figure 3.24, right), due to the initial longitudinal and latitudinal velocities. This is consistent with what happened in the D9.6–2D3D$_{\text{Tilted}}$ model. D10–2D3D$_{\text{Tilted}}$ is slightly less axisymmetric than D10–2D3D in Figure 3.24 and has more structure in its central and outer regions. Therefore, these metal-rich clumps in the D10–2D3D$_{\text{Tilted}}$ model retain slightly higher velocities (dashed orange curve in Figure 3.20) over its D10–2D3D counterpart (dashed green curve in Figure 3.20) until the He/H interface when the shock starts to decelerate and the second reverse shock forms. The second reverse shock dictates the subsequent velocity profile of the clumps, limiting their velocities as they try to burrow through it, bringing the average clump velocities back together as both dashed curves decrease until shock breakout. Although the *average* velocities of the clumps for both models obtain similar values near shock breakout, the *overall* velocity distribution across the analysis wedge domain (Figure 3.25) shows that the D10–2D3D$_{\text{Tilted}}$ model still retains higher velocities in the outer envelope.

The dynamics of the small features are further demonstrated by the growth in the isosurface areas (Figure 3.26). The total area for both the external coating (0.1% isosurface) and inner anatomy (3% isosurface) of the ^{56}Ni+IG-rich plumes start to diverge early during the dramatic acceleration of the shock. After encountering the reverse shock at ∼10000 s, the total surface area represented by the external coating (0.1% isosurface) of the bullets diverges further, as the bullets in D10–2D3D$_{\text{Tilted}}$ are able to burrow through it more efficiently due to the somewhat higher velocities that result from the spherical-like structures created upon the deviation from axisymmetry. The second divergence between models is not present in the 3% isosurface (inner anatomy) curves. This is not surprising due to the relatively similar distribution of metal-rich ejecta in both simulations, with the key differences occurring at larger mass coordinates and higher velocities that are inherently captured by the external

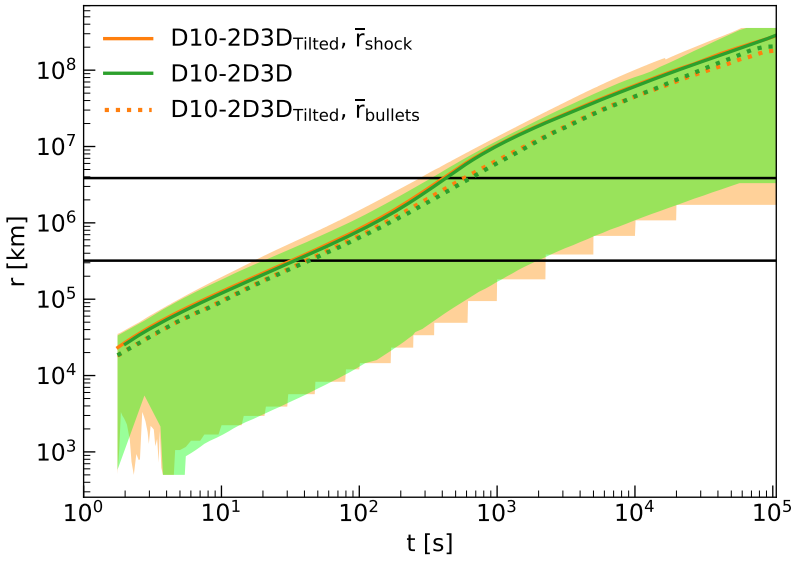

Figure 3.23: Angle-averaged shock radius (colored, solid lines) and angle-averaged bullet radius of the $X_{^{56}\text{Ni+IG}} = 3\%$ isosurface (colored, dashed lines) as functions of time for the D10 models. Matching overlaid colored regions highlight the range of r_{min} to r_{max} of a model's respective bullet isosurface. The horizontal black lines mark the radii of the He burning shell to inert He layer transition (bottom line) and He/H composition interface (top line).

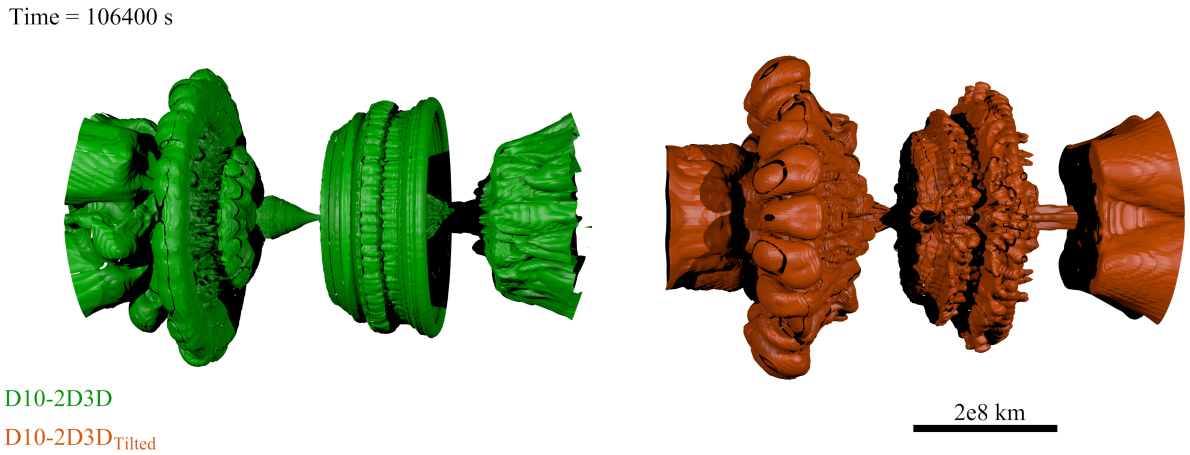

Figure 3.24: External coating $X_{^{56}\text{Ni+IG}} = 0.1\%$ isosurface for the D10–2D3D (green, left) and D10–2D3D$_{\text{Tilted}}$ (orange, right) bullets at shock breakout. Note, the D10–2D3D$_{\text{Tilted}}$ isosurface has been realigned in post-processing (i.e. rotated clockwise about its y-axis 90°) to match the orientation of the other model. The open ended "caps" are due to the poles evolving off the grid much earlier in the simulation.

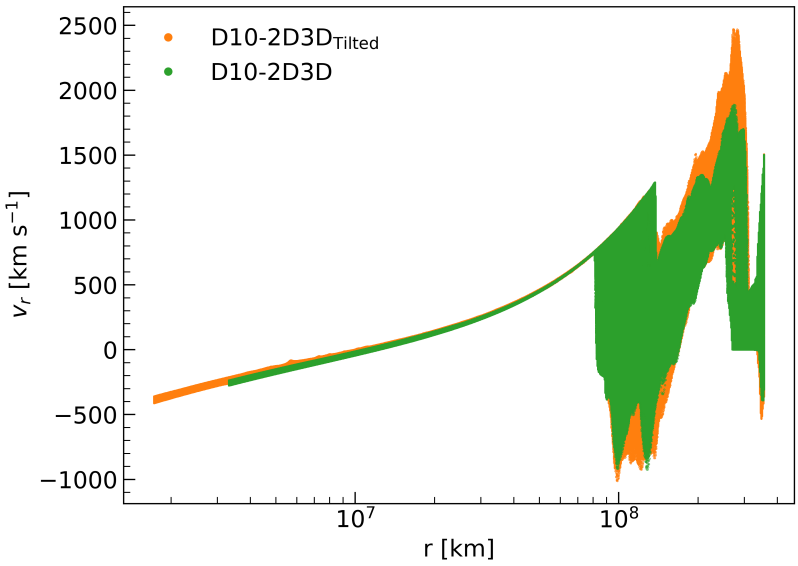

Figure 3.25: Scatter points of a grid cell's radial velocity versus cell-centered radius at shock breakout for each D10 model. Note, cells in the polar flows have been excluded via considering a wedge of the data.

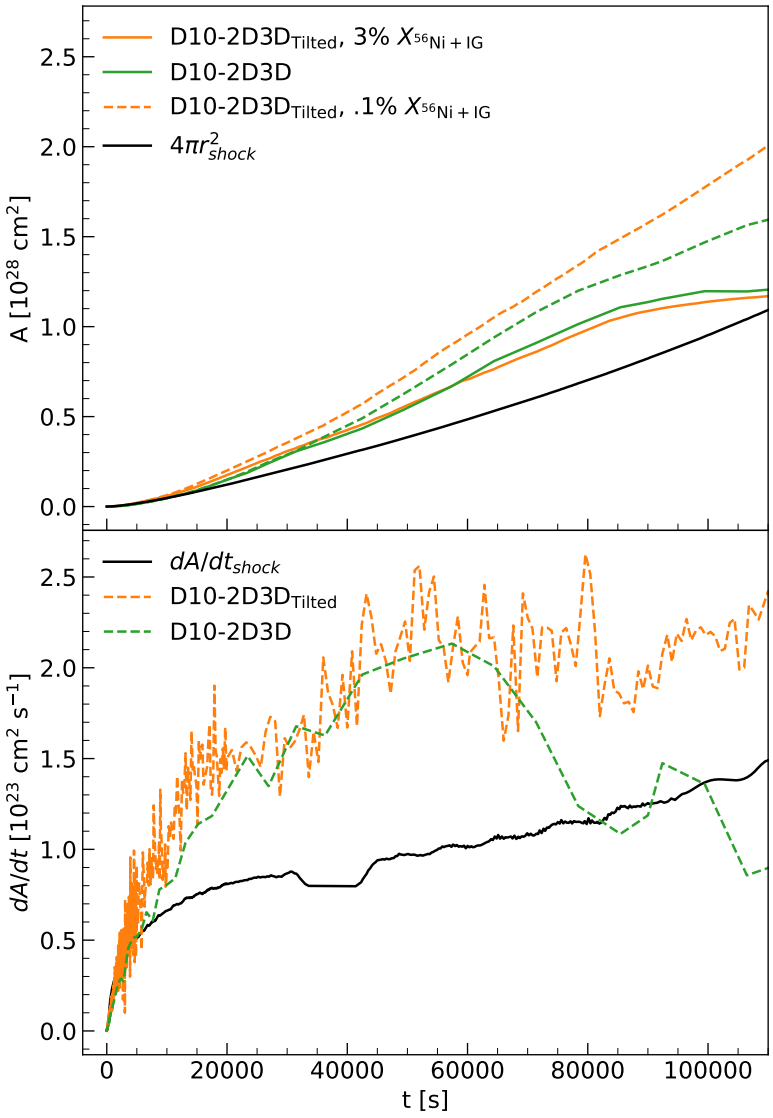

Figure 3.26: Top: Surface area of the $X_{^{56}\text{Ni+IG}} = 3\%$ (colored, solid) and $X_{^{56}\text{Ni+IG}} = 0.1\%$ (colored, dashed) isosurfaces for each D10 model. The average shock radii over time across all models are nearly identical, thus only the surface area of the D10–2D3D shock (black, solid) is included. Bottom: Numerical time derivatives of the surface area for the shock (black, solid) and $X_{^{56}\text{Ni+IG}} = 0.1\%$ (colored, dashed) curves of the top plot. Note that the difference in file output in the D10–2D3D simulation has led to a less dense distribution of data points.

coating isosurface instead. As with D9.6, the contributions to the total surface area converge back toward those provided by the expansion of the shock and more dramatically for D10–2D3D, which stays more axisymmetric and lacks the spherical-bubble structures that retain higher velocities and prolong the convergence to the shock-driven area increase. In contrast to the D9.6 models, the 0.1% isosurface in the D10 models has a larger total surface area than the 3% isosurface due to the considerable amount of fallback caused by the reverse shocks combined with a more condensed angular distribution of the metal-rich ejecta due to fewer R-T plumes spanning the whole volume.

The D10–2D3D$_{\text{Tilted}}$ model achieves greater velocities compared to D10–2D3D, although not as striking as D9.6–2D3D$_{\text{Tilted}}$. We believe that this is less dramatic in this simulation due to the resolution-limited spawning of only a few clumps at the He/H fragmentation, whereas D9.6 has a wider range of bullets developing from its (C+O)/He fragmentation. We would expect a larger deviation from the D10–2D3D toroid shape if the fragmentation environment was more similar to the high resolution test of Figure 3.21. Most importantly, despite all this, the end result of the D10–2D3D$_{\text{Tilted}}$ model no longer looks like a rotated 2D model and provides a more faithful 3D model of a polar-dominated explosion than the un-tilted D10–2D3D model.

Chapter 4

Conclusions

We have computed simulations of core-collapse supernovae using the FLASH code from the end of the neutrino-driven phase until shock breakout using two stellar progenitors with different structures, a 9.6 $M_\odot$ zero-metallicity red supergiant and a 10 $M_\odot$ solar-metallicity red supergiant. We have performed these simulations using 160 nuclear species — the largest network ever used in this regime — and higher resolution than comparative studies to provide a more faithful rendering of the composition, development, and terminal distribution of Rayleigh-Taylor (R-T) plumes.

The fully-consistent 3D model, D9.6–3D3D, starts to develop its initial R-T plumes by 2 s, after the shock fully crosses into the He layer. Large-scale features start to form at ∼60 s after the fastest moving R-T bullets penetrate the shock. As the shock continues to progress through the He core, the R-T bullets grow significantly into large mushroom features at ∼150 s. At ∼1000 s, the shock crosses the He/H composition interface and creates a weak pressure wave that propagates inward in mass and radius before steepening into a reverse shock. The minimal change in ρr^3 delays the formation of this reverse shock, which ensures that the fastest (and closest) R-T bullets interact with the rear of the main shock before the reverse shock forms. This interaction not only seeds new instabilities, but it further develops the most dominant R-T fingers into even larger mushroom-shaped plumes that are able to penetrate and re-shape the shock front. What once were primarily metal-rich mushrooms are now heavily coated in helium, for the propagation through the He core has filled the gaps between the R-T fingers. However, the original inner regions of the ejecta still form

the "bulk" of the inner anatomy of a single finger. Most notably represented in the main anatomy of an instability are the Ni isotopes, with the most abundant isotope occupying the bullets being ^{60}Ni. As the shock continues to expand, the inner regions of the explosion are shredded by the reverse shocks formed at the (C+O)/He and He/H interfaces. The shock continues to propagate through the H envelope until hitting the edge of the star at ∼70000 s (19.4 hours). We "rewind" and declare the end of our simulations at ∼62000 s, as this is the time where the shock enters the region of the progenitor where the Helmholtz equation of state assumption of fully-ionized hydrogen is no longer valid.

The extended structures developed out of the He/H interface in the D9.6–3D3D model are fingerprints of the early asymmetries present in the CHIMERA model. This agrees with the general findings of Wongwathanarat et al. [102] regarding their analysis of morphology development of different progenitors. The density profile of this star allows for steady deceleration of the shock through the He shell, which keeps the leading R-T bullets close to the rear of the shock. Consequently, the He/H mass shell has great impact on the trailing ejecta after the shock front has collided with the interface, with the ability to trap the bulk of the metal-rich ejecta if the R-T bullets are moving too slow relative to the shock. Because the relative velocity gap between v_{Shock} and v_{bullets} is small enough in D9.6–3D3D, the leading R-T bullets (those representing the greatest early-time asymmetries) are not trapped behind the wall of ^{4}He, reaching velocities of ∼1750 km s^{-1}.

Our 2D3D D9.6 simulations show that in the absence of a fully-consistent 3D model, tilting the axis of an axisymmetric 2D model in 3D produces a final morphology which better resembles a fully 3D model. The rotation of the coordinates breaks the symmetry of the non-radial velocities such that the initially toroidal structure of the 2D-to-3D model develops spherical-bubble structures along its originally axisymmetric toroids (D9.6–2D3D$_{\mathrm{Tilted}}$), which does not occur when the 3D grid remains aligned to the original 2D symmetry axis (D9.6–2D3D). These bubbles retain higher velocities and more easily spawn further R-T plumes at key density interfaces, which directly affects the final morphology of the ejecta. The D9.6–2D3D$_{\mathrm{Tilted}}$ model develops extended structures beyond the He/H interface, and also maintains maximum velocities of the metal-rich clumps similar to D9.6–3D3D. This enables further mixing of metal-rich ejecta into the outer regions of the H

envelope, thus providing similar ejecta distribution in both mass and velocity spaces, with the bullets reaching ∼1950 km s^{-1} at shock breakout. Clearly, the D9.6–2D3D$_{\text{Tilted}}$ model shows that axisymmetry is able to be broken with minimal perturbations. Because of the lack of spherical-bubble structures, the leading bullets in the D9.6–2D3D model move slow enough to get trapped behind the He/H wall (limiting velocities to ∼1250 km s^{-1} at shock breakout), thus this model does not share the morphological development of the D9.6–3D3D model. Therefore, the un-tilted D9.6–2D3D model looks primarily like a 2D model that has been extended to 3D space in axisymmetry — even at shock breakout.

A similar trapping event occurs in the studies of Stockinger et al. [84] for the same progenitor, as their model does not develop distinct elongated structures beyond the He wall, even though it is a fully 3D model. The morphological contrast is most clearly seen by comparing Figure 20 in Stockinger et al. [84] with our Figure 3.4. The result is a distribution of ejecta in both mass and velocity spaces that looks much more like the distribution seen in our effectively 2D D9.6–2D3D model. We believe this divergence in behavior for similar codes modeling the same progenitor is due to the explosion in the VERTEX-PROMETHEUS model being much less powerful than that in the CHIMERA model, as the diagnostic explosion energy of our input explosion model is 95% larger. The lower explosion energy of the VERTEX-PROMETHEUS model does not allow the Ni bullets to retain sufficient velocities to keep up with the shock, leading to the 250% difference we see at shock breakout between our maximum ^{56}Ni velocities and theirs. This, in combination with our angular resolution being twice as high, leads to different R-T fragmentation developing from the density interfaces.

Unlike the D9.6 simulations that have essentially two phases to shock progression (pre- and post-He/H interface), the D10 progenitor's density profile gives rise to four distinct phases of evolution. Starting with phase one, the shock is still briefly accelerating after crossing the (C+O)/He interface, which creates a large reverse shock from the subsequent deceleration once fully into the He-burning shell. As the (C+O)/He shell fragments, four main R-T plumes are quickly spawned, which are reminiscent of the dominant plumes that caused the shock to hit the composition interface. By 30 s, the shock reaches the density interface at the transition from the He-burning shell to the rest of the He layer, which marks the beginning of phase two. Due to the dramatic change in ρr^3 in this shell, the

shock accelerates significantly until it reaches the hydrogen envelope, which creates a large separation between the shock front and the trailing R-T fingers. By 60 s, the four main R-T fingers stretch with extremely thin stems at the base while the reverse shock collapses the material behind them. Phase three begins at ∼400 s, when the main shock encounters the He/H interface and launches an additional strong reverse shock due to the significant deceleration upon crossing the interface. The deceleration of the shock front allows the trailing material (the four main R-T plumes from the previous phases) to eventually get injected into the rear of the fragmenting He/H shell. As the shock front significantly outpaced the inner ejecta during phase two, the aforementioned injection does not occur until hours later at ∼10000 s. During phase four (from ∼30000 s onward), the shock front slowly expands to shock breakout. By 60000 s, this model has partial shock breakout at the poles and the shock exits the grid along the pole. As these polar flows are artifacts of the assumed symmetry in CHIMERA, we continued the simulation to determine when the remaining portions of the shock front (the "physical" shock) would achieve shock breakout, which occurs at ∼140000 s (38.8 hours). Similar to the D9.6 models, we rewind the end of our simulation to ∼110000 s, when the physical shock enters the region of the progenitor that is partially ionized.

We applied the same tilting comparison to the D10 progenitor, as we did not have a corresponding 3D CHIMERA model that has achieved a successful explosion. We acknowledge that tilting, because of the cutout along the polar axis in the FLASH model, does include more of the polar flow onto the grid, yet emphasize this is extremely dependent on the initial conditions of the 2D model, as the polar flows are particularly strong in the D10 models (as opposed to the D9.6 where polar flows in all models are comparable to flows at other latitudes). In mass and velocity spaces, we see relatively consistent distributions in both models, but we still see higher velocities and more outward radial mixing in the D10–2D3D$_{\rm Tilted}$ model (∼2500 km s^{-1}) when compared to D10–2D3D (∼1900 km s^{-1}). The parameterized 18 $M_\odot$ and 19.8 $M_\odot$ red supergiant models of Ono et al. [71], which have density profiles past the (C+O)/He interface that are similar to our D10 progenitor, achieve even higher velocities (∼5000 km s^{-1}), but this is due to a significantly larger explosion energy in their models (∼1.8×10^{51} ergs compared to ∼3.1×10^{50} ergs in our model). Although

D10–2D3D$_{\text{Tilted}}$ did not have as extreme an effect on the distribution of ejecta as was seen in the D9.6 model, tilting seems to have few drawbacks and significant benefits by breaking the toroidal symmetry and restoring a more natural structure to the final distribution of ejecta.

As with the D9.6 models, the D10–2D3D and D10–2D3D$_{\text{Tilted}}$ models are also consistent with the morphology analysis of Wongwathanarat et al. [102]. The type of morphology seen in the D10 simulations, a few extremely elongated R-T fingers, is due to the strongly varying density profile the shock encounters during its progression. The strong acceleration of the shock before encountering the He/H interface creates a large separation between the shock front and metal-rich clumps, thus allowing those metal-rich R-T plumes to grow quite elongated before catching up to the reverse shock created from the subsequent deceleration of the main shock. Examining the D9.6 and D10 models, we stress the importance of the density structure on the evolution of the explosion, as widely different results occur depending on the shock progression through the stellar density interfaces. However, as we discussed earlier in this section, the contrast between the Stockinger et al. [84] z9.6 model and our D9.6–3D3D model highlights the ability of the strongly aspherical initial explosion launched by the central engine to mediate the influence of the progenitor structure.

We believe the minimal impact of tilting on D10 is due to the strong polar flow and nature of the density profile in this progenitor. The more complex system of D9.6–2D3D$_{\text{Tilted}}$, with more R-T plumes across all latitudes, is more strongly affected by the tilting. In contrast, a simulation with few dominant R-T plumes does not provide enough dynamics between the longitudinal and latitudinal velocities to drive a clear deviation from axisymmetry (D10–2D3D$_{\text{Tilted}}$). Nevertheless, from a morphological standpoint, the D10–2D3D$_{\text{Tilted}}$ model *still* appears more realistic than D10–2D3D. The fact that the sole difference between the 2D3D and 2D3D$_{\text{Tilted}}$ models is that the initial conditions are rotated 90°, and that this causes an originally axisymmetric model to behave more like a 3D model, is a fascinating discovery. Although this seems to be progenitor and potentially resolution dependent, this gives much more value to a pure 2D model than previously believed. Because of the minimal drawbacks to extending a 2D model like this in 3D, we recommend this approach if one does not have a true 3D model available.

Analyzing the distribution of ejecta for both of these progenitors shines light on the importance of using a realistic nuclear network. That the total mass yields of our neutron-rich material rivals ^{56}Ni — and in some cases exceeds it — shows the importance of tracking a realistic number of species throughout the entire explosion, not just during the neutrino heating phase. This is highlighted by the extent of radial mixing we see of this neutron-rich material into the outer envelope (extending to the surface in both progenitors). In our D9.6 simulations, we also see a higher abundance of ^{60}Ni than ^{56}Ni in high-velocity regions, $v \gtrsim 1750$ km s^{-1}. Although others, such as Stockinger et al. [84], tried tracking neutron-rich material with a tracer nucleus, our results strongly imply that a tracer nucleus does not fully capture the yields or distribution of neutron-rich material at shock breakout, as demonstrated by our yields being an order of magnitude larger and extending significantly passed the $\sim$2 $M_\odot$ and $\sim$500 km s^{-1} maximum extents seen in Stockinger et al. [84]. Of course, the largest difference between z9.6 of Stockinger et al. [84] and our D9.6–3D3D simulation are the results of the respective VERTEX-PROMETHEUS and CHIMERA runs. The larger explosion energy and larger quantity of heavy element ejecta limits our ability to compare the results of the tracer nucleus approach to our realistic nuclear set. But these differences also act as a reminder that although these extended simulations further develop the final *distribution* of the ejecta, the *amount* of ejecta seen at shock breakout — and the final fate of the supernova — is determined by the explosion at early epochs.

The future development of this research depends on the availability of 3D models from CHIMERA. More 3D models means more data to compare against observations, especially with more conventionally aspherical models – as opposed to the D9.6 model, which had a relatively spherical shock front throughout its evolution. However, to truly compare with observations, our completed FLASH models must be ran fully through the surface of the star and into the circumstellar medium. Our data can then be mapped to a light-curve generating code and evolved further, similar to the work seen in Utrobin et al. [94]. Additionally, as discussed in Section 3.1.5, more particle analysis must be done to further analyze the fate of ejecta. And perhaps most importantly, as the computational power of the world increases, so does our ability to run higher quality core-collapse supernova simulations, which will further enlighten the ruby sanctum of our mind about the mysteries of this explosive event.

Bibliography

[1] Argast, D., Samland, M., Thielemann, F.-K., and Qian, Y.-Z. (2004). Neutron star mergers versus core-collapse supernovae as dominant r-process sites in the early Galaxy. *A&A*, 416:997–1011. 3

[2] Arnett, W. D., Bahcall, J. N., Kirshner, R. P., and Woosley, S. E. (1989). Supernova 1987A. *ARA&A*, 27:629–700. 3

[3] Aschenbach, B., Egger, R., and Trümper, J. (1995). Discovery of explosion fragments outside the Vela supernova remnant shock-wave boundary. *Nature*, 373(6515):587–590. 4

[4] Bethe, H. A. and Wilson, J. R. (1985). Revival of a Stalled Supernova Shock By Neutrino Heating. *ApJ*, 295:14–23. 2, 5

[5] Bhalerao, J., Park, S., Schenck, A., Post, S., and Hughes, J. P. (2019). Detailed X-Ray Mapping of the Shocked Ejecta and Circumstellar Medium in the Galactic Core-collapse Supernova Remnant G292.0+1.8. *ApJ*, 872(1):31. 3

[6] Bodansky, D., Clayton, D. D., and Fowler, W. A. (1968). Nuclear Quasi-Equilibrium during Silicon Burning. *ApJS*, 16:299. 6

[7] Boggs, S. E., Harrison, F. A., Miyasaka, H., Grefenstette, B. W., Zoglauer, A., Fryer, C. L., Reynolds, S. P., Alexander, D. M., An, H., Barret, D., Christensen, F. E., Craig, W. W., Forster, K., Giommi, P., Hailey, C. J., Hornstrup, A., Kitaguchi, T., Koglin, J. E., Madsen, K. K., Mao, P. H., Mori, K., Perri, M., Pivovaroff, M. J., Puccetti, S., Rana, V., Stern, D., Westergaard, N. J., and Zhang, W. W. (2015). ^{44}Ti gamma-ray emission lines from SN1987A reveal an asymmetric explosion. *Science*, 348:670–671. 3

[8] Brown, E. F., Calder, A. C., Plewa, T., Ricker, P. M., Robinson, K., and Gallagher, J. B. (2005). Type Ia Supernovae: Simulations and Nucleosynthesis. *Nucl. Phys. A*, 758:451–454. 30, 31

[9] Bruenn, S. W. (1985). Stellar core collapse - Numerical model and infall epoch. *ApJS*, 58:771–841. 10

[10] Bruenn, S. W., Blondin, J. M., Hix, W. R., Lentz, E. J., Messer, O. E. B., Mezzacappa, A., Endeve, E., Harris, J. A., Marronetti, P., Budiardja, R. D., Chertkow, M. A., and Lee, C.-T. (2020). Chimera: A Massively Parallel Code for Core-collapse Supernova Simulations. *ApJS*, 248:11. 11

[11] Bruenn, S. W., De Nisco, K. R., and Mezzacappa, A. (2001). General Relativistic Effects in the Core Collapse Supernova Mechanism. *ApJ*, 560:326–338. 10

[12] Bruenn, S. W., Dirk, C. J., Mezzacappa, A., Hayes, J. C., Blondin, J. M., Hix, W. R., and Messer, O. E. B. (2006). Modeling Core Collapse Supernovae in 2 and 3 dimensions with spectral neutrino transport. *J. Phys.: Conf. Ser.*, 46:393–402. 11

[13] Burrows, A., Hayes, J., and Fryxell, B. A. (1995). On the Nature of Core Collapse Supernovae Explosions. *ApJ*, 450:830–850. 4

[14] Burrows, A. and Lattimer, J. M. (1985). The prompt mechanism of Type II supernovae. *ApJ*, 299:L19–L22. 2

[15] Calder, A. C., Fryxell, B., Plewa, T., Rosner, R., Dursi, L. J., Weirs, V. G., Dupont, T., Robey, H. F., Kane, J. O., Remington, B. A., and et al. (2002). On validating an astrophysical simulation code. *The Astrophysical Journal Supplement Series*, 143(1):201–229. 30

[16] Cayrel, R., Depagne, E., Spite, M., Hill, V., Spite, F., François, P., Plez, B., Beers, T., Primas, F., Andersen, J., Barbuy, B., Bonifacio, P., Molaro, P., and Nordström, B. (2004). First stars V - Abundance patterns from C to Zn and supernova yields in the early Galaxy. *A&A*, 416:1117–1138. 11

[17] Chandrasekhar, S. (1939). The internal constitution of the stars. *Proceedings of the American Philosophical Society*, 81:153–187. 2

[18] Chevalier, R. A. (1976). The hydrodynamics of type II supernovae. *ApJ*, 207:872–887. 7

[19] Cioffi, D. F., McKee, C. F., and Bertschinger, E. (1988). Dynamics of Radiative Supernova Remnants. *ApJ*, 334:252. 45

[20] Couch, S. M., Graziani, C., and Flocke, N. (2013). AN IMPROVED MULTIPOLE APPROXIMATION FOR SELF-GRAVITY AND ITS IMPORTANCE FOR CORE-COLLAPSE SUPERNOVA SIMULATIONS. *The Astrophysical Journal*, 778(2):181. 18

[21] Couch, S. M., Wheeler, J. C., and Milosavljević, M. (2009). Aspherical Core-Collapse Supernovae in Red Supergiants Powered by Nonrelativistic Jets. *ApJ*, 696:953–970. 16

[22] Courant, R., Friedrichs, K., and Lewy, H. (1928). Über die partiellen Differenzengleichungen der mathematischen Physik. *Mathematische Annalen*, 100:32–74. 18

[23] Dimonte, G., Youngs, D. L., Dimits, A., Weber, S., Marinak, M., Wunsch, S., Garasi, C., Robinson, A., Andrews, M. J., Ramaprabhu, P., Calder, A. C., Fryxell, B., Biello, J., Dursi, L., MacNeice, P., Olson, K., Ricker, P., Rosner, R., Timmes, F., Tufo, H., Young, Y.-N., and Zingale, M. (2004). A comparative study of the turbulent rayleigh–taylor instability using high-resolution three-dimensional numerical simulations: The alpha-group collaboration. *Physics of Fluids*, 16(5):1668–1693. 16

[24] Dubey, A., Antypas, K., Ganapathy, M. K., Reid, L. B., Riley, K., Sheeler, D., Siegel, A., and Weide, K. (2009). Extensible component-based architecture for flash, a massively parallel, multiphysics simulation code. *Parallel Computing*, 35(10):512 – 522. 16

[25] Duffell, P. C. (2016). A ONE-DIMENSIONAL MODEL FOR RAYLEIGH–TAYLOR INSTABILITY IN SUPERNOVA REMNANTS. *The Astrophysical Journal*, 821(2):76. 13

[26] Ellinger, C., Young, P., and Fryer, C. L. (2008). Nucleosynthetic Constraints on the Progenitor of Cassiopeia A. In [78], page 206. 14

[27] Fassia, A. and Meikle, W. P. S. (1999). ^{56}Ni dredge-up in Supernova 1987A. *MNRAS*, 302:314–320. 4

[28] Fernández, R. (2012). Hydrodynamics of Core-collapse Supernovae at the Transition to Explosion. I. Spherical Symmetry. *ApJ*, 749(2):142. 18, 19

[29] Fisher, R. T., Kadanoff, L. P., Lamb, D. Q., Dubey, A., Plewa, T., Calder, A., Cattaneo, F., Constantin, P., Foster, I., Papka, M. E., Abarzhi, S. I., Asida, S. M., Rich, P. M., Glendenin, C. C., Antypas, K., Sheeler, D. J., Reid, L. B., Gallagher, B., and Needham, S. G. (2008). Terascale turbulence computation using the flash3 application framework on the ibm blue gene/l system. *IBM Journal of Research and Development*, 52(1.2):127–136. 16

[30] Fraknoi, A., Morrison, D., and Wolff, S. C. (2016). *The Death of Stars*, chapter 23. OpenStax. 2

[31] Fröhlich, C., Hauser, P., Liebendörfer, M., Martínez-Pinedo, G., Thielemann, F.-K., Bravo, E., Zinner, N. T., Hix, W. R., Langanke, K., Mezzacappa, A., and Nomoto, K. (2006a). Composition of the Innermost Supernova Ejecta. *ApJ*, 637:415–426. 11

[32] Fröhlich, C., Martínez-Pinedo, G., Liebendörfer, M., Thielemann, F. K., Bravo, E., Hix, W. R., Langanke, K., and Zinner, N. T. (2006b). Neutrino-induced nucleosynthesis of A> 64 nuclei: The nu p-process. *Phys. Rev. Lett.*, 96(14):142502. 11

[33] Fryer, C., Young, P., Bennet, M. E., Diehl, S., Herwig, F., Hirschi, R., Hungerford, A., Pignatari, M., Magkotsios, G., Rockefeller, G., and Timmes, F. X. (2008). Nucleosynthesis from Supernovae as a Function of Explosion Energy from NuGrid. In [78], page 101. 10

[34] Fryxell, B., Mueller, E., and Arnett, D. (1991). Instabilities and Clumping in SN 1987A. I. Early Evolution in Two Dimensions. *ApJ*, 367:619. 7

[35] Fryxell, B., Olson, K., Ricker, P., Timmes, F. X., Zingale, M., Lamb, D. Q., MacNeice, P., Rosner, R., Truran, J. W., and Tufo, H. (2000). FLASH: An Adaptive Mesh Hydrodynamics Code for Modeling Astrophysical Thermonuclear Flashes. *ApJS*, 131:273–334. 16

[36] Gratton, R. G. and Sneden, C. (1991). Abundances of elements of the Fe-group in metal-poor stars. *A&A*, 241:501–525. 11

[37] Grefenstette, B. W., Fryer, C. L., Harrison, F. A., Boggs, S. E., DeLaney, T., Laming, J. M., Reynolds, S. P., Alexander, D. M., Barret, D., Christensen, F. E., Craig, W. W., Forster, K., Giommi, P., Hailey, C. J., Hornstrup, A., Kitaguchi, T., Koglin, J. E., Lopez, L., Mao, P. H., Madsen, K. K., Miyasaka, H., Mori, K., Perri, M., Pivovaroff, M. J., Puccetti, S., Rana, V., Stern, D., Westergaard, N. J., Wik, D. R., Zhang, W. W., and Zoglauer, A. (2017). The Distribution of Radioactive ^{44}Ti in Cassiopeia A. *ApJ*, 834:19. 3

[38] Grefenstette, B. W., Harrison, F. A., Boggs, S. E., Reynolds, S. P., Fryer, C. L., Madsen, K. K., Wik, D. R., Zoglauer, A., Ellinger, C. I., Alexander, D. M., An, H., Barret, D., Christensen, F. E., Craig, W. W., Forster, K., Giommi, P., Hailey, C. J., Hornstrup, A., Kaspi, V. M., Kitaguchi, T., Koglin, J. E., Mao, P. H., Miyasaka, H., Mori, K., Perri, M., Pivovaroff, M. J., Puccetti, S., Rana, V., Stern, D., Westergaard, N. J., and Zhang, W. W. (2014). Asymmetries in core-collapse supernovae from maps of radioactive ^{44}ti in cassiopeia a. *Nature*, 506:339–342. 3

[39] Hachisu, I., Matsuda, T., Nomoto, K., and Shigeyama, T. (1990). Nonlinear growth of Rayleigh-Taylor instabilities and mixing in SN 1987A. *ApJ*, 358:L57–LL61. 4, 7

[40] Hammer, N. J., Janka, H.-T., and Müller, E. (2010). Three-dimensional Simulations of Mixing Instabilities in Supernova Explosions. *ApJ*, 714:1371–1385. 12, 13, 14, 16, 20

[41] Hanuschik, R. W., Thimm, G., and Dachs, J. (1988). H-alpha fine-structure in SN 1987A within the first 111 days. *MNRAS*, 234:41P–49P. 4

[42] Harris, J. A., Hix, W. R., Chertkow, M. A., Lee, C.-T., Lentz, E. J., and Messer, O. E. B. (2017). Implications for Post-processing Nucleosynthesis of Core-collapse Supernova Models with Lagrangian Particles. *ApJ*, 843:2. 28

[43] Herant, M. and Benz, W. (1992). Postexplosion hydrodynamics of SN 1987A. *ApJ*, 387:294–308. 4, 7, 12

[44] Herant, M., Benz, W., Hix, W. R., Fryer, C. L., and Colgate, S. A. (1994). Inside the supernova: A powerful convective engine. *ApJ*, 435:339–361. 4, 10

[45] Hix, W. R. and Thielemann, F.-K. (1999). Silicon Burning II: Quasi-Equilibrium and Explosive Burning. *ApJ*, 511:862–875. 6, 28

[46] Hoffman, R. D., Woosley, S. E., Fuller, G. M., and Meyer, B. S. (1996). Production of the Light p-Process Nuclei in Neutrino-driven Winds. *ApJ*, 460:478–488. 10

[47] Hughes, J. P., Rakowski, C. E., Burrows, D. N., and Slane, P. O. (2000). Nucleosynthesis and Mixing in Cassiopeia A. *ApJ*, 528:L109–L113. 3

[48] Janka, H.-T. and Müller, E. (1996). Neutrino Heating, Coonvection, and the Mechanism of Type–II Supernova Explosions. *A&A*, 306:167–198. 4, 10

[49] Joggerst, C. C., Almgren, A., and Woosley, S. E. (2010). THREE-DIMENSIONAL SIMULATIONS OF RAYLEIGH-TAYLOR MIXING IN CORE-COLLAPSE SUPERNOVAE. *The Astrophysical Journal*, 723(1):353–363. 7

[50] Kageyama, A. and Sato, T. (2004). The yin-yang grid: An overset grid in spherical geometry. *Geochemistry Geophysics Geosystems*, 5. 20, 22, 23

[51] Kane, J., Arnett, D., Remington, B. A., Glendinning, S. G., Bazán, G., Müller, E., Fryxell, B. A., and Teyssier, R. (2000). Two-dimensional versus Three-dimensional Supernova Hydrodynamic Instability Growth. *ApJ*, 528:989–994. 7, 12

[52] Kifonidis, K., Plewa, T., Janka, H.-T., and Müller, E. (2000). Nucleosynthesis and Clump Formation in a Core-Collapse Supernova. *ApJ*, 531:L123–L126. 13

[53] Kifonidis, K., Plewa, T., Janka, H.-T., and Müller, E. (2003). Non-spherical core collapse supernovae. I. Neutrino-driven convection, Rayleigh-Taylor instabilities, and the formation and propagation of metal clumps. *A&A*, 408:621–649. 8, 9, 12, 54

[54] Kifonidis, K., Plewa, T., Scheck, L., Janka, H.-T., and Müller, E. (2006). Non-spherical core collapse supernovae. II. The late-time evolution of globally anisotropic neutrino-driven explosions and their implications for SN 1987 A. *A&A*, 453:661–678. 16

[55] Larsson, J., Fransson, C., Spyromilio, J., Leibundgut, B., Challis, P., Chevalier, R. A., France, K., Jerkstrand, A., Kirshner, R. P., Lundqvist, P., Matsuura, M., McCray, R.,

Smith, N., Sollerman, J., Garnavich, P., Heng, K., Lawrence, S., Mattila, S., Migotto, K., Sonneborn, G., Taddia, F., and Wheeler, J. C. (2016). Three-dimensional Distribution of Ejecta in Supernova 1987A at 10,000 Days. *ApJ*, 833:147. 3

[56] Lentz, E. J., Mezzacappa, A., Messer, O. E. B., Hix, W. R., and Bruenn, S. W. (2012a). Interplay of Neutrino Opacities in Core-collapse Supernova Simulations. *ApJ*, 760:94. 11

[57] Lentz, E. J., Mezzacappa, A., Messer, O. E. B., Liebendörfer, M., Hix, W. R., and Bruenn, S. W. (2012b). On the Requirements for Realistic Modeling of Neutrino Transport in Simulations of Core-Collapse Supernovae. *ApJ*, 747:73. 11

[58] Limongi, M. and Chieffi, A. (2003). Evolution, Explosion, and Nucleosynthesis of Core-Collapse Supernovae. *ApJ*, 592:404–433. 6

[59] McCray, R. (1993). Supernova 1987A revisited. *ARA&A*, 31:175–216. 3, 10

[60] Melson, T., Janka, H.-T., and Marek, A. (2015). Neutrino-driven Supernova of a Low-mass Iron-core Progenitor Boosted by Three-dimensional Turbulent Convection. *ApJ*, 801:L24. 33, 60, 63

[61] Meyer, B. S., Krishnan, T. D., and Clayton, D. D. (1998). Theory of Quasi-Equilibrium Nucleosynthesis and Applications to Matter Expanding from High Temperature and Density. *ApJ*, 498:808. 5

[62] Miller, D. S., Wilson, J. R., and Mayle, R. W. (1993). Convection Above the Neutrinosphere in Type II Supernovae. *ApJ*, 415:278–285. 4

[63] Müller, B., Gay, D. W., Heger, A., Tauris, T. M., and Sim, S. A. (2018). Multidimensional simulations of ultrastripped supernovae to shock breakout. *MNRAS*, 479(3):3675–3689. 13, 20

[64] Müller, B., Tauris, T. M., Heger, A., Banerjee, P., Qian, Y.-Z., Powell, J., Chan, C., Gay, D. W., and Langer, N. (2019). Three-dimensional simulations of neutrino-driven core-collapse supernovae from low-mass single and binary star progenitors. *Monthly Notices of the Royal Astronomical Society*, 484(3):3307–3324. 33

[65] Müller, E. (1998). Simulation of Astrophysical Fluid Flow. In *Saas-Fee Advanced Course 27: Computational Methods for Astrophysical Fluid Flow.*, page 343. 3

[66] Müller, E., Fryxell, B., and Arnett, D. (1991). Instability and clumping in SN 1987A. *A&A*, 251:505–514. 4, 7

[67] Müller, E., Hillebrandt, W., Orio, M., Hoflich, P., Monchmeyer, R., and Fryxell, B. A. (1989). Mixing and fragmentation in supernova envelopes. *A&A*, 220:167–176. 12

[68] Nagasawa, M., Nakamura, T., and Miyama, S. M. (1988). Three-dimensional hydrodynamical simulations of type II supernova : mixing and fragmentation of ejecta. *PASJ*, 40:691–708. 12

[69] Nagataki, S., Shimizu, T. M., and Sato, K. (1998). Matter Mixing from Axisymmetric Supernova Explosion. *ApJ*, 495:413. 7, 10

[70] O'Connor, E. and Ott, C. D. (2011). Black Hole Formation in Failing Core-Collapse Supernovae. *ApJ*, 730:70. 34

[71] Ono, M., Nagataki, S., Ferrand, G., Takahashi, K., Umeda, H., Yoshida, T., Orlando, S., and Miceli, M. (2020). Matter mixing in aspherical core-collapse supernovae: Three-dimensional simulations with single-star and binary merger progenitor models for SN 1987a. *The Astrophysical Journal*, 888(2):111. 16, 92

[72] Ott, C. D. (2009). Topical review: The gravitational-wave signature of core-collapse supernovae. *Classical Quantum Gravity*, 26:063001. 3

[73] Paxton, B., Schwab, J., Bauer, E. B., Bildsten, L., Blinnikov, S., Duffell, P., Farmer, R., Goldberg, J. A., Marchant, P., Sorokina, E., Thoul, A., Townsend, R. H. D., and Timmes, F. X. (2018). Modules for experiments in stellar astrophysics (mesa): Convective boundaries, element diffusion, and massive star explosions. *The Astrophysical Journal Supplement Series*, 234(2):34. 13

[74] Plewa, T. and Müller, E. (1999). The consistent multi-fluid advection method. *A&A*, 342:179–191. 16

[75] Rayleigh (1882). Investigation of the character of the equilibrium of an incompressible heavy fluid of variable density. *Proceedings of the London Mathematical Society*, s1-14(1):170–177. 7

[76] Rojas, D., Boukharfane, R., Dalcin, L., Del Rey Fernández, D. C., Ranocha, H., Keyes, D. E., and Parsani, M. (2021). On the robustness and performance of entropy stable collocated discontinuous galerkin methods. *Journal of Computational Physics*, 426:109891. 30, 31

[77] Sandoval, M. A., Hix, W. R., Messer, O. E. B., Lentz, E. J., and Harris, J. A. (2021). Three dimensional core-collapse supernova simulations with 160 isotopic species evolved to shock breakout. 1

[78] Schatz, H., Austin, S., Beers, T., Brown, A., Brown, E., Cyburt, R., Lynch, W., and Zegers, R., editors (2008). *Proceedings of Nuclei in the Cosmos X*. SISSA Proceedings of Science. 98, 99

[79] Scheck, L., Janka, H.-T., Foglizzo, T., and Kifonidis, K. (2008). Multidimensional supernova simulations with approximative neutrino transport. II. Convection and the advective-acoustic cycle in the supernova core. *A&A*, 477:931–952. 18

[80] Scheck, L., Kifonidis, K., Janka, H.-T., and Müller, E. (2006). Multidimensional supernova simulations with approximative neutrino transport. I. Neutron star kicks and the anisotropy of neutrino-driven explosions in two spatial dimensions. *A&A*, 457:963–986. 18

[81] Sedov, L. I. (1959). *Similarity and Dimensional Methods in Mechanics*. Academic Press. 8, 12

[82] Sinnott, B., Welch, D. L., Rest, A., Sutherland, P. G., and Bergmann, M. (2013). Asymmetry in the Outburst of SN 1987A Detected Using Light Echo Spectroscopy. *ApJ*, 767:45. 4

[83] Spyromilio, J., Meikle, W. P. S., and Allen, D. A. (1990). Spectral line profiles of iron and nickel in supernova 1987A - Evidence for a fragmented nickel bubble. *MNRAS*, 242:669–673. 4

[84] Stockinger, G., Janka, H.-T., Kresse, D., Melson, T., Ertl, T., Gabler, M., Gessner, A., Wongwathanarat, A., Tolstov, A., Leung, S.-C., Nomoto, K., and Heger, A. (2020). Three-dimensional models of core-collapse supernovae from low-mass progenitors with implications for Crab. *Monthly Notices of the Royal Astronomical Society*, 496(2):2039–2084. 13, 14, 18, 20, 33, 34, 38, 40, 54, 60, 62, 64, 91, 93, 94

[85] Strom, R., Johnston, H. M., Verbunt, F., and Aschenbach, B. (1995). A radio-emitting X-ray "bullet" ejected by the Vela supernova. *Nature*, 373(6515):590–592. 4

[86] Sukhbold, T., Ertl, T., Woosley, S. E., Brown, J. M., and Janka, H.-T. (2016). Core-collapse Supernovae from 9 to 120 Solar Masses Based on Neutrino-powered Explosions. *ApJ*, 821:38. 34

[87] Swesty, F. D. (1998). Gray models of convection in core-collapse supernovae. In Mezzacappa, A., editor, *Stellar Evolution,Stellar Explosions, and Galactic Chemical Evolution*, page 539. Bristol: IOP. 9

[88] Taylor, G. (1950). The Instability of Liquid Surfaces when Accelerated in a Direction Perpendicular to their Planes. I. *Proceedings of the Royal Society of London Series A*, 201(1065):192–196. 7

[89] Thielemann, F.-K., Nomoto, K., and Hashimoto, M. (1996). Core-Collapse Supernovae and Their Ejecta. *ApJ*, 460:408–436. 6, 10

[90] Timmes, F. X. and Swesty, F. D. (2000). The Accuracy, Consistency, and Speed of an Electron-Positron Equation of State Based on Table Interpolation of the Helmholtz Free Energy. *ApJS*, 126:501–516. 27

[91] Truelove, J. K. and McKee, C. F. (1999). Evolution of Nonradiative Supernova Remnants. *ApJs*, 120(2):299–326. 45

[92] Utrobin, V. P., Chugai, N. N., and Andronova, A. A. (1995). Asymmetry of SN 1987A: Fast Ni-56 clump. *A&A*, 295:129–135. 4

[93] Utrobin, V. P., Wongwathanarat, A., Janka, H.-T., and Müller, E. (2015). Supernova 1987A: neutrino-driven explosions in three dimensions and light curves. *A&A*, 581:A40. 13

[94] Utrobin, V. P., Wongwathanarat, A., Janka, H. T., Müller, E., Ertl, T., Menon, A., and Heger, A. (2021). Supernova 1987a: 3d mixing and light curves for explosion models based on binary-merger progenitors. *ApJ*. 13, 94

[95] Utrobin, V. P., Wongwathanarat, A., Janka, H. T., Müller, E., Ertl, T., and Woosley, S. E. (2019). Three-dimensional mixing and light curves: constraints on the progenitor of supernova 1987A. *A&A*, 624:A116. 13

[96] Wang, L., Wheeler, J. C., Höflich, P., Khokhlov, A., Baade, D., Branch, D., Challis, P., Filippenko, A. V., Fransson, C., Garnavich, P., Kirshner, R. P., Lundqvist, P., McCray, R., Panagia, N., Pun, C. S. J., Phillips, M. M., Sonneborn, G., and Suntzeff, N. B. (2002). The Axisymmetric Ejecta of Supernova 1987A. *ApJ*, 579:671–677. 3

[97] Weaver, T. A., Zimmerman, G. B., and Woosley, S. E. (1978). Presupernova evolution of massive stars. *ApJ*, 225:1021–1029. 33

[98] Wilson, J. R. (1985). Supernovae and Post–Collapse Behavior. In Centrella, J. M., LeBlanc, J. M., and Bowers, R. L., editors, *Numerical Astrophysics*, pages 422–434, Boston. Jones and Bartlett. 5

[99] Wilson, J. R. and Kothe, D. (1995). A marker particle method for interface tracking. In *Proceedings of the Sixth International Symposium on Computational Fluid Dynamics*. 30

[100] Wilson, J. R. and Mayle, R. W. (1993). Report on the Progress of Supernova Research by the Livermore Group. *Phys. Rep.*, 227:97–111. 10

[101] Wongwathanarat, A., Hammer, N. J., and Müller, E. (2010). An axis-free overset grid in spherical polar coordinates for simulating 3D self-gravitating flows. *A&A*, 514:A48. 22

[102] Wongwathanarat, A., Müller, E., and Janka, H.-T. (2015). Three-dimensional simulations of core-collapse supernovae: from shock revival to shock breakout. *A&A*, 577:A48. 8, 13, 14, 18, 20, 54, 63, 64, 90, 93

[103] Wooden, D. H. (1997). Observational evidence for mixing and dust condensation in core-collapse supernovae. In Bernatowicz, T. J. and Zinner, E., editors, *American Institute of Physics Conference Series*, volume 402 of *American Institute of Physics Conference Series*, pages 317–376. 3

[104] Woosley, S. E., Arnett, W. D., and Clayton, D. D. (1973). The explosive burning of oxygen and silicon. *ApJS*, 26:231–312. 5, 6

[105] Woosley, S. E., Heger, A., and Weaver, T. A. (2002). The evolution and explosion of massive stars. *Rev. Mod. Phys.*, 74:1015–1071. 3

[106] Woosley, S. E. and Weaver, T. A. (1995). The Evolution and Explosion of Massive Stars. II. Explosive Hydrodynamics and Nucleosynthesis. *ApJS*, 101:181–235. 2, 6, 10

[107] Woosley, S. E., Wilson, J. R., Mathews, G. J., Hoffman, R. D., and Meyer, B. S. (1994). The r-process and neutrino-heated supernova ejecta. *ApJ*, 433:229–246. 6

[108] Yamada, Y., Nakamura, T., and Oohara, K. (1990). Three Dimensional Simulations of Supernova Explosion. I. *Progress of Theoretical Physics*, 84(3):436–443. 12

[109] Yee, H. C., Sandham, N. D., and Djomehri, M. J. (1999). Low-Dissipative High-Order Shock-Capturing Methods Using Characteristic-Based Filters. *Journal of Computational Physics*, 150(1):199–238. 30

Appendices

A D9.6 Raw Data

Below is the full version of Table 3.1.

Table A: D9.6 Yields – Full Network

Species	D9.6–2D3D [$M_\odot$]	D9.6–3D3D [$M_\odot$]	D9.6–2D3D$_{\text{Tilted}}$ [$M_\odot$]
n	1.4199564137078323e-06	2.6529427168878523e-09	2.1795814616136960e-06
^{1}H	4.9952554808781757e+00	4.9579969642434030e+00	5.0166696391174339e+00
^{2}H	8.0845296507840918e-10	7.9515855657011458e-10	8.1376154415470935e-10
^{3}He	5.6670670620392698e-05	5.6249680140470084e-05	5.6914762474734532e-05
^{4}He	3.0520166296241991e+00	3.0225659335999944e+00	3.0561119920430557e+00
^{6}Li	1.0229682595062019e-15	1.4205516784910526e-16	1.0850251856499246e-15
^{7}Li	4.1560413709908041e-09	4.0629016621827812e-09	4.0639572614791332e-09
^{7}Be	3.5071140974193505e-10	4.5320538105573532e-11	3.6020786475088524e-10
^{9}Be	9.2969893972889262e-14	1.0899065502661643e-15	1.4593546886511454e-13
^{8}B	1.3041928678625940e-16	8.0616821508458612e-17	1.3309078681298502e-16
^{10}B	2.3893414356643739e-15	1.3003127172569191e-16	2.5261194692492267e-15
^{11}B	1.9579065471233406e-13	2.6043574934037548e-13	2.0023774157887455e-13
^{12}C	2.2898826418393310e-02	2.2271402691156659e-02	2.2260182572900845e-02
^{13}C	4.4764989980260834e-04	4.3465069126238102e-04	4.3483696309192898e-04
^{14}C	3.1400691024714335e-05	2.5928231222874485e-06	3.3091598286818158e-05
^{13}N	3.1733106090178613e-09	2.3195306916657640e-09	3.1967677274750869e-09
^{14}N	2.8794241950257944e-05	2.7948008820676957e-05	2.7972924050657676e-05
^{15}N	1.7716302366811702e-07	5.6777858801621120e-09	1.8785646638691103e-07
^{14}O	4.5946003224250459e-10	1.1864096641763832e-09	4.7258181758748481e-10
^{15}O	8.9740806082636361e-10	5.1076606266359024e-10	9.0746525056034952e-10
^{16}O	8.1251554589733908e-03	8.0504277949834287e-03	7.9740312048282858e-03
^{17}O	1.0141928334446198e-06	9.1325912239315569e-07	9.8295799222550116e-07
^{18}O	4.1616657984213330e-06	5.6340591521527807e-08	4.4808641844402533e-06
^{17}F	8.3235277166700328e-12	5.5631119894320775e-11	8.5437549572041178e-12
^{18}F	3.8183867985922700e-10	1.5113736935245758e-10	3.8528766820971277e-10

Table A continued

Species	D9.6–2D3D [$M_\odot$]	D9.6–3D3D [$M_\odot$]	D9.6–2D3D$_{\rm Tilted}$ [$M_\odot$]
^{19}F	3.8552391327491633e-08	2.2904851149013118e-08	3.8667742940865500e-08
^{18}Ne	2.1267016309925136e-10	1.2950679225389314e-09	2.1773833594503482e-10
^{19}Ne	5.2968804596213245e-11	1.0541720116126527e-11	5.5056965034443653e-11
^{20}Ne	5.5505605134209719e-04	5.9767510838838549e-04	5.5218806650251054e-04
^{21}Ne	2.3370371739109787e-06	1.2960946627245711e-06	2.2933209931927965e-06
^{22}Ne	1.7299930757395664e-05	5.2872236515897665e-06	1.8109886662044146e-05
^{21}Na	5.7794489792594922e-08	3.7382908380634288e-08	5.9182320989113330e-08
^{22}Na	2.4554257892232507e-08	2.2572013348854956e-08	2.3071841208025411e-08
^{23}Na	1.1502959052574456e-06	1.0406769335983186e-06	1.1581951424516625e-06
^{23}Mg	2.3387351479898075e-07	2.1693743317983946e-07	2.3445421695461773e-07
^{24}Mg	1.7839287237585039e-04	1.9589866562193359e-04	1.7851402609837623e-04
^{25}Mg	1.9509645700296458e-06	1.5964300555322098e-06	1.9355657160261469e-06
^{26}Mg	2.1798380029632719e-05	4.6468939698565832e-06	2.2490792591858823e-05
^{25}Al	2.5966276983423616e-07	1.5574084718609083e-07	2.6696286166881643e-07
^{26}Al	6.2702760648952021e-07	6.6777151293194470e-07	6.2860369463029793e-07
^{27}Al	8.5144663753951816e-06	9.4811799854020176e-06	8.5553778680054270e-06
^{28}Si	5.1180164369679800e-04	6.1805642274818083e-04	5.1568489476168291e-04
^{29}Si	5.3063415217271190e-06	4.7588369006910888e-06	5.3447739620592045e-06
^{30}Si	1.8905648716447008e-05	1.1376157610450952e-05	1.9059201940178350e-05
^{31}Si	3.1694755893770563e-07	2.7309733972958049e-08	3.1856320991650358e-07
^{32}Si	4.7616516835130329e-05	1.5691159572913614e-06	4.8421606527780971e-05
^{29}P	7.9247221986503838e-07	4.9208278966612286e-07	8.1493965416508003e-07
^{30}P	4.6799213881258441e-07	3.7475489287227750e-07	4.7056713550645132e-07
^{31}P	5.3154100406450333e-06	6.9819330842432596e-06	5.3477813924681950e-06
^{32}P	5.7322911176275710e-07	1.3003988377503715e-07	5.7753715712240397e-07
^{33}P	2.2565684008058479e-06	1.9603545220218988e-07	2.2910634392726121e-06
^{32}S	3.8230142970971105e-04	4.4998758832106314e-04	3.8564435391016971e-04
^{33}S	2.7638774400285118e-06	3.1287251109390957e-06	2.7844421508459976e-06

Table A continued

Species	D9.6–2D3D [$M_\odot$]	D9.6–3D3D [$M_\odot$]	D9.6–2D3D$_{\rm Tilted}$ [$M_\odot$]
^{34}S	2.5058620950419755e-05	1.7713393639604871e-05	2.5336010076388057e-05
^{35}S	1.3245716930392169e-06	1.4843875386363429e-07	1.3345122493516802e-06
^{36}S	5.2029387460943198e-05	2.8415305052063650e-06	5.2614549153908892e-05
^{33}Cl	2.0517882239172314e-06	1.2499020636679245e-06	2.1098421202346879e-06
^{34}Cl	2.1133468638299416e-07	1.4454449042010286e-07	2.1663451550673452e-07
^{35}Cl	9.3186350788421265e-06	1.2158564014814615e-05	9.3635990841107005e-06
^{36}Cl	1.2111435857335783e-07	7.5221027738096689e-08	1.2168844891333171e-07
^{37}Cl	1.8699441065798946e-06	4.5101149320905613e-07	1.8930161162216138e-06
^{36}Ar	1.2592294700823056e-04	1.3692312869761946e-04	1.2703314067322079e-04
^{37}Ar	5.3094116763132840e-07	5.7916353717203618e-07	5.3355607510042176e-07
^{38}Ar	1.9873445800056729e-05	2.0149896721285957e-05	2.0023106519928340e-05
^{39}Ar	3.9801157312986957e-07	8.6215099956867984e-08	4.0019172763593752e-07
^{40}Ar	7.6788767121301226e-06	9.4246351961927425e-07	7.7648156509510744e-06
^{37}K	1.5499158067182951e-06	9.1064434865277436e-07	1.5926453437415382e-06
^{38}K	1.7048615514111986e-07	1.4962096576570645e-07	1.7445144302044086e-07
^{39}K	8.6516918911919013e-06	1.1646435699397088e-05	8.6893611658031031e-06
^{40}K	4.4973162072064922e-08	3.3294301103043517e-08	4.5213619410319996e-08
^{41}K	3.7317651230919255e-07	1.2821700746101390e-07	3.7595428118187268e-07
^{40}Ca	1.9553066786677498e-04	2.0089437364164683e-04	1.9748582470861055e-04
^{41}Ca	4.6666494167306593e-07	5.3990982548933514e-07	4.6841423248297596e-07
^{42}Ca	1.1065052862482392e-05	1.5726313492373155e-05	1.1101895845719344e-05
^{43}Ca	8.6593282564809710e-07	7.0784889789024915e-07	8.6859679331982518e-07
^{44}Ca	8.1443850147683719e-07	3.8931914345371919e-07	8.1716953860922773e-07
^{45}Ca	1.2435894533406995e-07	3.4317831887976322e-08	1.2453338154760455e-07
^{46}Ca	8.2872733277755903e-07	2.1342622843589933e-07	8.3271327400962575e-07
^{47}Ca	1.0979389675968129e-07	2.3863292296884585e-08	1.1008255651925830e-07
^{48}Ca	1.5634010931995276e-04	1.4187801738331592e-05	1.6046249826393561e-04
^{43}Sc	2.7482013149851435e-06	3.8430351257264304e-06	2.7540743018670224e-06

Table A continued

Species	D9.6–2D3D [$M_\odot$]	D9.6–3D3D [$M_\odot$]	D9.6–2D3D$_{\rm Tilted}$ [$M_\odot$]
^{44}Sc	1.3690058766913975e-07	1.7756405199777690e-07	1.3726772155486826e-07
^{45}Sc	8.1918127012350837e-07	9.9812764818595734e-07	8.2221957562750277e-07
^{46}Sc	6.0891104080907322e-08	5.1109150438618310e-08	6.1152040501348932e-08
^{47}Sc	3.2956198465889639e-07	2.2372400029801528e-07	3.3069143014143645e-07
^{48}Sc	3.1175515077216763e-06	1.6342573563435971e-06	3.1443706266893703e-06
^{49}Sc	2.1426506407204779e-05	2.7313056104557510e-06	2.1853869596748507e-05
^{44}Ti	7.5572696763202608e-06	7.4460584689863159e-06	7.7051226924772174e-06
^{45}Ti	2.5900752780301759e-07	4.2052227902989610e-07	2.5921642154108391e-07
^{46}Ti	4.6934771127579243e-06	6.7402738315520488e-06	4.7058842118584422e-06
^{47}Ti	6.5485526777213375e-07	7.4761647336254893e-07	6.5663325890680323e-07
^{48}Ti	1.8990169785900674e-06	1.4887943448092577e-06	1.9078070760072434e-06
^{49}Ti	8.7827633114070438e-07	6.2559490564250343e-07	8.8234194380277347e-07
^{50}Ti	1.2075127236603232e-05	7.0729229991642793e-06	1.2208442978972005e-05
^{51}Ti	5.1777051298358842e-06	5.8642206183844890e-07	5.3448676252655838e-06
^{46}V	3.4403459089933225e-08	3.0236962492076898e-08	3.5273612803630063e-08
^{47}V	1.4434039887285056e-06	2.2518379325380931e-06	1.4472801973617137e-06
^{48}V	4.8230996245454335e-07	5.7472254035627275e-07	4.8377521945121268e-07
^{49}V	1.9396176935304842e-06	2.1453430755858115e-06	1.9450757416397794e-06
^{50}V	1.7709476880170053e-07	1.5521681767987219e-07	1.7791577100155021e-07
^{51}V	2.8400051926113788e-06	1.6584639757254962e-06	2.8653290974658490e-06
^{52}V	1.0157551708921960e-06	2.2210756785558873e-07	1.0297025224467886e-06
^{48}Cr	1.2901854879684655e-05	1.1523950492040053e-05	1.3180721738353080e-05
^{49}Cr	6.7511529024583690e-07	8.6351430716966206e-07	6.7797337975716540e-07
^{50}Cr	4.0360258369304734e-06	6.0768825847415601e-06	4.0616804669377388e-06
^{51}Cr	1.2489663969629368e-06	1.2267553132127629e-06	1.2563265151084741e-06
^{52}Cr	2.9520782924480376e-05	1.9950162911297432e-05	2.9930593876252384e-05
^{53}Cr	3.0627781199317503e-06	1.4218686406230038e-06	3.1110246254645813e-06
^{54}Cr	6.2186965812697522e-05	2.2600237942693866e-05	6.3087916539963243e-05

Table A continued

Species	D9.6–2D3D [$M_\odot$]	D9.6–3D3D [$M_\odot$]	D9.6–2D3D$_{\rm Tilted}$ [$M_\odot$]
^{50}Mn	1.8517464649460687e-07	8.1241902724433725e-08	1.9311555977238603e-07
^{51}Mn	8.5469377155589301e-07	1.2448866597491616e-06	8.5955336909742555e-07
^{52}Mn	5.9342427314487553e-07	7.5944482718483399e-07	5.9569761350697769e-07
^{53}Mn	5.5566805529303093e-06	5.4173829577645327e-06	5.6015259009534940e-06
^{54}Mn	1.6458859963784061e-06	1.4561465994059902e-06	1.6584856122055649e-06
^{55}Mn	8.6472854392532108e-06	6.6659227594374612e-06	8.7665356449170343e-06
^{52}Fe	2.7774505645023626e-05	2.9553404534695611e-05	2.8197023516492852e-05
^{53}Fe	3.9740439763335140e-06	4.1976146848931587e-06	4.0137149645137093e-06
^{54}Fe	3.1367576059686204e-04	2.9317904504893731e-04	3.1589021955048553e-04
^{55}Fe	2.3065448717094453e-05	2.4686841850630301e-05	2.3307378874645215e-05
^{56}Fe	2.7495217933729173e-04	2.3629905437715101e-04	2.7860721561204238e-04
^{57}Fe	7.2955288519507492e-06	5.8093742079462603e-06	7.3873417409620462e-06
^{58}Fe	1.8056521707372370e-04	1.4184877677771694e-04	1.8497203448331306e-04
^{53}Co	5.2768628764365293e-06	2.2738013758231447e-06	5.4339008846274176e-06
^{54}Co	1.9452977942193994e-06	1.1686799256560358e-06	2.0096602133156917e-06
^{55}Co	2.0271839383161986e-05	1.5245126233806054e-05	2.0358353388702548e-05
^{56}Co	5.2969403264533685e-06	4.3026452350356406e-06	5.3342781947767879e-06
^{57}Co	2.4934033666737836e-05	2.3468155538720361e-05	2.5173064191683494e-05
^{58}Co	1.8623112936919005e-06	1.9216790301088375e-06	1.8773961074962361e-06
^{59}Co	1.8694698204963268e-05	2.2631391886002514e-05	1.8938991847133315e-05
^{56}Ni	2.7117116521096847e-03	2.3371180680595285e-03	2.7673933800370027e-03
^{57}Ni	7.8681412779977436e-05	8.8849085757695490e-05	7.9820877434045985e-05
^{58}Ni	2.1498931479751299e-03	1.9930721852975185e-03	2.1668649234884937e-03
^{59}Ni	1.0841680358148332e-04	9.3786496025350418e-05	1.0911432238661160e-04
^{60}Ni	4.0133669956858107e-03	3.6687180886753805e-03	4.0438653328124814e-03
^{61}Ni	7.5824074885938472e-05	6.6742913859054896e-05	7.6627500998650833e-05
^{62}Ni	2.4181842189357075e-03	2.8232799898811520e-03	2.4483885834315124e-03
^{63}Ni	1.4158513333443253e-05	1.5097601958916688e-05	1.4431541702849294e-05

Table A continued

Species	D9.6–2D3D [$M_\odot$]	D9.6–3D3D [$M_\odot$]	D9.6–2D3D$_{\rm Tilted}$ [$M_\odot$]
^{64}Ni	1.7141684444907483e-03	1.0093377623661534e-03	1.7831359695519638e-03
^{57}Cu	2.6060111185362493e-07	6.1055572789683355e-07	2.6617108188927799e-07
^{58}Cu	2.1229481569797679e-06	2.2170938608263650e-06	2.1646135463877118e-06
^{59}Cu	3.2184075919716940e-05	3.8013473434569072e-05	3.2789540651163833e-05
^{60}Cu	1.3827540662221102e-06	1.3833249514384308e-06	1.4011527825436781e-06
^{61}Cu	4.7248568973986922e-05	4.5719594090087801e-05	4.7467227527608887e-05
^{62}Cu	4.6826030001937763e-06	4.1556354193143393e-06	4.7154780078667065e-06
^{63}Cu	1.6189276675274879e-04	1.7800733534747236e-04	1.6310567046331904e-04
^{64}Cu	6.9629868812602570e-06	9.8574416009425681e-06	7.0082506536679261e-06
^{65}Cu	1.0569684280946245e-04	9.7590020661408883e-05	1.0724169115329112e-04
^{59}Zn	3.8397329722495243e-05	1.4011368661229242e-05	3.9838144863085598e-05
^{60}Zn	1.3356346046825484e-04	1.4600908508040705e-04	1.3676669368957112e-04
^{61}Zn	2.4318113035169105e-06	4.0682510860086028e-06	2.4861187879602705e-06
^{62}Zn	1.7362004794428904e-04	2.0125838380086108e-04	1.7537475817904716e-04
^{63}Zn	1.1781033943487055e-05	1.1283297466973859e-05	1.1861798022392614e-05
^{64}Zn	1.1282732713222914e-03	9.9768817535982935e-04	1.1366374566700310e-03
^{65}Zn	2.9218391697275279e-05	2.5728832756819904e-05	2.9477126289507629e-05
^{66}Zn	1.3828781883220055e-03	1.1415202011527499e-03	1.3987521054048381e-03
^{62}Ga	3.7141653447606137e-07	1.9375726001943379e-07	3.8830160602419624e-07
^{63}Ga	8.4395815795933117e-06	1.0669890356419179e-05	8.6154173951943401e-06
^{64}Ga	4.3806586651714876e-07	5.9609372169336739e-07	4.4900084955018392e-07
^{63}Ge	3.2607584150981463e-06	8.7712080661022754e-07	3.4163199582090596e-06
^{64}Ge	1.0400616489804946e-05	2.8404331890205535e-05	1.0672556884181378e-05

B D10 Raw Data

Below is the full version of Table 3.2.

Table B: D10 Yields – Full Network

Species	D10–2D3D [$M_\odot$]	D10–2D3D$_{\text{Tilted}}$ [$M_\odot$]
n	2.9270063273711386e-12	2.8362527353632702e-12
^{1}H	4.1310168309503119e+00	4.2772123540347442e+00
^{2}H	2.3261595116345055e-05	2.4084700745699424e-05
^{3}He	2.1391940623925125e-04	2.2148839302139507e-04
^{4}He	2.4877048480453792e+00	2.5325856028368547e+00
^{6}Li	6.2263927584259865e-10	6.4466951622620770e-10
^{7}Li	8.8493003946954199e-09	9.1624099723404100e-09
^{7}Be	2.2738131759741558e-10	3.0805522420300972e-10
^{9}Be	1.6350870884121395e-10	1.6929412308993537e-10
^{8}B	9.4388455290453703e-17	1.1151679434467820e-16
^{10}B	8.6267053898423152e-10	8.9319361902392697e-10
^{11}B	3.7786259780897394e-09	3.9123063448932696e-09
^{12}C	4.5459348780484299e-02	4.5797996522708204e-02
^{13}C	5.4726770883505515e-04	5.6470026492525948e-04
^{14}C	6.5681044920748475e-07	6.3572937913926721e-07
^{13}N	3.3467792931542939e-07	1.0339230935523961e-06
^{14}N	1.9286569844457233e-02	1.9614070387703464e-02
^{15}N	8.1558758036311206e-06	8.4217220839995081e-06
^{14}O	1.2620974667528705e-06	4.5159679671585739e-06
^{15}O	8.2847296380703864e-09	2.8806363878429467e-08
^{16}O	7.9849035460711884e-02	8.0755181901590409e-02
^{17}O	5.8243609838307482e-05	6.0103774009459882e-05
^{18}O	1.3223070405743351e-03	1.3451067914695828e-03
^{17}F	2.6741621617063879e-09	1.6110120770870592e-08
^{18}F	1.6590765906104304e-08	1.7577966336968208e-08

Table B continued

Species	D10–2D3D [$M_\odot$]	D10–2D3D$_{\rm Tilted}$ [$M_\odot$]
^{19}F	2.8235460302625981e-06	2.9154922967595559e-06
^{18}Ne	3.3894101673673197e-08	1.1545673721063797e-07
^{19}Ne	1.0875145758878511e-09	3.6789562845708593e-09
^{20}Ne	9.2644013884879643e-03	9.4689495235076478e-03
^{21}Ne	3.7411549587824697e-05	3.8179804470359877e-05
^{22}Ne	3.3749986942084361e-03	3.4291775402952840e-03
^{21}Na	1.3041300288850454e-05	2.6795458922924412e-05
^{22}Na	2.5533405059028811e-08	9.0103985250642180e-08
^{23}Na	4.7822414451481794e-04	4.8602848598610477e-04
^{23}Mg	2.3854849569189449e-07	5.1820365912702795e-07
^{24}Mg	4.1815956608988823e-03	4.2771049518522900e-03
^{25}Mg	6.6516163187911495e-04	6.7523386645274724e-04
^{26}Mg	8.7031703145582146e-04	8.8148941208763512e-04
^{25}Al	2.2285365517291240e-05	3.2050450313164700e-05
^{26}Al	9.3354741989035830e-06	1.1350581855876075e-05
^{27}Al	5.1812592820200216e-04	5.2835793413950557e-04
^{28}Si	7.8423805354943324e-03	7.9476317483286301e-03
^{29}Si	3.7151382113220685e-04	3.7569278894585592e-04
^{30}Si	2.9745886106394352e-04	2.9800763198293233e-04
^{31}Si	1.3529929352471389e-07	1.3401869624905091e-07
^{32}Si	1.5779941380185839e-08	1.6059211148701408e-08
^{29}P	1.9381531665836941e-04	2.2916462678188536e-04
^{30}P	1.5778608829258812e-05	1.9372480672654725e-05
^{31}P	8.4069608811126591e-05	8.4449451623657421e-05
^{32}P	3.1593418182239792e-07	3.0657272036374315e-07
^{33}P	9.8441605948080006e-08	9.7232434495693269e-08
^{32}S	4.9036535841889394e-03	4.9476254791923999e-03
^{33}S	4.1424226034509952e-05	4.4081258555536302e-05

Table B continued

Species	D10–2D3D [$M_\odot$]	D10–2D3D$_{\rm Tilted}$ [$M_\odot$]
^{34}S	1.8551986768347245e-04	1.9018733154987526e-04
^{35}S	3.4291006884246201e-07	3.3314134021763090e-07
^{36}S	1.0747437970875997e-06	1.0769015276581990e-06
^{33}Cl	2.2609033286771378e-04	2.6638691527606313e-04
^{34}Cl	2.0157904766259641e-05	2.4709620721801101e-05
^{35}Cl	4.1115977279094159e-05	4.1662952228107314e-05
^{36}Cl	2.1568334906867252e-07	2.0946324241698202e-07
^{37}Cl	1.2723191654826053e-05	1.2954683703069943e-05
^{36}Ar	1.2809159278828310e-03	1.2928183842154967e-03
^{37}Ar	3.4433543282784941e-06	4.7509312091707302e-06
^{38}Ar	1.4596711731990265e-04	1.5071041400547945e-04
^{39}Ar	3.4732883618663427e-07	3.4155456408409044e-07
^{40}Ar	4.0567654330980889e-07	4.0786065396001225e-07
^{37}K	5.8794915963590586e-05	6.9125288058609599e-05
^{38}K	1.1015313101797421e-05	1.3061994483550926e-05
^{39}K	3.2515397001308133e-05	3.3519462119078649e-05
^{40}K	1.8199838201729305e-07	1.8206397873474468e-07
^{41}K	2.2803686737745875e-06	2.3395520185647929e-06
^{40}Ca	1.6972275232612895e-03	1.7380612586925899e-03
^{41}Ca	6.6864338965486435e-07	7.3477627444327527e-07
^{42}Ca	5.1336221174247370e-06	5.2841070918309354e-06
^{43}Ca	8.2508555526913271e-07	8.4416044236250456e-07
^{44}Ca	1.1658867063712865e-05	1.1980332842191931e-05
^{45}Ca	2.6667616050679683e-08	2.6256414277837249e-08
^{46}Ca	4.0479345238671427e-08	4.1076944571453630e-08
^{47}Ca	1.8871889277012129e-09	1.9574947348559665e-09
^{48}Ca	1.1321524929304705e-06	1.1638671721620551e-06
^{43}Sc	1.9383289377309260e-08	2.6021653218010324e-08

Table B continued

Species	D10–2D3D [$M_\odot$]	D10–2D3D$_{\rm Tilted}$ [$M_\odot$]
^{44}Sc	3.4215754588863119e-09	3.7152031633041578e-09
^{45}Sc	3.8661857166083060e-07	3.9536349790715185e-07
^{46}Sc	1.6922513681925525e-08	1.6733450560104483e-08
^{47}Sc	9.7194906454638897e-09	9.6659465662922211e-09
^{48}Sc	5.1369270898401573e-09	5.1250721729302467e-09
^{49}Sc	1.7258898873852364e-09	1.7481136485255495e-09
^{44}Ti	8.9524690464558147e-05	9.4814593095347212e-05
^{45}Ti	1.7655471868570966e-08	2.1352612236579444e-08
^{46}Ti	2.5422043655315255e-06	2.6197654578104655e-06
^{47}Ti	1.7713079928627667e-06	1.8179387783529837e-06
^{48}Ti	1.7092837049181980e-05	1.7580236850534619e-05
^{49}Ti	1.4095673230796274e-06	1.4465773034010718e-06
^{50}Ti	1.4207060422508451e-06	1.4538384248642292e-06
^{51}Ti	1.1193953792199698e-08	1.1273983118267612e-08
^{46}V	2.8928480627182462e-08	3.5320385128811372e-08
^{47}V	2.6847192478565794e-08	3.1868710667618994e-08
^{48}V	1.1586593176388191e-08	1.8107910695668742e-08
^{49}V	9.6868680316115114e-08	9.9685589487685176e-08
^{50}V	2.6555655386655829e-08	2.6825092944822074e-08
^{51}V	2.9772392045610649e-06	3.0587829675411287e-06
^{52}V	1.9301183890066152e-08	1.9240194540748257e-08
^{48}Cr	1.2431589163756571e-04	1.3249884349440113e-04
^{49}Cr	5.0289516242550881e-07	5.1476762289610707e-07
^{50}Cr	8.2840911606899237e-06	8.4501320085965186e-06
^{51}Cr	1.2873819127480494e-07	1.3169840293719833e-07
^{52}Cr	1.1165115849650819e-04	1.1484205047178805e-04
^{53}Cr	1.2873032636085415e-05	1.3236454371170327e-05
^{54}Cr	3.8777390625882387e-06	3.9658353245150799e-06

Table B continued

Species	D10–2D3D [$M_\odot$]	D10–2D3D$_{\rm Tilted}$ [$M_\odot$]
^{50}Mn	2.7223340107440088e-07	3.0464368859406035e-07
^{51}Mn	8.0926582336221038e-07	8.0021913742452947e-07
^{52}Mn	7.6401781893915253e-08	1.0075639316894893e-07
^{53}Mn	3.8568166724054424e-07	4.1426585342280429e-07
^{54}Mn	3.0854499010925438e-08	3.2243168396931332e-08
^{55}Mn	1.0102403513026122e-04	1.0387072275414131e-04
^{52}Fe	2.1459079792093439e-04	2.2066822477125975e-04
^{53}Fe	2.4682185621298028e-05	2.6524723383371852e-05
^{54}Fe	7.5810565175654589e-04	7.6776245952206174e-04
^{55}Fe	1.7433409283522824e-06	1.8965540795503592e-06
^{56}Fe	8.5254963173130773e-03	8.7687730634290473e-03
^{57}Fe	2.1603331579797463e-04	2.2185563401007076e-04
^{58}Fe	5.8403060596124272e-05	5.8896509429100757e-05
^{53}Co	1.7070819392726075e-05	1.7707042611350336e-05
^{54}Co	1.8613339322992803e-05	1.9063915658268030e-05
^{55}Co	4.7151354159189547e-05	4.7865514003008494e-05
^{56}Co	9.0404013649215076e-07	1.2450098968497035e-06
^{57}Co	8.0636481485914072e-07	1.1304500612762702e-06
^{58}Co	9.5966078910671782e-08	1.2873592897765167e-07
^{59}Co	3.6626422962852173e-05	3.7321363270892829e-05
^{56}Ni	9.8595043264284345e-03	1.1152463513791719e-02
^{57}Ni	6.8101426565941861e-05	7.8659968663663841e-05
^{58}Ni	4.5031118753671939e-04	4.9660857877220643e-04
^{59}Ni	1.5268921621364340e-06	1.8561328860494188e-06
^{60}Ni	1.5712813183119982e-04	1.6161470983442870e-04
^{61}Ni	9.3457512306150677e-06	9.5390991862549341e-06
^{62}Ni	3.1018798209490773e-05	3.1472803551686080e-05
^{63}Ni	3.0716335094729509e-06	3.0149449366652000e-06

Table B continued

Species	D10–2D3D [$M_\odot$]	D10–2D3D$_{\rm Tilted}$ [$M_\odot$]
^{64}Ni	1.2149404219842757e-05	1.2195104083744122e-05
^{57}Cu	1.5520442191270517e-06	2.1681441416499851e-06
^{58}Cu	3.4007044107962974e-06	3.9338322932982823e-06
^{59}Cu	3.4181146128076785e-05	5.0775275581015833e-05
^{60}Cu	5.5624407479751314e-07	7.8550091645041652e-07
^{61}Cu	5.5378885735283919e-08	7.9196627563748484e-08
^{62}Cu	8.3373028565687937e-09	1.4970753424503495e-08
^{63}Cu	5.1656847685356130e-06	5.3028979536877155e-06
^{64}Cu	1.2632957590023492e-07	1.2541672229061914e-07
^{65}Cu	4.1036084646623207e-06	4.1185745685683870e-06
^{59}Zn	1.0028265162746272e-05	1.1418628969326769e-05
^{60}Zn	3.1508278307852266e-04	3.8895806923823620e-04
^{61}Zn	6.3710679526538028e-07	8.3800735116099370e-07
^{62}Zn	2.3144153123952835e-06	4.5357990970196921e-06
^{63}Zn	5.1844002557733706e-08	8.0591670800270831e-08
^{64}Zn	8.0258066939638277e-06	8.2959485188203087e-06
^{65}Zn	5.8187110107467370e-08	5.9347555252154327e-08
^{66}Zn	6.4815026864259690e-06	6.5724998918138215e-06
^{62}Ga	8.9483716434910706e-08	9.5120404707727544e-08
^{63}Ga	2.6631123034760408e-06	3.6986010079792853e-06
^{64}Ga	2.2331426544182326e-07	2.7233282680195702e-07
^{63}Ge	6.2708249052167436e-07	6.7168869269981536e-07
^{64}Ge	1.4253551585491766e-05	1.8582869727752781e-05

Vita

Michael Sandoval grew up in Fremont, California where he attended American High School. After high school, he received his Bachelor of Science degree from San José State University (SJSU) where he majored in Physics and minored in both Math and Astronomy. During his final year at SJSU, he conducted research in observational astronomy and discovered an astronomical object that is the densest known free-floating star system in the universe, which spawned a new object classification – a "hyper compact cluster". His team also discovered an object that is the record holder for the densest known galaxy in the universe. His passion for computational astrophysics led him to graduate school at the University of Tennessee, Knoxville (UTK) where he pursued a PhD in Physics with a concentration in Astrophysics. After graduating from UTK, he will begin his new staff position as an HPC Engineer in the Oak Ridge Leadership Computing Facility at Oak Ridge National Laboratory.